

Physics and Processing of Vanadium Dioxide for Optical Devices

By

Robert Marvel

Dissertation

Submitted to the Faculty of the
Graduate School of Vanderbilt University
in partial fulfillment of the requirements
for the degree of

DOCTOR OF PHILOSOPHY

in

Interdisciplinary Materials Science

May, 2016

Nashville, Tennessee

Approved:

Professor Richard Haglund

Professor Jason Valentine

Professor Bridget Rogers

Professor Norman Tolk

Professor Timothy Hanusa

TABLE OF CONTENTS

	Page
LIST OF TABLES	vii
LIST OF FIGURES	ix
Chapter	
1 Introduction to VO ₂ : The Basics	1
1.1 The Problem	1
1.2 Brief History of VO ₂ Research	2
1.3 Properties of Vanadium Dioxide	3
1.3.1 Structural Transition	5
1.3.2 Electronic Transition	6
1.3.3 Triggering the Phase Transition	6
1.3.4 Phase Stability	8
1.3.5 Hysteresis Width and Contrast	9
1.3.6 Defects	11
1.3.7 Temporal Response	11
1.3.8 A Monoclinic Metal	12
1.4 Materials Platforms for Optical Modulators	13
1.4.1 Limitations of Silicon-Based Electronic Modulators	13
1.4.2 Limitations of Other Materials	15
1.5 Outline of Dissertation	15
2 Optical Modulation with VO ₂	17
2.1 Introduction	17
2.2 Background: VO ₂ Based Devices	17
2.2.1 Optical	18

2.2.2	Electrical	20
2.2.3	Mechanical	21
2.3	Photothermal and CW Optical Modulation of Si-VO ₂ Ring Resonators	23
2.3.1	Introduction	23
2.3.2	Contributions	23
2.3.3	Fabrication	24
2.3.4	Experimental	24
2.3.5	Results and Discussion	26
2.4	Pulsed Optical Modulation of Si-VO ₂ Ring Resonators	32
2.4.1	Experimental	32
2.4.2	Results and Discussion	33
2.5	Conclusions: VO ₂ Optical Devices	38
3	Er Doped VO ₂	41
3.1	Introduction	41
3.2	Er-Doped VO ₂	41
3.2.1	Contributions	42
3.3	Erbium Doped Films: Crystal Symmetry	42
3.3.1	Erbium Doped Films: Experimental	42
3.3.2	Erbium Doped Films: Results and Discussion	44
3.3.3	Raman Scattering	44
3.3.4	Photoluminescence	44
3.3.5	Reflectivity Switching	47
3.3.6	Conclusions: Erbium Doped Thin Films	50
3.4	Erbium Doped Single Crystals	50
3.4.1	Erbium Single Crystals: Fabrication	50
3.4.2	Erbium Single Crystals: Results and Discussion	50
3.4.3	Conclusions: Er Doped Crystals	52

3.5	Conclusions: Erbium and VO ₂	52
4	Processing VO ₂ Thin Films and Crystals	54
4.1	Introduction	54
4.2	Thin Films: Motivation	54
4.2.1	Contributions	56
4.2.2	Introduction	56
4.3	Thin Films: Experimental	57
4.3.1	Substrates	57
4.3.2	Deposition Processes	57
4.3.3	Annealing	58
4.3.4	Rutherford backscattering spectrometry	59
4.3.5	X-ray photoelectron spectroscopy	59
4.3.6	X-ray reflectivity	60
4.3.7	Optical Characterization	60
4.3.8	Morphology	61
4.4	Thin Films: Results and Discussion	62
4.4.1	Composition	62
4.4.2	Optical Performance	63
4.4.3	Morphology	67
4.4.4	X-ray reflectivity	72
4.5	Thin Films: Conclusions	73
4.6	Single Crystals: Introduction	74
4.7	Single Crystals: Fabrication	75
4.8	Conclusions: Single Crystals	79
4.9	Conclusions: State of VO ₂ Fabrication	80
5	The Non-equilibrium Metallic Response of VO ₂	82
5.1	Introduction	82

5.2	Dynamics of Femtosecond Laser Pulse Excitation in Vanadium Dioxide . . .	82
5.2.1	Contributions	83
5.2.2	Introduction to Time Resolved Spectroscopy	83
5.3	Introduction: Time-Resolved Photoelectron Spectroscopy	92
5.3.1	Experiment	93
5.3.2	Results and Discussion	93
5.3.3	Conclusion: PES	98
5.4	Coherent Phonon Generation	98
5.4.1	Experiment	99
5.4.2	Results and Discussion	99
5.4.3	Conclusions: Coherent Phonon Generation	107
5.5	Conclusions: Ultrafast Behavior	107
6	Electronic Structure and Optical Properties of Tungsten Doped VO ₂	109
6.1	Introduction	109
6.2	Tungsten-Doped Vanadium Dioxide	109
6.2.1	Contributions	110
6.3	Optical Properties of Tungsten Doped VO ₂	111
6.3.1	Fabrication	111
6.3.2	Experimental Setup	111
6.3.3	Results and Discussion: 10-40 μm	112
6.3.4	Results and Discussion: 1.6-12 μm	116
6.3.5	Results and Discussion: 0.3-1.6 μm	119
6.4	Conclusions	123
7	Outlook for VO ₂ Based Optical Devices	126
	APPENDICES	129
A	Supplementary Information for Chapter 4	130

B Contributions to VO_2 Knowledge 149

BIBLIOGRAPHY 152

LIST OF TABLES

Table	Page
1.1 Tabulation of vanadium dioxide properties above and below the phase transition.	4
1.2 Optical Properties of VO ₂ thin film above and below the phase transition[11]. 5	5
2.1 Current optical modulator performance metrics as compiled by Reed[58]. . .	40
4.1 Tabulation of substrate physical properties. Information is provided from supplier data sheets unless otherwise noted.	58
4.2 Comparison of the three deposition processes. Energy given is for the ejected target material before contacting the substrate. The flux-to-diffusion ratio is a measure of how adatom mobility (Energy) is affected by atoms impacting the film surface (Rate) and is discussed more below.	59
4.3 Sample labeling scheme used in this work. Example: P_Sa_30 = is a film deposited by PLD on sapphire and annealed for 30 minutes	60
4.4 Deconvolution of V2p _{3/2} peak bonding states for as-deposited films. Values given represent the contribution to total peak area for each bonding state. . .	63
4.5 Layered structure of films deposited on silicon as determined by x-ray reflectivity measurements.	72
4.6 Layered structure of films deposited on sapphire as determined by x-ray reflectivity measurements.	74
4.7 Quantitative breakdown of elemental species observed in Figure 4.11.	78
5.1 Pump-probe techniques and ultrafast VO ₂ dynamics.	86
6.1 Sputtering Target Composition	111

6.2	Peak positions for electronic transitions in the monoclinic (A,B,C,D) and rutile states (AA,BB,CC,DD) as extracted by fitting the data.	122
B.1	Published work contributed towards vanadium dioxide understanding during time as a graduate student. Work covered in this dissertation is highlighted. .	150
B.2	Work contributed towards vanadium dioxide understanding during time as a graduate student. Work covered in this dissertation is highlighted.	151

LIST OF FIGURES

Figure	Page
1.1 Citations per year for "Vanadium Dioxide" as reported by Web of Science, December 2014.	3
1.2 Atomic Structure of VO ₂ M ₁ , M ₂ and R phase[31].	6
1.3 Band structure of vanadium dioxide as described by Goodenough[31]. . . .	7
1.4 Temperature stress phase diagram for vanadium dioxide single crystals[5]. .	9
1.5 a) Temperature and pump fluence phase diagram for vanadium dioxide film[40]. b) Distinct "phases" as determined by THz probe pulse.	10
1.6 Schematic representation of the hysteresis parameters.	10
2.1 Schematic representation of VO ₂ thin film bolometers, a and b. SEM images of VO ₂ based bolometers, c-e[68].	18
2.2 SEM image of silicon ring resonator structure with VO ₂ patch on ring, a. Experimental setup used to optically heat VO ₂ patch while monitoring 1550 nm transmission through waveguide, b. Measured shift in resonant wavelength due to VO ₂ phase transition, c[13].	19
2.3 VO ₂ FET, a and VO ₂ FET using ionic liquid gate, b[72].	20
2.4 False color SEM image of silicon VO ₂ electro-optic modulator, a. Schematic representation of the same device, b[14].	21
2.5 Cross section of VO ₂ silicon mechanical actuator, a. Thermally activated VO ₂ micro mechanical actuator above and below phase transition temperature, b[7]. VO ₂ mechanical memory device, c[9].	22
2.6 SEM image of Si-VO ₂ micro-ring resonator with 1.5 μm radius. The VO ₂ patch is highlighted in false-color. (scale bar is 250 nm)[13].	25
2.7 Schematic of the optical measurement set-up[13].	25

2.8	Spectral dependance of the optical transmission for 1.5 μm radius ring resonators with (bottom) and without (top) VO_2 patch. The top curve has been shifted by + 20 dBm for clarity[13].	26
2.9	Optical transmission of the 1.5 μm radius hybrid Si- VO_2 ring resonator as a function of wavelength, before and after triggering the SMT with a 532 nm pump laser. The lines are Lorentzian fits. Inset: IR camera images revealing vertical radiation at a fixed probe wavelength, $\lambda = 1568.78$ nm (dashed line)[13].	28
2.10	Temporal behavior of the optical transmission at $\lambda = 1568.78$ nm, in a 1.5 μm radius Si- VO_2 device. With 532 nm pump laser (a) ON and (b) OFF. (c) Images from the IR camera, at various times, highlighting the probe response observed in (b)[13].	29
2.11	(a) Normalized resonance shift after photothermally triggering the SMT for hybrid Si- VO_2 micro-ring resonators of different radii and the same VO_2 patch length $L_{\text{VO}_2} = 560$ nm. (b) Q-factor for the same devices before and after triggering the SMT. Inset illustrates the various decay channels affecting total Q-factor and an IR camera image showing vertical radiation from a 10 μm radius hybrid resonator when on-resonance in the semiconducting state[13].	31

2.12	Si-VO ₂ photonic devices and all-optical modulation. (a) Phase-change absorber where the SMT induces a broadband change in absorption Δ . SEM image of a compact Si-VO ₂ absorber with a 1 μm VO ₂ patch . (b) Phase-change ring resonator where the SMT induces phase modulation $\Delta\phi$. SEM image of compact Si-VO ₂ ring resonator with radius $R = 1.5 \mu\text{m}$ and a 500 nm VO ₂ patch. SEM scale bars are 1.5 μm . (c) Schematic of the experimental pump-probe set-up. Transmission is monitored with a photodetector and oscilloscope. Nanosecond-pulsed pump light is focused onto the device with a microscope objective (MO) and the power is controlled by a linear polarizer (P)[73].	33
2.13	Normalized probe transmission through Si-VO ₂ absorbers with (a) 1 μm and (b) 500 nm VO ₂ patch lengths. The pump fluence is varied from 0.5-8 mJ cm^{-2} . Inset shows a magnified view of the temporal response. (c) Transmission through a 500 nm Si-VO ₂ absorber from 1500 to 1600 nm, demonstrating that the SMT of VO ₂ can produce broadband absorption modulation. Plots are shifted for clarity[73].	34
2.14	(a) Transmission spectra for a Si-VO ₂ ring resonator with radius $R = 1.5 \mu\text{m}$. (b) Probe transmission at resonant wavelength ($\lambda = 1588.5 \text{ nm}$)[73].	35
2.15	(a) Saturation of the probe signal is observed above the threshold fluence of 1.27 mJ cm^2 . (b) Relaxation time, τ_{M-S} , from the metallic state to the initial semiconducting state for different pump fluences, plotted for Si-VO ₂ absorbers and ring resonators with 500 nm or 1 μm VO ₂ patches[73].	36
2.16	Spectral response of Si-VO ₂ ring resonator. Optical transmission for variable wavelength pump-probe measurements above threshold (1.9 mJ/cm^2). Right column shows magnified view of the same device along with a Si-only device pumped at 1.9 mJ/cm^2 and 11.5 mJ/cm^2 . Color bar indicates a logarithmic scale[73].	37

2.17	Analysis of Si-VO ₂ ring resonator. (a) Resonant wavelength vs. time, extracted from pump-probe measurements shown in Fig. 2.16. (b) FDTD simulation for a hybrid Si-VO ₂ waveguide, with Si dimensions 220 x 500 nm and a 70 nm thick VO ₂ patch on top. (c) Resonance wavelength blue-shift $\Delta\lambda_{max}$, in response to the photoinduced SMT in Si-VO ₂ ring resonators with varying radii and fixed VO ₂ patch length. Shaded area represents $\Delta\lambda < 0.3$ nm, corresponding to thermo-optic changes of resonators due to temperature variations[73].	38
3.1	The monoclinic M1 ((a) and (b)) and rutile R ((c) and (d)) structures of VO ₂ viewed along different directions. The translucent blue region indicates where the ErO ₆ clusters fit[91].	43
3.2	The Raman spectra of an as-prepared VO ₂ sample and another VO ₂ sample implanted with Er and annealed at 1000 °C. These spectra were recorded at (a) room temperature (22 °C) and (b) liquid N ₂ temperature (-195.6 °C). The green annotations show the VO ₂ Raman lines observed from the as-prepared sample and the red annotation shows the Si Raman, from the substrate. The unlabeled peaks in (b), are Er ³⁺ PL from the: ² H _{9/2} → ⁴ I _{13/2} and ⁴ S _{3/2} → ⁴ I _{15/2} transitions[91].	45
3.3	(a) Free-ion energy level diagram of Er ³⁺ , showing the transitions observed in the PL measurements. (b)(g) PL spectra for a VO ₂ sample with Er. Each spectrum corresponds to an electronic transition in (a) with the correspondingly color. The spectra in (b) were measured at three different temperatures (-195.6 °C, 22 °C, and 100 °C) as indicated; all other spectra in (c)(f) were taken at near-liquid N ₂ temperature (-195.6 °C). The peaks indicated by the shaded region in (g) are not due to the Er ³⁺ PL, but to the 2TO and the 2LO Raman modes of the Si substrate[91].	46

3.4	Total intensity of the Er^{3+} PL at 0.80580.8166 eV vs. the Er implantation fluence for two annealing temperatures. All data are obtained from measurements at room temperature using 532 nm excitation[91].	47
3.5	Temperature resolved reflectance for pure VO_2 annealed at 1000 C (a), and (b)Er implanted films annealed at 1000 °C. Black axes account for roughness dependent scattering, while red axes are the raw values. c-f) energy distribution for grains in the films. Color indicates heating or cooling. Distributions are plotted below their respective hysteresis curves[91].	48
3.6	The phase transition parameters are presented with respect to implantation fluence and for different annealing temperatures. The x axis coordinate labeled U indicates unimplanted samples. The hysteresis parameters are (a) the critical temperature, (b) the hysteresis width, (c) the dynamic range, and (d) the mean transition width[91].	49
3.7	Polarization spectroscopy at -195.6 °C with 532 nm excitation and 2 mW power. (a) Photograph of the $\text{VO}_2\text{:Er}$ crystal being measured. The width of the beam is approximately 15 μm . The polarization x-axis was oriented parallel to the crystal long axis. (b) Energy level diagram of Er^{3+} , showing the observed transitions. The measured PL spectra are shown in c-f. Different polarizations are plotted in each graph, as indicated in the legend. The positions of the Er^{3+} PL lines are labeled with purple texts (unit: eV). In f, the peaks labeled in orange are VO_2 Raman peaks, while the green peak is a Raman peak from the substrate[92].	51
4.1	a) I-V curves for different VO_2 waveguide based optical modulators produced by pulsed laser deposition. b) I-V curves for the same devices but with VO_2 produced by sputtering.	55

4.2	A) Optical hysteresis curve for VO ₂ thin film (deposited by PLD on glass and annealed for five minutes) measured in transmission at 1550 nm. B) Heating curve with sigmoidal fit and inset illustrating fit parameters. C) Cooling curve with sigmoidal fit[98].	57
4.3	XPS spectra (Black) of V2p _{3/2} peak for an as-deposited film sputtered on silicon. Peak deconvolution suggests the presence of four vanadium oxides, V ₂ O ₅ (blue), V ₆ O ₁₃ (orange), VO ₂ (green) and V ₂ O ₃ (red).[111, 112, 98] .	62
4.4	Optical hysteresis parameters measured across the thermally induced phase transition at 1550 nm. Lines connecting the data points are added to clearly demonstrate the trends with annealing time[98].	66
4.5	Film morphology evolution regimes, A) P_G_10, B) P_G_30, C) E_Sa_10, D) E_Sa_30 , E) S_Si_5 and F) S_Si_90. Detailed sample description is found in Table 4.3. All images are 2μm x 2μm[98].	68
4.6	AFM image of VO ₂ film (A) showing evidence of dewetting; fingering instability (B) and edge retraction (C)[98]. B and C reprinted with permission from the Annual Review of Materials Research, Volume 42 2012 by Annual Reviews, http://www.annualreviews.org	70
4.7	AFM images (top) are accompanied by schematics (bottom) to illustrate how dewetting drives the morphological evolution. Films initially show poorly defined grooves (A) P_Si_2. With longer annealing times the initial grooves deepen and new grooves form(B) P_Si_10 and with prolonged annealing edge retraction and fingering instability dominate the grain structure of the film(C) P_Si_30. All images are 2 μm x 2 μm[98].	71
4.8	a) VO ₂ high aspect ratio single crystal wire growing off the edge of a silicon substrate. b) Wires grown on sapphire exhibit the hexagonal symmetry of the substrate. c) Approximately 100 μm ² single crystal grown on a quartz substrate. d) SEM image of low aspect ratio single crystal cluster on silicon.	76

4.9	a,b) Preferential growth of VO ₂ nanobeams on solgel derived VO _x patterns after growth for 3 min and 2 h, respectively. (c) Formation of VO _x nanoparticles upon annealing of solgel derived thin film (dashed lines are a guide to the eye indicating location of the VO _x pattern) prior to growth. (d) Higher magnification image of (b) taken at the bottom right corner. Image taken from Kim[127].	77
4.10	a) High resolution TEM image of VO ₂ wire. b) HAADF image of VO ₂ wire.	78
4.11	EDS images of the the rounded end of VO ₂ wire pictured in Figure 4.10b. Letters in the upper left hand corner of each image indicate the elemental species being mapped.	79
4.12	a) Tunable dispersion meta-material.[130] b) Tunable emitter.[131] c) Switchable quarter-wave plate.[132] d) Meta-material perfect absorber.[133] . . .	81
5.1	Length and time scales for electronic and atomic dynamics. Figure taken from[137].	84
5.2	Phase transition time for different pulse durations. Figure taken from[143]. .	87
5.3	The changes in lattice constant($\Delta a/a$) and optical density(ΔOD) are plotted as a function of pump-probe delay for varying pump fluence. Figure taken from[20].	89
5.4	Changes in the optical transmission at 5 μm (inset) are plotted for different fluences and as a function of delay. The main graph shows changes in the ($30\bar{2}$) and (220) diffraction peak intensity for different pump fluence values. Figure taken from[29].	90
5.5	Response of VO ₂ films in white light pump-probe experiment A) below phase transition fluence and B) above fluence[38].	91
5.6	a) Change in reflectivity for a VO ₂ film at 525 nm excited at different fluences. b) Below F_{Th} behavior at 800 nm and 525 nm, inset shows Fourier transform of experimental data. Figure taken from[146].	92

5.7	Top: schematic of the atomic and electronic structure evolution in vanadium dioxide during the photoinduced phase transition. Bottom left and right: change in photoelectron spectrum when heating (left) and cooling (right). Integrated PE intensity ($0.2 \text{ eV} < E - E_F < 0.0 \text{ eV}$) shows hysteretic behavior (center)[28].	94
5.8	(a) Photoelectron spectra before (blue) and 1 ps after pumping (red, $6.7 \text{ mJ} = \text{cm}^2$). Inset: schematic showing of partial phase transition and film domain structure. (b) Thermally induced changes (green) and photoinduced changes (yellow, orange, red)[28].	95
5.9	(a) PE intensity change versus pump-probe delay close to E_F . Photoelectrons are detected immediately in the gap, showing the quasi-instantaneous collapse (cartoon energy axis is to scale). Integration of the PE intensity above (purple) and below (green) E_F yields the respective transients in (b). The empirical fit (black) quantifies the averaged hot electron(hole) lifetimes[28].	97
5.10	Schematic representation of the OPA pump white-light probe system at the Center for Nanophase Materials Science, Oak Ridge National Laboratory (courtesy of Aziz Boulesbaa)	100
5.11	Raw absorption data for variable wavelength pump, white-light probe measurements on VO_2 films at fluence values less than required to complete the structural phase transition. The pump wavelength used is recorded in the bottom left hand side of each plot. The color scale on each plot represents the absorption.	101
5.12	a) Raw absorption data at 492 nm when pumped at 800 nm. b) Absorption transient from a) with double exponential subtracted. Red line is a three-function fit to experimental data. The quality of the fit is quantified by the mean squared error (MSE) and displayed at the top.	102

5.13	Area of each oscillator (integral of each $A_i * e^{-B_i t}$ term) normalized to the total area with pump wavelength displayed at the top. See text for more detailed description.	104
5.14	Plot showing 1.7(red), 6(yellow) and 8(purple) THz modes and data (blue circles). Absorption at 570 nm for film pumped at 1500 nm is shown (blue circles).	106
6.1	Imaginary part of the VO ₂ dielectric function as measured along the monoclinic b_m (a) and a_m (b) crystal directions by Huffman[159]. (c) Large single crystal platelet of VO ₂ used in experiments by Huffman[159].	113
6.2	Imaginary part of the monoclinic dielectric function measured for a undoped VO ₂ film deposited on silicon. The vertical red dotted lines show the position of oscillators representing longitudinal modes while the black dotted lines indicate the position of those for the transverse modes, as used by Huffman[159]. Two oscillators are used to capture the asymmetry of the longitudinal mode between 600 and 650 cm ⁻¹	114
6.3	Imaginary part of the monoclinic phase dielectric function measured for undoped and doped VO ₂ films deposited on silicon. The curves are shifted vertically for clarity. Features which evolve with increased tungsten doping are noted by A and B along with vertical lines.	115
6.4	Imaginary part of the rutile phase dielectric function measured for undoped and doped VO ₂ films deposited on silicon. The curves are shifted vertically for clarity.	116
6.5	Peaks in Raman spectra that soften with increasing tungsten concentration at (a) ~ 194 cm ⁻¹ and ~ 225 cm ⁻¹ and (b) ~ 615 cm ⁻¹	117
6.6	Imaginary part of the rutile phase dielectric function measured for undoped and doped VO ₂ films deposited on silicon. The curves are shifted vertically for clarity.	118

6.7	Absorption measurements for undoped and doped VO ₂ films deposited on silicon at 25 C a) and 85 C b). The curves are shifted vertically for clarity.	119
6.8	Electronic structure of monoclinic VO ₂ , from Qazilbash[162]. Red arrow indicates transition observed in this work but not in the original paper.	120
6.9	Absorption spectra for a monoclinic phase undoped VO ₂ film deposited on silicon. The blue points are fit by summing up multiple Gaussian + Lorentzian functions to determine the energy of various electronic transitions.	121
6.10	Imaginary part of the monoclinic phase dielectric function measured for undoped and doped VO ₂ films deposited on silicon. The curves are shifted vertically for clarity.	122
6.11	Atomically resolved strain maps for tungsten doped VO ₂ . [158] Blue regions show tensile strain (+15%) and yellow indicate compressive strain (-15%).	123
6.12	Density functional theory calculations showing the phonon density of states for pure VO ₂ in black and W doped (~1 %) VO ₂ in red [161].	125

Chapter 1

Introduction to VO₂: The Basics

In this dissertation, we explore the fundamental physical properties and material processing methods that will be required to successfully design and fabricate the next generation of optical modulators based on the vanadium dioxide (VO₂) phase transition. We describe the fabrication and performance of the first generation of compact, high-speed and all-optical modulators which take advantage of the VO₂ phase transition.

1.1 The Problem

As the quest for faster, more efficient and more compact computers continues, a number of problems arise with current silicon-based electronics including: thermal management, interference and bandwidth. Switching to optical-based computing and signal processing is one approach that solves many of these problems. The requirements for active materials in optical computing are demanding:

- Optical modulation at GHz speeds or faster.
- Optical modulation depth of at least 1 dB with 100 fJ or less input.
- Possible to modify properties by doping.
- Optical response to excitation at ~ 1550 nm.
- Processing compatible with current silicon technology

However, relatively few materials can meet these requirements under normal conditions. Vanadium dioxide, on the other hand, may satisfy these requirements.

We show how to combine VO₂ with existing silicon photonic structures to produce compact, high-speed optical modulators. The performance of these devices is presented

and the physics and processing of VO₂, as relevant to high speed optical modulation, is explored.

- We demonstrate all-optical devices capable of performing at GHz speeds, which are only limited by the laser pulse duration, and perform experiments indicating that THz modulation is possible.
- We report modulation depths up to 7 dB along with shifts in the resonant wavelength of up to 3 nm.
- We show that tungsten and erbium doping modifies the optical properties.
- We explore the femtosecond phase transition dynamics when excited at a range of wavelengths from 400 nm to 1500 nm.
- We explore fabrication methods which provide additional paths to tune the phase transition properties.

We do not observe fundamental issues which would prevent VO₂ from satisfying the material requirements for optical modulators.

1.2 Brief History of VO₂ Research

The metal-insulator transition in vanadium dioxide (VO₂) was first observed by Morin[1] at Bell Telephone Laboratories in 1959. In Figure 1.1, the number of citations per year for VO₂ is plotted from 1966 to 2015. From 1966 to 1992 the number of citations remained relatively constant at approximately fifty to one hundred per year. From 1992 thru 2013, the number of citations grew exponentially to 6000 and maintained that value for 2014. This growth can be attributed to the significant interest VO₂ has attracted across multiple fields including physics, engineering, chemistry and materials science. VO₂ is interesting not only for its possible applications but also as a model material for exploring the behavior of strongly correlated systems. In this introductory Chapter, the physical properties of VO₂

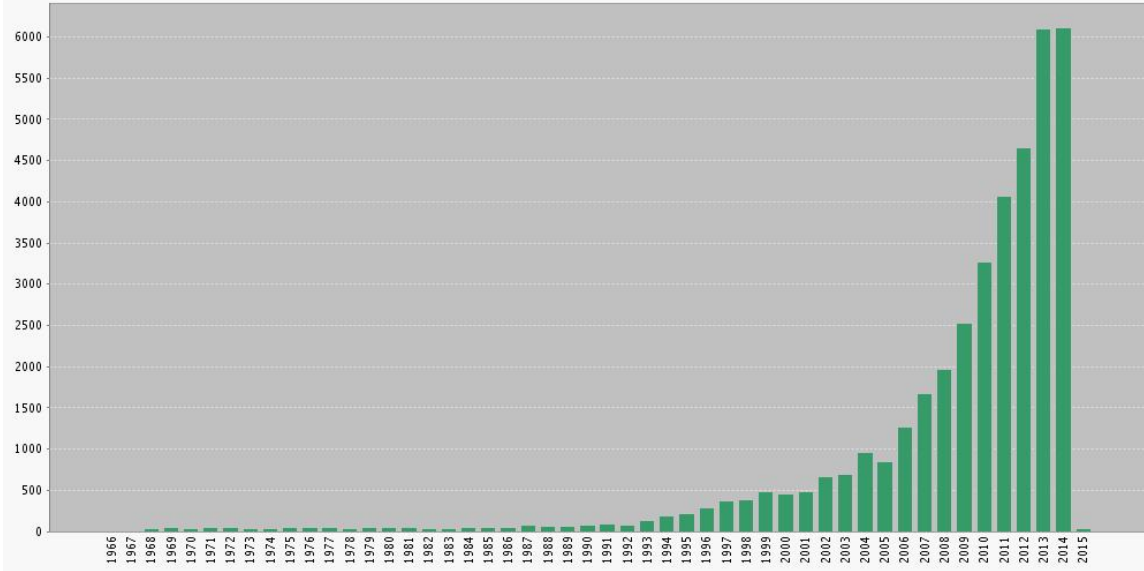


Figure 1.1: Citations per year for "Vanadium Dioxide" as reported by Web of Science, December 2014.

are discussed and some common applications are mentioned. In-depth discussions of these topics are provided in the subsequent chapters.

1.3 Properties of Vanadium Dioxide

The thermally induced metal-insulator transition, as observed by Morin[1] is certainly the most well known trait of vanadium dioxide. A change in conductivity up to five orders of magnitude[2] has been observed in single-crystal samples and is accompanied by a structural transition from rutile[3] in the metallic state to monoclinic[4] in the insulating phase. In Table 1.1, additional properties of VO_2 that vary across the phase transition are presented. Four distinct crystal phases are observed in pure and doped VO_2 [5, 6]; two monoclinic (M_1 and M_2), one triclinic (T) and one rutile (R). The unit cell expands along the rutile c-axis during the transition and can be harnessed as a mechanical actuator[7, 8, 9]. While useful in thin film applications, the c-axis expansion proves destructive for large crystals, which can only survive relatively few phase transition cycles before breaking. Thin films on the other hand, have demonstrated millions of phase transition cycles with-

Table 1.1: Tabulation of vanadium dioxide properties above and below the phase transition.

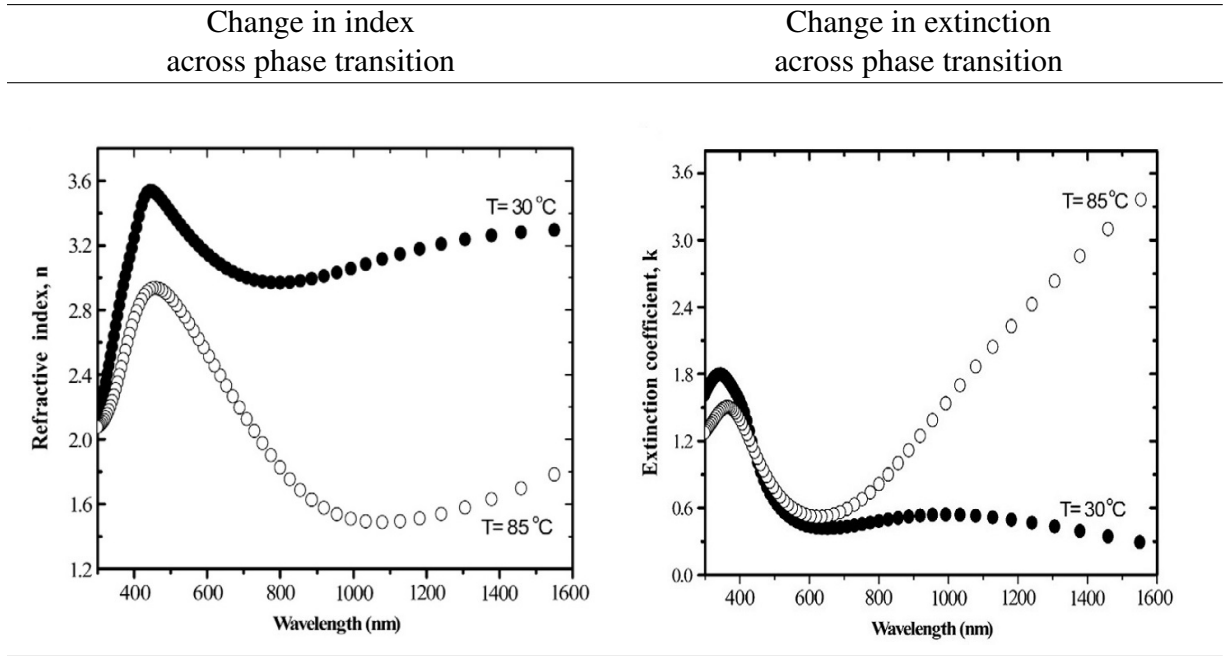
Property	Below T_c Value	Above T_c Value	Change	Reference
Crystal Structure	Monoclinic (M_1) $P2_1/c$	Rutile (R) $P4_2/mnm$	-	[4, 3]
Density	4.57 g/cm ³	4.65 g/cm ³	0.08 g/cm ³	[20]
Thermal Conductivity	3.5 W/(mK)	6.0 W/(mK)	2.5 W/(mK)	[21]
Heat Capacity	0.656 J/(gK)	0.78 J/(gK)	0.13 J/(gK)	[22]
Thermal Expansion Coefficient	-	-	$4.87 \times 10^{-6}/K$	[23]
Latent Heat	-	-	51.8 J/g	[24]
Entropy	-	-	$(3.0 \pm 0.3)k_B$	[5]
Young's Modulus	140 GPa	140 GPa	-	[25]
Fracture Stress	5.2 GPa	5.2 GPa	-	[25]
Work Function	5.15 eV	5.30 eV	0.15 eV	[26]

out degradation[10].

The large change in electronic structure across the phase transition produces significant contrast between the dielectric constants of the metallic and insulating phases, index (n) and extinction coefficient (k)[11], shown in Table 1.2. In the UV/VIS spectral range the contrast is quite small but increases into the IR with $\Delta n = -1.6$ and $\Delta k = 3$ at the center of the optical communication band, 1550 nm. The large change in optical properties has attracted interest for use in optical switching devices[12, 13, 14], thermal management[15, 16], metamaterials[17, 18] and plasmonic[19] applications.

Considering all of the published work about VO₂ might lead to the conclusion that it is well understood; however, recent work has shown that it is actually a much more complicated material than previously thought. In general, theoretical understanding of the physics behind the phase transition has not kept pace with experiment. In 2010 Cao[27] suggested the possibility of a triple point and in 2013 Park[5] conclusively demonstrated that a solid-state triple point exists for VO₂ where M_1 , M_2 and R phases coexist. In addition, the recent work of Wegkamp[28], Morrison[29] and Laverock[30] has shown that a monoclinic metal can exist in both the optically and thermally induced phase transitions. This recent work demonstrates that there is still much to be learned about the behavior and physics of the VO₂ phase transition.

Table 1.2: Optical Properties of VO₂ thin film above and below the phase transition[11].



1.3.1 Structural Transition

Interest in vanadium dioxide has long been centered around how the atoms re-arrange themselves during the phase transition with the aim of understanding the driving mechanism for the phase transition. The Peierls and Mott-Hubbard models have been the primary theories under consideration. In the Peierls model, the structural transition is driven by the instability of a one-dimensional chain of metal atoms (along the rutile *c*-axis), which can form a lower energy configuration by dimerization. The Mott-Hubbard model is based on the competition between inter-atom electron mobility (hopping integral) and the intra-atom Coulomb repulsion. Although four phases are known to exist (M_1 , T, M_2 and R), most work discusses only two (M_1 and R). In Figure 1.2 the atomic structure of the three most studied phases is presented.

In the R phase, both the metal and oxygen atoms occupy equivalent positions. In the M_2 phase, half of the vanadium atom chains have become dimerized along the *c*-axis (purple atoms) while the other half are tilted (orange atoms) but still equidistant. This produces

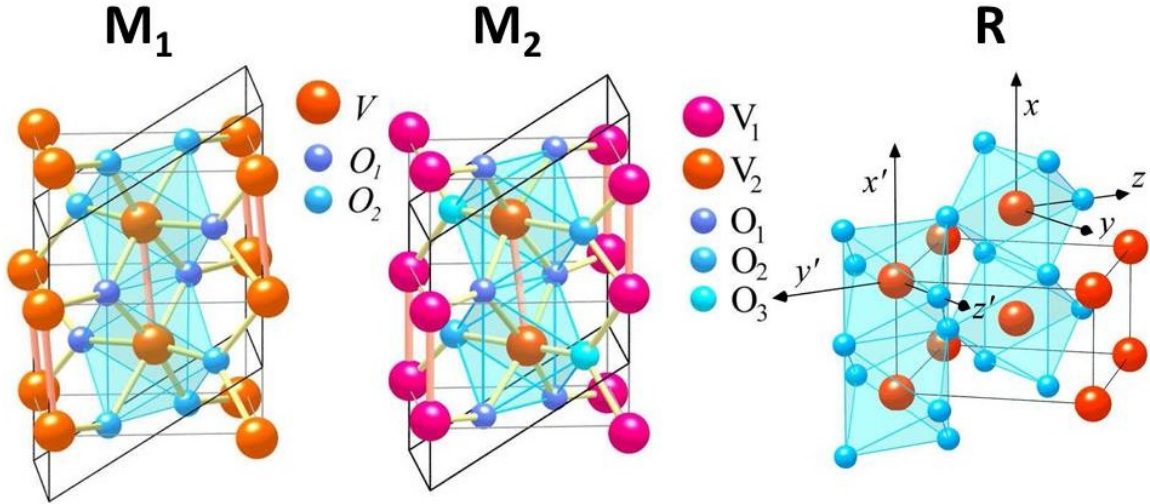


Figure 1.2: Atomic Structure of VO₂ M₁, M₂ and R phase[31].

three different bonding environments for the oxygen atoms. In the final low temperature state, all the vanadium atoms are dimerized and tilted along the c-axis and two distinct oxygen atom environments exist (lavender O₁ and blue O₂).

1.3.2 Electronic Transition

An explanation for the band structure changes near the Fermi energy that result from the phase transition, Figure 1.3, was first proposed by Goodenough[32] and is still widely accepted. In this picture, Figure 1.3a, the octahedral crystal field of the oxygen atoms splits the t_{2g} states into a $d_{||}$ state directed along the rutile c-axis and the π^* states. When in the monoclinic state, the vanadium atom dimerization splits the $d_{||}$ band into bonding and antibonding states. The dimerization also moves the π^* band to higher energy, resulting in a band gap of ≈ 0.7 eV.

1.3.3 Triggering the Phase Transition

The simplest and most common method used to induce the phase transition is heating; in pure films the transition occurs at 67 °C. The exact mechanism responsible for the transi-

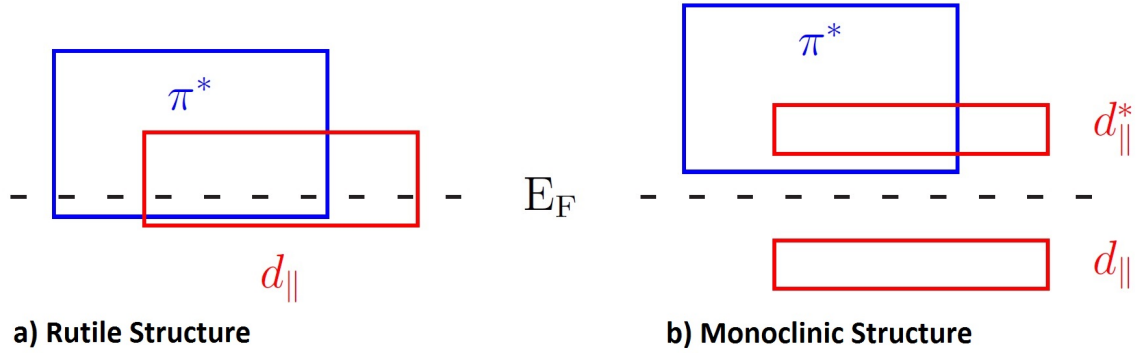


Figure 1.3: Band structure of vanadium dioxide as described by Goodenough[31].

tion is still debated, with Mott-Hubbard and Peierls mechanisms both explaining some aspect; however, recent work seems to favor the Mott-Hubbard explanation[29, 30]. Dopants, such as tungsten and molybdenum, reduce the phase transition temperature by stabilizing the metallic phase to well below room temperature; however, this occurs at the expense of electrical and optical contrast between the phases. Strain may also be used to trigger the phase transition and is most commonly used for this purpose in single crystals[27, 5]. Initially Cao[27] explored the physics of strain in single crystals and mapped out a phase diagram which was refined later by Park[5]. Controlled strain has also been used to probe the physics of VO₂ in thin films and systematically reduce the phase transition temperature[33].

Using an electric field to induce the phase transition has long been a goal for many researchers[34, 35, 36, 14], however, clear evidence for electric field switching has not yet been reported. In most cases the electric field required to trigger the phase transition is almost equal to the breakdown voltage, making it difficult to determine if the applied field or Joule heating due to electric current is responsible for the switching. The Poole-Frenkel effect, where an applied electric field increases electron mobility, appears to play a major role in the electric-field-induced phase transition[36, 14].

Optical excitation by femtosecond pulses can initiate the phase transition, however, the physics is significantly different from thermal excitation. According to van Veenendaal[37], the transition is set into motion by photoinduced orbital imbalance between the $d_{||}$ and d_{π}

bands which in turn drives coherent motion of the vanadium dimers into the rutile phase. The coherent motion of the V-V dimers is an important driving force for the phase transition and serves as a indicator for the structural transition as shown by Wall[38]. In general, a fluence of 7-10 mJ/cm² at 800 nm is required to complete the phase transition, however increased temperature can be used to reduce the fluence, as demonstrated by Pashkin[39] and Cocker[40]. The majority of ultrafast measurements have been performed using 800 nm light, more than twice the optical band-gap of 0.67 eV in the semiconducting state. In section 5.4 we present the first experiments to examine the dynamics when pumping close to the band-edge.

1.3.4 Phase Stability

The exact conditions under which the four phases of VO₂ are stable has only recently been determined in studies of single crystals by Park[5]. By performing electrical and optical measurements while carefully controlling the strain and temperature of single crystal wires, they mapped out the phase diagram (Figure 1.4) and observe a solid-state triple point where the M₁ M₂ and R phases coexist. The triple point is found to be at the critical temperature of $T_c = 65 \pm 0.1$ °C. Three phases, M₁ and M₂ and R can coexist.

Another type of phase diagram, which explores the influence of temperature on time resolved dynamics in the THz region, was mapped out by Cocker[40]. Using 0.5-2 THz probe pulses and a variable temperature stage, four phases are mapped out, as shown in Figure 1.5. In region A, the fluence and temperature are not sufficient to generate a response the looks anything like the metallic state, a sharp spike is observed around T₀ due to coherence. In region B, an "intermediate metallic state" is observed where metallic islands are present on a monoclinic lattice and cannot grow. In C, isolated islands of rutile VO₂ nucleate and over time expand to cover the entire film. In region D the entire film is driven into the metallic state in less than 500 femtoseconds. This work supports the existence of an "intermediate metallic state" where THz signatures of the insulator-to-metal transition are

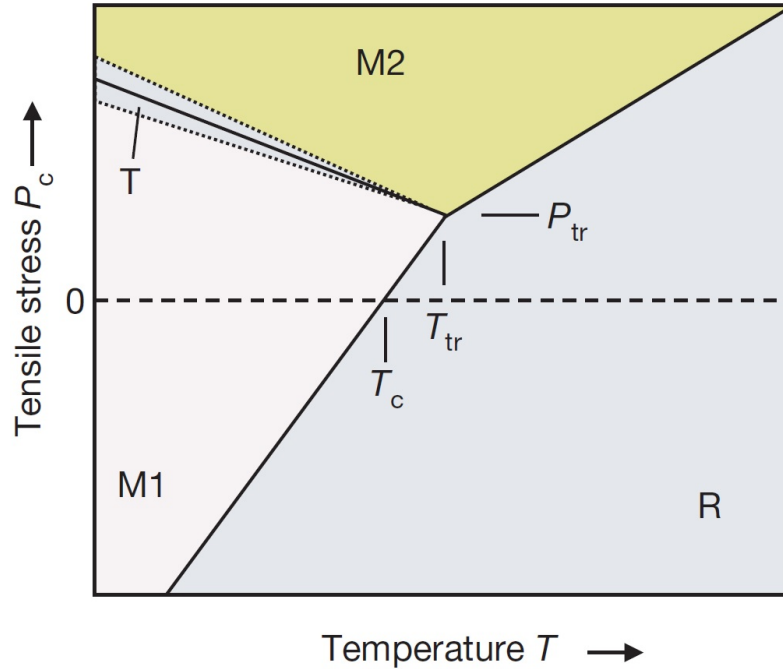


Figure 1.4: Temperature stress phase diagram for vanadium dioxide single crystals[5].

present before the structure has had time to move. Cocker concludes that a critical density of excited electrons and phonons is required to complete the structural phase transition.

1.3.5 Hysteresis Width and Contrast

The phase transition hysteresis width and contrast are important properties for devices and understanding the phase transition physics. If the insulator-metal(IM) transition temperature is defined as point A in Figure 1.6, and the metal-insulator(MI) transition is defined as point B, then the hysteresis width is the temperature difference $T_{IM} - T_{MI}$. The optical contrast is defined as a change in transmission or reflection and represented by C in Figure 1.6. The contrast is related to the thickness of the film and the composition; portions of a film which are not VO_2 will not switch and contribute to the contrast.

The origin of the hysteresis width is more complicated. To understand this, consider a thin film in which all grains are identical. T_{IM} and T_{MI} will be the same for all grains and the resulting hysteresis will be narrow, approaching that of a single crystal. Considering

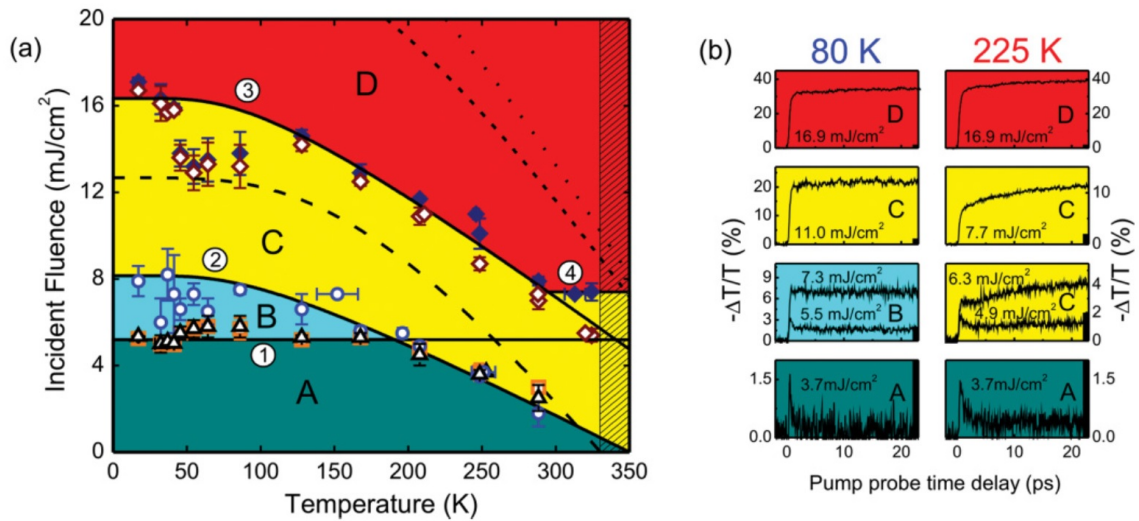


Figure 1.5: a) Temperature and pump fluence phase diagram for vanadium dioxide film[40]. b) Distinct "phases" as determined by THz probe pulse.

a film composed of two different sized grains, each grain size will have a unique T_{IM} and T_{MI} . The hysteresis width for this film will be slightly larger than for the film with identical grains. The hysteresis width can be thought of as a measure of the grain uniformity within a film. Films with a narrow distribution of grains will have a narrow hysteresis while films with a broader distribution will have a wider hysteresis.

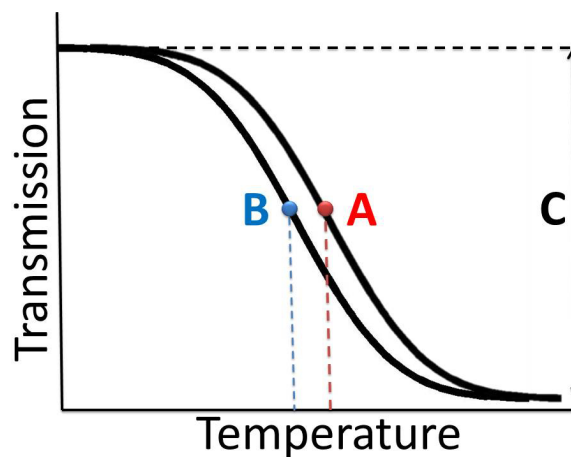


Figure 1.6: Schematic representation of the hysteresis parameters.

1.3.6 Defects

Any disturbance in the periodicity of a crystal is considered a defect. Crystallographic defects can occur inside or on the exterior of a crystal domain. A interface or surface can also be considered as a defect since the periodicity of the atomic lattice is disturbed. Crystallographic defects such as point defects (vacancy or dopant) are known to play an important role in determining the hysteresis parameters. Appavoo[41] observed a reduction in the phase transition energy attributed to oxygen vacancies formed by strain at the grain boundaries. Suh[42] found that the width and shape of the hysteresis depends on the density of transition-nucleating defects. Electrical hysteresis measurements performed with current flowing perpendicular to twin boundaries produced much larger contrast across the transition than when conducted parallel to the twin boundary[43]. It is clear that in VO₂ crystallographic defects play an important role in determining the hysteresis parameters.

The value of an epitaxial interface for tailoring thin film properties has long been known and VO₂ is no exception[44]. Films on sapphire and TiO₂, which provide an epitaxial interface, are known to have sharper hysteresis curves and higher electrical and optical contrast than films without an epitaxial interface. In addition, the epitaxial relationship has allowed molecular beam epitaxy (MBE) processes to produce switching films as thin as 2.3 nm[45]. Careful control of strain by tailoring the thickness of a RuO₂ buffer layer between VO₂ and TiO₂ allowed Aetukuri[33] to modulate the transition temperature from 345 K to 285 K. For single crystals, strain has been shown to influence the transition temperature and affect phase coexistence[27, 5]. In Chapter 4.2, the hysteresis parameters are examined for thin films fabricated on glass, silicon and sapphire substrates.

1.3.7 Temporal Response

Many groups have contributed information to help unravel the VO₂ metal-insulator transition on femtosecond time scales[46, 47, 39, 48, 40, 49, 29]. Current understanding of

the physics separates the structural and electronic portions of the phase transition. Under femtosecond laser excitation, the electronic structure transitions from semiconducting to metallic in under 100 femtoseconds. The monoclinic structure begins the transition to rutile under a few picoseconds but may take much longer to complete. In Chapter 5.2, a more complete discussion of the temporal behavior is provided. Results from the first experiments are presented and definitively show that the electronic structure collapses in under 100 femtoseconds. We also explore for the first time the phase-transition dynamics in the region below the critical fluence (F_{TH}) for VO₂ films excited by 400, 800, 1200, 1400 and 1500 nm sub-100 femtosecond pulses.

1.3.8 A Monoclinic Metal

The femtosecond change in optical and electrical properties during the IM transition has made VO₂ a material of interest for high speed switching applications, however, the nanosecond time scale MI transition recovery is unacceptable in most applications. Nag first demonstrated[50] that the electronic transition occurs first and can be separated from the structural transition by comparing temperature resolved optical and structural measurements. The recent work of Tao[51], Laverock[30], Morrison[29] and Wegkamp[28] has shown that the metallic properties of VO₂ can be observed while maintaining the monoclinic crystal structure. It now seems likely that the VO₂ phase-transition could be triggered on femtosecond time scales with just the right fluence to induce the electronic transition without triggering the full structural transition.

In the thermal regime, Laverock[30] showed that careful film growth on (110) TiO₂ substrates produces a grain structure which when heated will show all the signatures of the electronic phase transition while maintaining the monoclinic structure. In ultrafast measurements, where VO₂ is excited to a non-equilibrium state, Wegkamp[28] observed by time-resolved photoelectron spectroscopy an almost instantaneous transition to the metallic state. The details of this work are presented in section 5.2. Combining ultrafast electron

diffraction and infrared transmission, Morrison[29] found that electronic signatures of the metallic phase emerged while the structure was clearly monoclinic. These discoveries have not only revived the possibility of using VO₂ for high speed switching applications but have also confirmed that VO₂ can exist as a "monoclinic metal" even under equilibrium conditions!

1.4 Materials Platforms for Optical Modulators

1.4.1 Limitations of Silicon-Based Electronic Modulators

Silicon electronics have contributed more to human societal and technological advancements in the last fifty years than any other technology and the full impact will not be known for many years to come. However, if current trends in computing speed, device size and power use are to continue, all-electrical and all-silicon devices will not be the answer. The most serious issues related to the continued miniaturization of silicon based electronics are:

- Resistive losses and the thermal dissipation requirements associated with Joule heating in copper interconnects.
- Electromagnetic noise and electronic signal interference.
- Increased cross talk and power consumption for high-speed electronics in close proximity[52, 53].

Ultimately, quantum and molecular computing technologies may provide the best solutions but these are entirely new technologies. Switching to optical information transfer eliminates the concerns listed above while at the same time taking advantage of the existing complementary metal oxide semiconductor (CMOS) production infrastructure, materials supply and technical knowledge base.

As the fundamental performance limitations of silicon are approached, multi-core processing has emerged as the near-term solution. Multi-core processing is only effective if

high-speed communication exists between multiple cores and currently copper interconnects are fulfilling this requirement. But copper interconnects consume 80% of a microprocessor's power[54], much of which is converted to heat. In contrast, when light propagates in a medium without absorption, little to no heat is generated. Photons are not affected by electromagnetic noise and they do not suffer from the same types of interference phenomena. Optical interconnects can also be thought of as parallel communication channels (wavelength division multiplexing) since photons of different wavelengths can travel together simultaneously without interacting. With all of these benefits, there has been significant effort made by Intel[55], IBM[56] and others towards incorporating optical interconnects into silicon based electronics.

Low-loss optical transmission fibers have been known since 1970, and methods exist to produce relatively low-loss silicon waveguides[57]. The challenge is to develop compact, efficient and high-speed silicon optical modulators[58]. Any optical modulator design must incorporate an active material which experiences a change in index (Δn) or change in absorption ($\Delta\alpha$) in the presence of an electric field or under optical excitation. When an acceptable material has been identified, interferometer or resonator based designs are typically used to produce a modulator. In a interferometer based device, the index change in the active material is used to shift the phase relationship between two propagating waves, resulting in constructive or destructive interference. For a resonator based approach, the active material is used to tune the device in and out of resonance, switching between on and off states. In general, interferometer based devices have larger bandwidth (about 20 nm) but this comes at the expense of increased physical size. Resonator based devices are significantly more compact but have 10-100 times less bandwidth[59].

In most semiconductor materials, the electric field-induced change in optical properties is due to the Pockels effect, Kerr effect and Franz-Keldysh effect[58]. Unfortunately, at the relevant telecommunications wavelengths of 1.3 μm [60] and 1.55 μm [61], these effects are too weak in silicon (and most other materials) to be useful. Optical modulation is

most commonly achieved by increasing the concentration of free charges, which modulates the real and imaginary parts of the dielectric function[61]. Current "state of the art" all-silicon devices and their performance metrics are tabulated by Reed[58]. In Chapter 2.2 we consider VO₂ as an active material for optical modulators using resonator devices and waveguides. We modulate the resonant condition by triggering the VO₂ phase transition thermally and with CW and nanosecond pulse light. In addition, we produce electrically activated modulators by directly depositing a VO₂ on a silicon waveguide.

1.4.2 Limitations of Other Materials

As mentioned in the previous section, silicon and most other semiconductors do not have large optical responses when excited by electric fields or intense optical fields, however, other materials do. For example, crystalline to amorphous phase transitions in materials like Ge₂Sb₂Te₅ result in the dielectric function changing by 30% in 100 femtoseconds, after optical excitation[62]. This large change in the dielectric properties is quite desirable for optical data storage, flexible displays, and optical circuits, however the transition is not reversible if the material is fully amorphized. Many pnictides exhibit superconducting phase transitions and large changes in the magnetic properties; however, these only occur under high pressure[63] or at low temperature[64]. Manganites such as LaPrCaMnO[65] have large magnetic phase transitions; however, these occur at temperatures below that of liquid nitrogen. Vanadium dioxide does not have large changes in the optical, electrical or structural properties when compared to other materials; however, the changes occur under conditions that are readily accessible. The significant interest in VO₂ has been driven largely by the ease with which the phase transition can be triggered.

1.5 Outline of Dissertation

This dissertation is structured as follows.

1. Chapter 1: VO₂ has large reversible changes in the electrical, optical and structural properties under "normal conditions".
2. Chapter 2: We demonstrate optical modulation with silicon based devices incorporating VO₂ as an active material.
3. Chapter 3: We dope VO₂ with erbium and use the phase transition to modulate optical emission.
4. Chapter 4: We examine the properties of vanadium dioxide thin films and crystals fabricated by different methods.
5. Chapter 5: We study the non-equilibrium phase behavior of vanadium dioxide by time-resolved laser spectroscopy.
6. Chapter 6: We measure the optical constants of tungsten doped films and explore the underlying physics.

Chapter 2

Optical Modulation with VO₂

2.1 Introduction

In the previous Chapter, we presented the physical properties of VO₂ which make it a promising material for compact optical modulation devices and described some of the limiting factors in current electronic computing technology. There are very few materials that exhibit large, high-speed changes in their optical properties under normal conditions. In this Chapter we survey the wide range of applications that have been proposed for VO₂ and then focus on compact optical modulators. We choose the ring-resonator device geometry for its compact size and high sensitivity to changes in local optical properties. The performance characteristics of these devices are presented.

2.2 Background: VO₂ Based Devices

The abrupt change in optical, electrical and structural properties that are part of the VO₂ phase transition make it appealing for a wide range of nano/micro-scale devices. Bolometers were the first optical device application of vanadium dioxide[66, 67, 68], followed by plasmonic applications[69] and silicon ring resonator (SRR) based devices[12, 13]. Some of the first devices built in the field effect transistor (FET) geometry were produced by the research groups of Ramanathan[70] and Kim[34]. More recent work has examined the FET geometry using ionic liquids as the gate[71, 72]. The first devices to take advantage of the structural phase transition were fabricated by the Wu group[8, 7], and are described below.

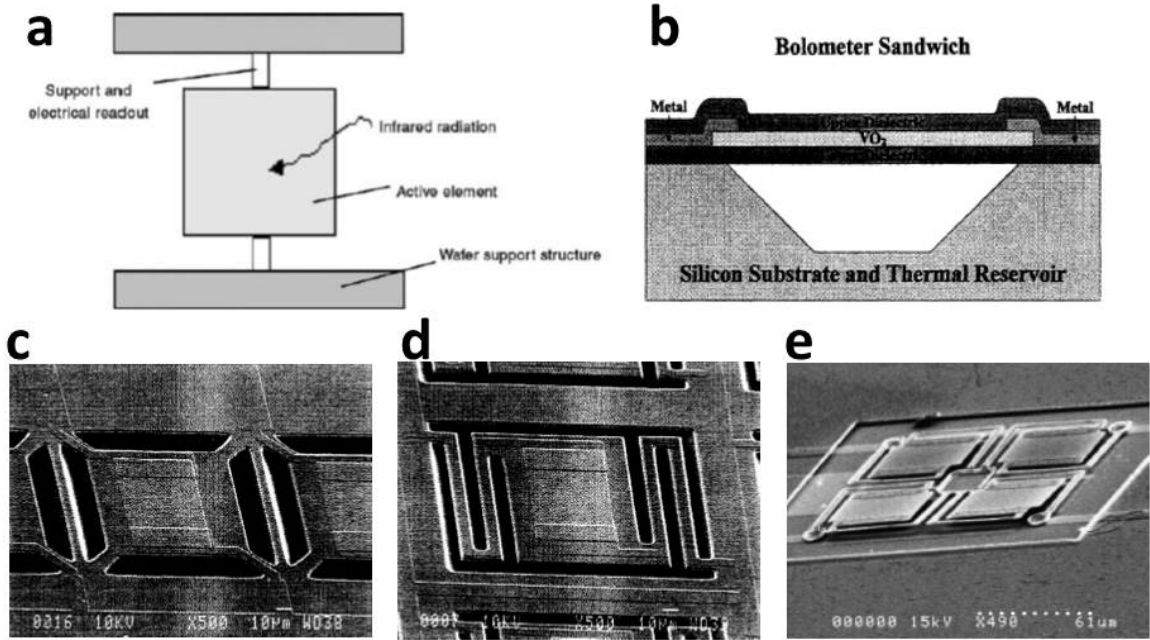


Figure 2.1: Schematic representation of VO₂ thin film bolometers, a and b. SEM images of VO₂ based bolometers, c-e[68].

2.2.1 Optical

The basic structure of a bolometer is quite simple, as shown in Figure 2.1 a and b, and consists of two components, an active material and a electrical readout. The active material responds to infrared radiation by a change in resistance, which is monitored by the electrical readout. Since the VO₂ phase transition can be triggered thermally, modified by doping and is accompanied by a large change in electrical resistance, it is an ideal material for this application. Various device geometries Figure 2.1 c-e have been employed to optimize the responsivity, noise equivalent power, detectivity and response time[68].

All-optical communication and computation circuits are an area of active research which may overcome the speed and space limitations of current silicon based electronics. The silicon ring resonator structure is one promising device geometry which has been integrated with VO₂ to produce all-optical modulation[13, 73]. In the simplest form, this device consists of a ring which is placed in close proximity to a waveguide, as shown in Figure 2.2 a. Under certain conditions, light can couple into the ring structure, resulting in

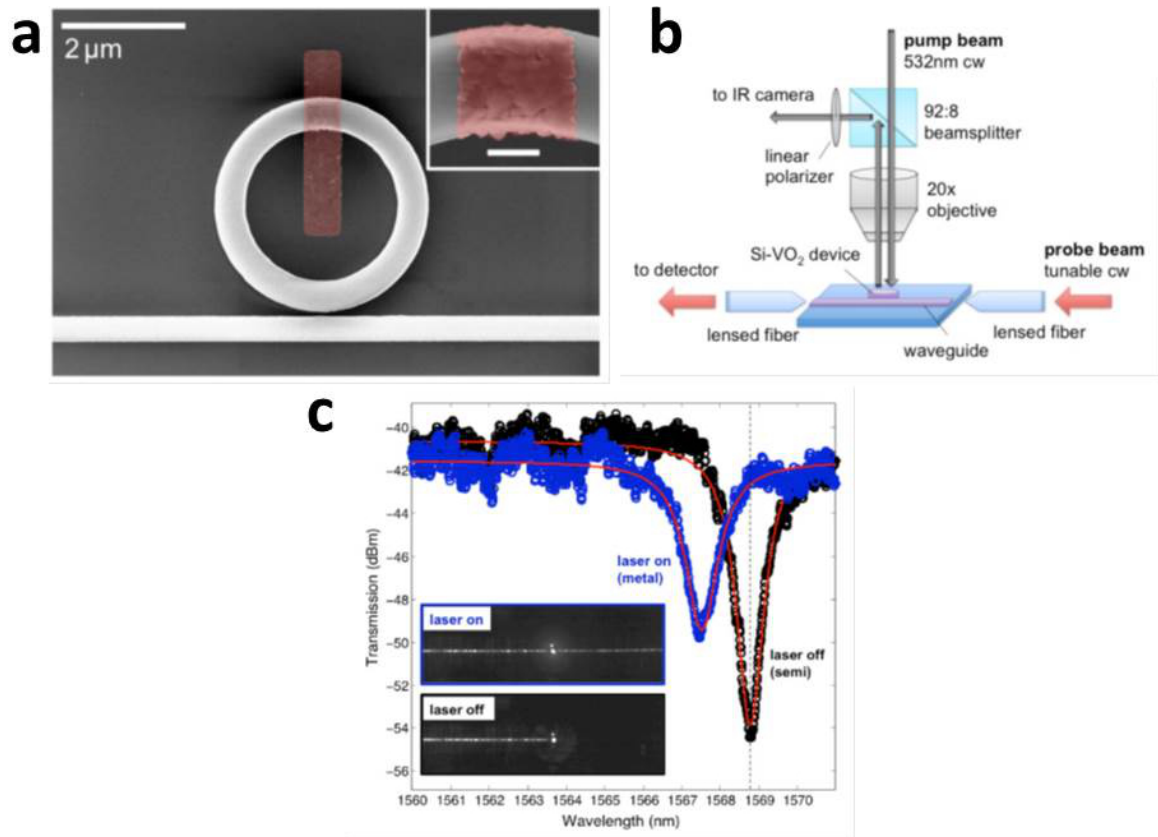


Figure 2.2: SEM image of silicon ring resonator structure with VO_2 patch on ring, a. Experimental setup used to optically heat VO_2 patch while monitoring 1550 nm transmission through waveguide, b. Measured shift in resonant wavelength due to VO_2 phase transition, c[13].

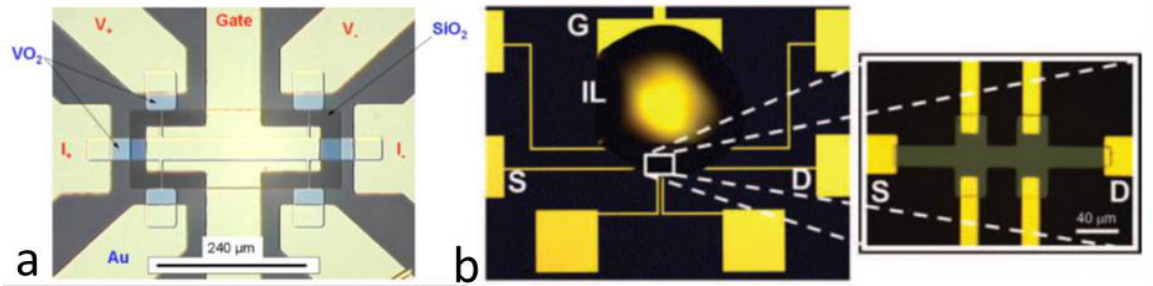


Figure 2.3: VO₂ FET, a and VO₂ FET using ionic liquid gate, b[72].

modulation of light through the waveguide. Modulation of the coupling by using VO₂ was first demonstrated by Briggs[12] who observed 6.5 dB modulation upon heating the entire device. Later Ryckman[13] used an all-optical setup, shown in Figure 2.2 b, to switch a VO₂ patch while monitoring transmission through the waveguide. A shift in resonance wavelength of ~ 1.2 nm was observed along with ~ 10 dB modulation in transmission, Figure 2.2 c. Subsequent work using nanosecond laser pulses demonstrated the possibility of GHz switching[73] and future experiments will attempt to demonstrate THz switching speeds.

2.2.2 Electrical

Many of the early experiments on VO₂ were performed on single crystals, which demonstrated large changes in resistance across the phase transition; however, few phase-transition cycles were possible without cracking the crystal. Thin films, however, do not suffer from this and using VO₂ in the field effect transistor (FET) geometry, Figure 2.3a, has been a goal of many research groups[74, 34, 75, 70, 17, 72, 71]. Currently, reversible modulation of the VO₂ channel conductivity has been demonstrated by applied voltage; however, current leakage through the gate dielectric is still an issue[70]. Ionic electrolyte gating, Figure 2.3b, has also been demonstrated, but electric field induced oxygen vacancy formation stabilizes the metallic phase to temperatures below 5 K, suppressing the metal-insulator transition[72].

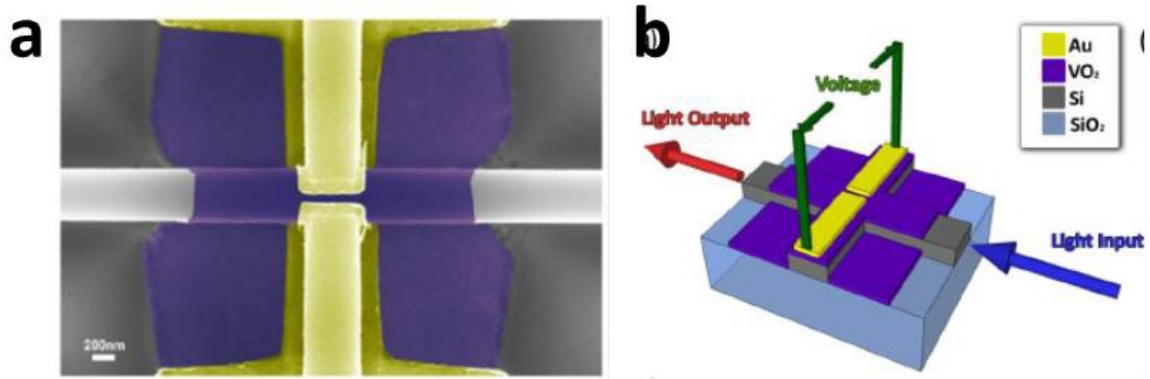


Figure 2.4: False color SEM image of silicon VO₂ electro-optic modulator, a. Schematic representation of the same device, b[14].

At Vanderbilt, we have produced electro-optic modulators which incorporate VO₂ as the active element. The typical device structure is shown in Figure 2.4a and b, where a patch of VO₂ is deposited on a silicon wave guide. Electrical contacts are then deposited on top of the VO₂ and used to switch the patch, resulting in modulation of light transmission through the wave guide. Unlike the SRR designs described previously, an electro-optic modulator can be used to directly convert a electrical signal into an optical one.

2.2.3 Mechanical

Mechanical devices represent the most recent application of the VO₂ phase transition, taking advantage of the 2% change in strain, due to the c-axis expansion across the phase transition[7]. These actuators, as shown in Figure 2.5 a and b, have proven to be extremely efficient, operating at two-thirds of the Carnot cycle efficiency between 27 - 68 °C and capable of oscillating at 4.5 kHz when driven by pulsed laser[7]. Micro-electro-mechanical memory devices have been realized, Figure 2.5c, by harnessing the structural phase transition to power cantilever type devices[9]. Incorporation of a metallic heater into the cantilever devices allowed for active control and feedback, via a change in heater resistance, producing 30 μm deflection and no degradation after 12,000 cycles[9].

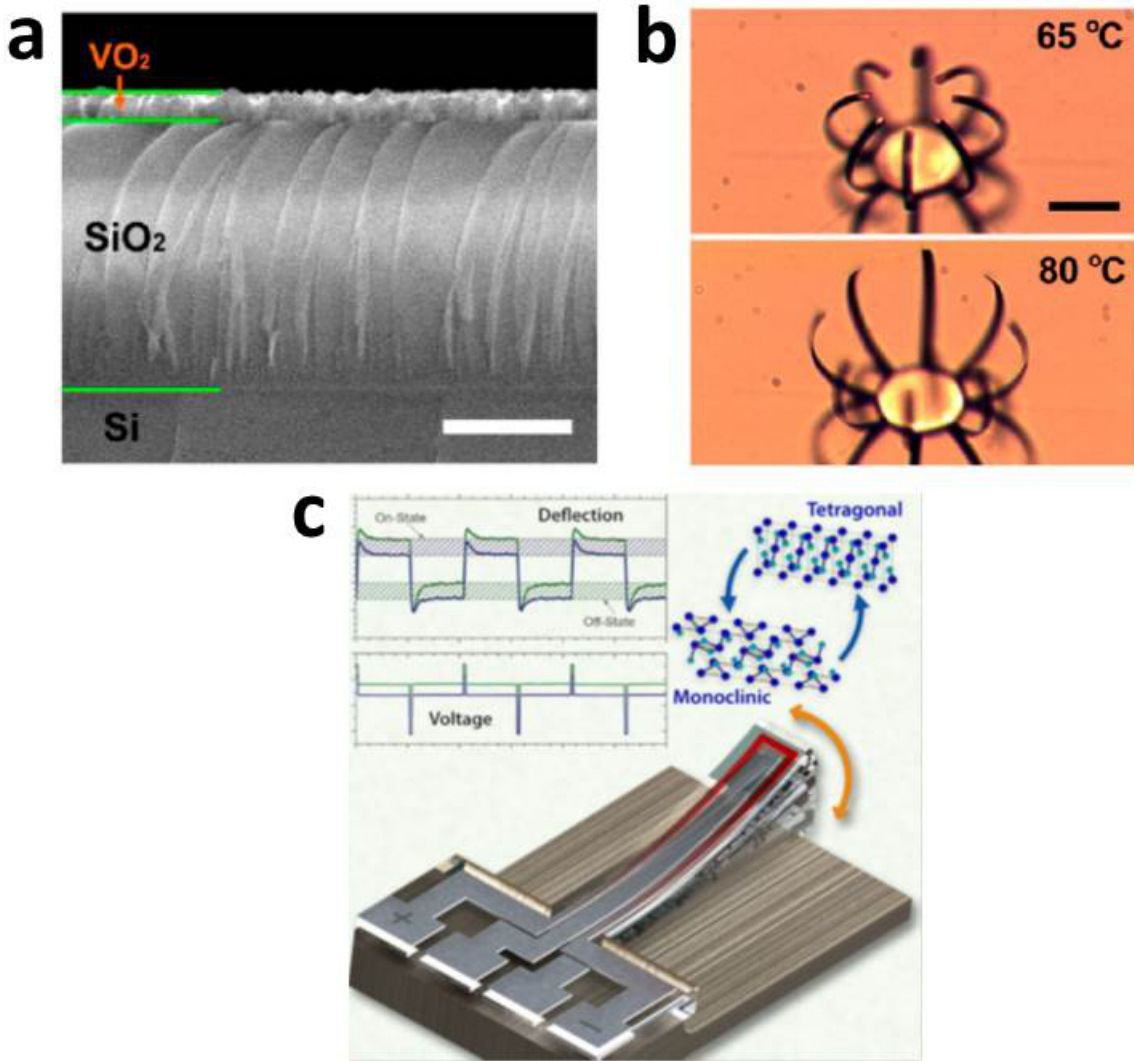


Figure 2.5: Cross section of VO₂ silicon mechanical actuator, a. Thermally activated VO₂ micro mechanical actuator above and below phase transition temperature, b[7]. VO₂ mechanical memory device, c[9].

2.3 Photothermal and CW Optical Modulation of Si-VO₂ Ring Resonators

2.3.1 Introduction

The limitations of all-silicon optical modulators motivate the search for hybrid material combinations that can satisfy device requirements by incorporating a second material on the silicon platform to control modulation[76, 68, 12]. In one recent example, it has been proposed that intensity modulation with speeds up to 1 THz may be feasible with a hybrid polymer-silicon waveguide structure based on the all-optical Kerr effect[77]. Graphene has also recently been integrated with silicon waveguides and used to demonstrate a high-speed electro-absorption based broadband optical modulator[8]. In a similar fashion, VO₂ has been integrated onto silicon waveguides to function as an in-line broadband absorption modulator[12].

At Vanderbilt, we have focused on making and characterizing silicon hybrid optical modulators by incorporating VO₂ as the optical switching element. The performance of these devices is tested by thermally, optically and electrically triggering the phase transition. By placing a small patch of VO₂ on ring resonator (or waveguide) structures, large changes to the resonant wavelength, and thus optical transmission, can be induced by triggering the phase transition. These hybrid Si-VO₂ modulators lay the foundation for a new class of electro-optic or all-optical modulators utilizing VO₂ as an active element on Si.

2.3.2 Contributions

The testing and fabrication of compact devices designed for optical modulation was performed in collaboration with Prof. Sharon Weiss's group at Vanderbilt. The ring resonator based devices[13, 73] provided the groundwork for a new funded National Science Foundation proposal. The full text of this work can be found in papers by Ryckman[13, 73] published in *Optics Express* and Markov[14] in *ACS Photonics*.

2.3.3 Fabrication

The Si-VO₂ hybrid ring resonator structures (and waveguides) discussed in the following sections were fabricated on a silicon-on-insulator (SOI) substrate with a 220 nm p-type, 1422 cm resistivity, Si(100) layer and 1 μm buried oxide layer (SOITEC). Electron-beam lithography (JEOL JBX-9300100 kV) was used to pattern ZEP 520A e-beam resist spun at 6,000 rpm (300 nm thick). After pattern exposure and development in xylene for 30 seconds, followed by an IPA rinse and N₂ drying, anisotropic reactive ion etching (Oxford PlasmaLab 100), using C₄F₈/SF₆/Ar process gases, removed the exposed portion of the 220 nm Si layer.

A second stage of electron-beam lithography (Raith eLine) opened up windows for VO₂ deposition, using ZEP 520A spun at 2,000 rpm (500 nm thick) to better facilitate VO₂ lift-off. Amorphous VO_x was then deposited by physical vapor deposition, as outlined in Chapter 4.2. Deposition and lift-off in acetone under sonication produced amorphous VO_x patches across the silicon rings. Samples were then annealed in a vacuum chamber with 250 mTorr of oxygen at 450 °C for five minutes.

2.3.4 Experimental

A SEM image of the ring resonator devices tested is shown in Figure 2.6. The radius, as measured from the center of the ring to the midpoint of the ring waveguide, is 1.5 μm and the ring width is 500 nm. The bus waveguide is 400 nm wide and the gap between ring and waveguide is 75 nm. A patch of crystalline VO₂, 560 nm long and 70 nm thick is deposited across a small section of the ring.

The experimental setup used to test these devices is shown in Figure 2.7. A 532 nm cw pump laser is used for excitation in all measurements. The peak intensity was calculated to be between 15-30 W/cm².

Transmission measurements for a 1.5 μm radius ring with and without VO₂, Figure

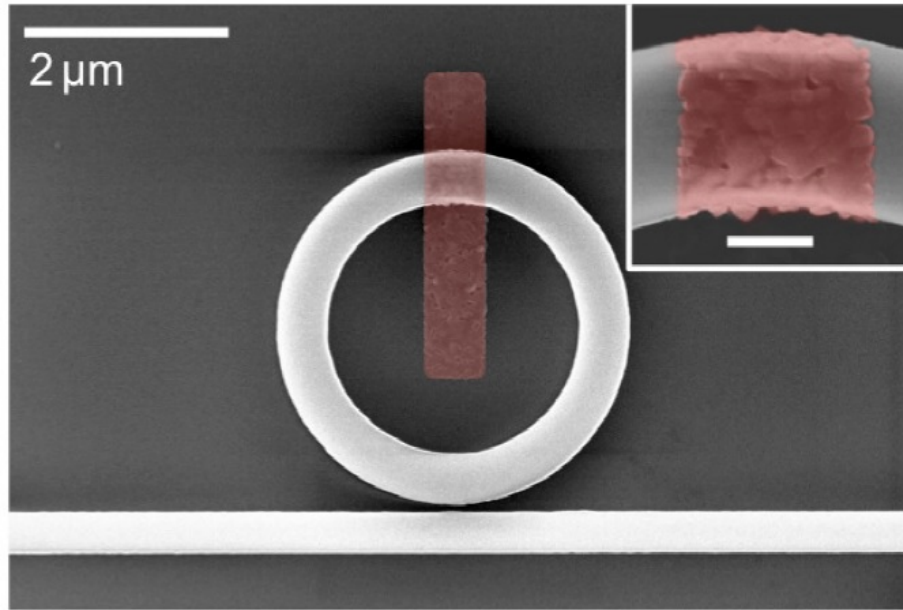


Figure 2.6: SEM image of Si-VO₂ micro-ring resonator with 1.5 μm radius. The VO₂ patch is highlighted in false-color. (scale bar is 250 nm)[13].

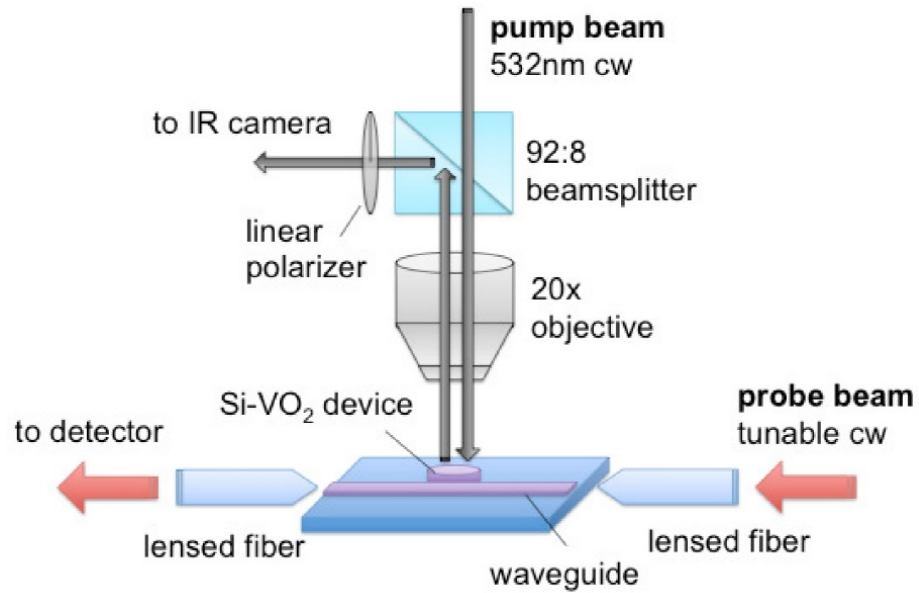


Figure 2.7: Schematic of the optical measurement set-up[13].

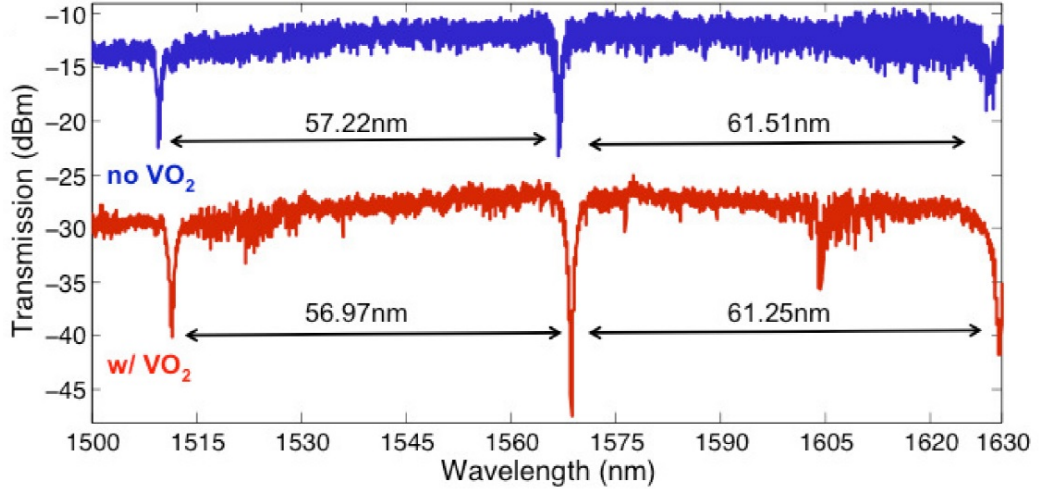


Figure 2.8: Spectral dependence of the optical transmission for 1.5 μm radius ring resonators with (bottom) and without (top) VO_2 patch. The top curve has been shifted by + 20 dBm for clarity[13].

2.8, show the large free-spectral range (FSR) near 60 nm, a desirable feature which could enable multiplexed photonic architectures[78]. The ring with VO_2 has deeper resonances than the one without, possibly indicating that the presence of VO_2 improves the coupling.

2.3.5 Results and Discussion

In Figure 2.9, the optical transmission of the 1.5 μm radius Si- VO_2 ring resonator is shown with the excitation laser on (metallic state) and off (semiconducting state). A significant shift in the resonance wavelength, $\Delta\lambda = 1.26$ nm, is measured in addition to optical modulation greater than 10 dB at the initial resonance wavelength, $\lambda = 1568.78$ nm. The observed shifts in resonant wavelength are consistent with a change in index in the vicinity of the ring. The resonant wavelength (λ_{res}) for a ring resonator is given by:

$$\lambda_{res} = \left(\frac{n_{eff}L}{m} \right) \quad (2.1)$$

where n_{eff} is the effective index of the ring (Equation 2.2), L is the circumference of the ring and m is an integer corresponding to the multiple resonant wavelengths of the ring.

The blue-shift in resonance frequency is consistent with the reduction in refractive index which results from triggering the SMT. Additional optical effects may contribute to this response, including:

1. the thermo-optic (TO) effect in silicon, $\Delta n/\Delta T = + 1.86 \cdot 10^{-4}/K$;
2. the free-carrier index (FCI), $\Delta n \approx -N_c$, where N_c is the number of excited carriers.

These two effects are much weaker than the optical response of VO_2 and also have the opposite sign. In this device, the TO and FCI refractive index contributions from silicon work against each other, making the VO_2 response even more pronounced. In the absence of these effects, the $\Delta\lambda = 1.26$ nm value observed could be even larger.

The temporal response at the resonant wavelength $\lambda = 1568.78$ nm is presented in Figure 2.10. Initially the optical transmission is very low (VO_2 is semiconducting) corresponding to the “on-resonance” state. After excitation, an immediate increase in the optical transmission occurs (~ 10 dBm) followed by a 15 second decay toward low transmission. The transmission gradually increases for about three minutes before stabilizing, Figure 2.10(a). The time scales observed in these measurements are the result of laser-induced heating, with the initial spike to high transmission resulting from the rapid heating of the silicon ring and a thermo-optic dominated shift to longer resonance wavelength. The photothermal switching approach used in this experiment, Figure 2.7), can be optimized to reduce response time by increasing the pump intensity[79].

In Figures 2.10(b) and 2.10(c) the slow thermal recovery is examined. The transmission does not return to the initial state immediately; turning off the laser produces a small (0.5 dB) increase in transmission and 2 second delay before a 2-5 dB drop. After completing the phase transition, several minutes are needed for the device to return to room temperature. This time scale is not inherent to the phase transition but is an artifact of the thermal

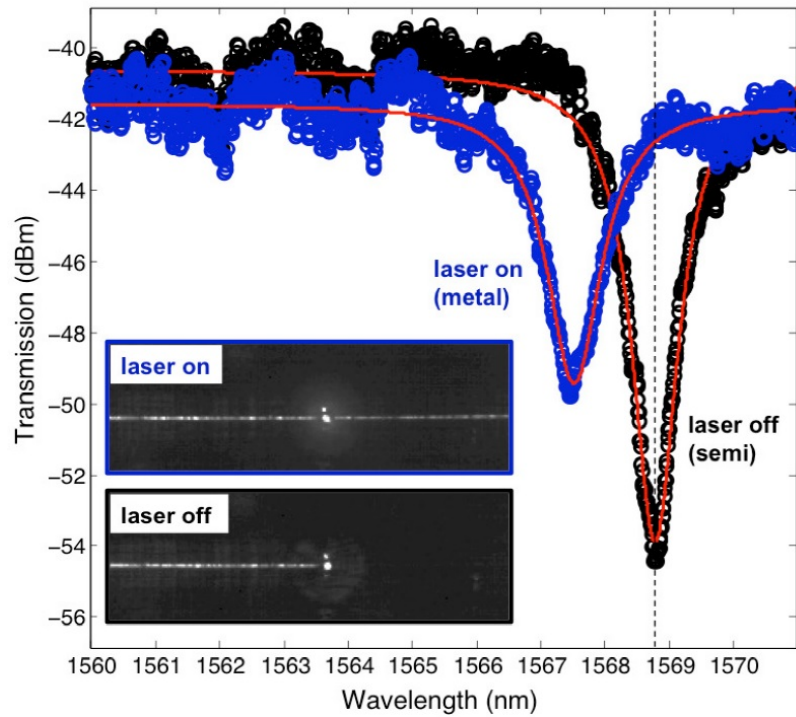


Figure 2.9: Optical transmission of the $1.5 \mu\text{m}$ radius hybrid Si-VO₂ ring resonator as a function of wavelength, before and after triggering the SMT with a 532 nm pump laser. The lines are Lorentzian fits. Inset: IR camera images revealing vertical radiation at a fixed probe wavelength, $\lambda = 1568.78 \text{ nm}$ (dashed line)[13].

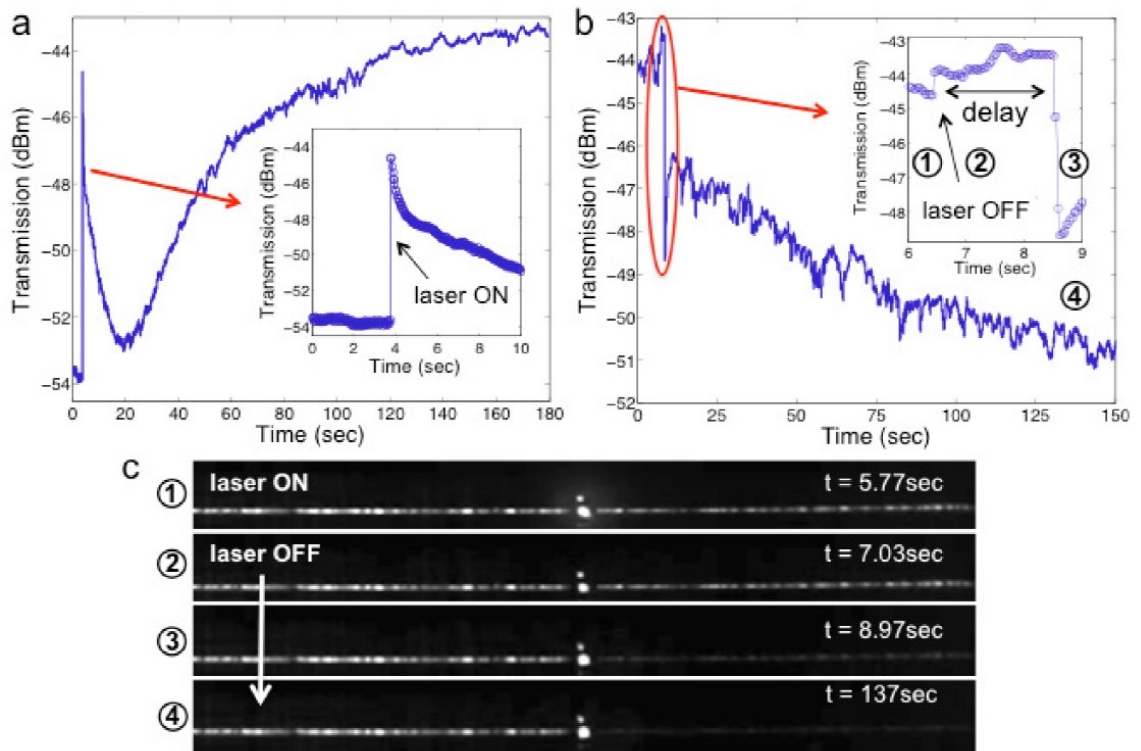


Figure 2.10: Temporal behavior of the optical transmission at $\lambda = 1568.78$ nm, in a $1.5 \mu\text{m}$ radius Si-VO₂ device. With 532 nm pump laser (a) ON and (b) OFF. (c) Images from the IR camera, at various times, highlighting the probe response observed in (b)[13].

dissipation behavior of this device. A design which is optimized to increase the thermal conductivity could significantly decrease the return time.

The influence of the ring-resonator radius is explored by fabricating different size rings, the results are presented in Figure 2.11. In 2.11a, the resonance shift ($\Delta\lambda$) is normalized to the initial resonance position and shows a decrease in the blue-shift for increasing radius. The primary effects contributing to the resonance shift are the SMT in the VO₂, and the TO and FCI effects in silicon. Their contributions to the effective index change, N_{eff} of resonator are approximated by

$$\Delta N_{eff} = \Delta N_{SMT} \left(\frac{L_{VO_2}}{2\pi R} \right) + \Gamma_{Si} (\Delta n_{TO} + \Delta n_{FCI}) \quad (2.2)$$

where ΔN_{SMT} represents the change in index of the VO₂, with length L_{VO_2} , R is the radius, Γ_{Si} the field confinement factor[80], and Δn_{TO} and Δn_{FCI} are the index changes due to the TO and FCI effects in silicon.

Reducing the coverage of VO₂ on the ring diminishes the effect of the SMT on the overall effective index change, reducing the wavelength shift ($\Delta\lambda / \lambda$) as observed in Figure 2.11(a). The 2, 5 and 10 μm rings correspond to a fractional coverage (L_{VO_2} / L_{RING}) of 4 %, 2 % and 1%, respectively. The sign change in the resonant response (from blue to red) for the largest ring occurs when the silicon TO affect is the main source of index variation. The resonance shift is varied by changing the fractional VO₂ coverage on the resonator and possibly by the volume. Further variation of the resonant response might be achieved using alternate geometries[80]; simultaneously maximizing ΔN_{SMT} and minimizing Γ_{Si} .

Figure 2.11(b) presents the quality factors (Q, Equation 2.3) of different size resonators, before and after photothermally triggering the SMT, as determined by fitting the resonances to a Lorentzian line shape,

$$Q = f_0 / \Gamma \quad (2.3)$$

where f_0 is the resonant frequency and Γ is the full width at half-maximum. In both the

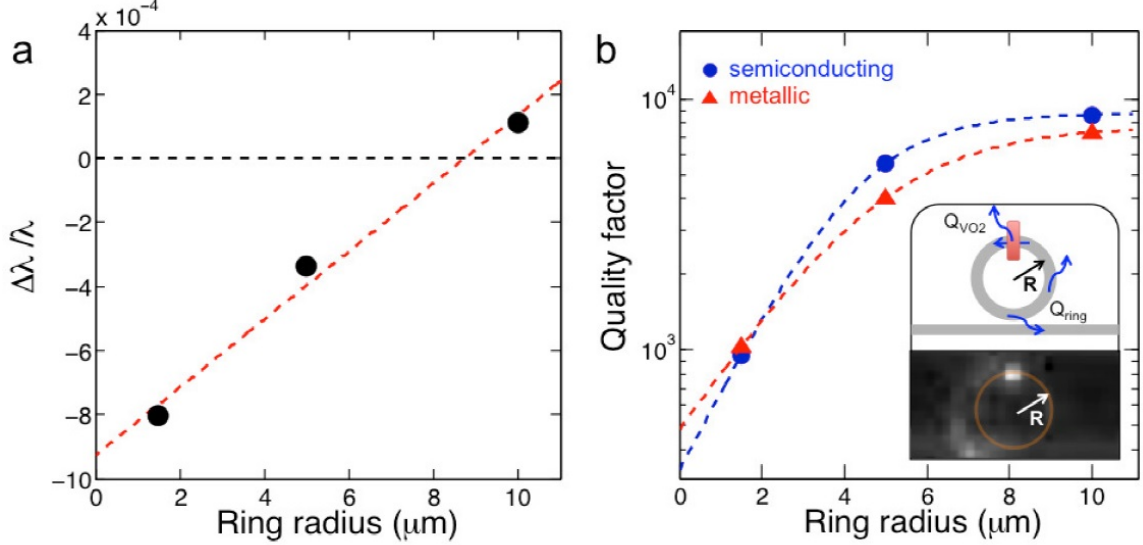


Figure 2.11: (a) Normalized resonance shift after photothermally triggering the SMT for hybrid Si-VO₂ micro-ring resonators of different radii and the same VO₂ patch length $L_{VO_2} = 560$ nm. (b) Q-factor for the same devices before and after triggering the SMT. Inset illustrates the various decay channels affecting total Q-factor and an IR camera image showing vertical radiation from a $10 \mu\text{m}$ radius hybrid resonator when on-resonance in the semiconducting state[13].

semiconducting and metallic states, a trend of increasing Q-factor with increasing ring radius is observed. The exponential increase is expected for rings less than $5 \mu\text{m}$ in diameter, due to an exponential reduction in the bending losses[81]. The increase appears to saturate for larger rings. This is explained by examining contributions to the Q-factor:

$$\frac{1}{Q_{tot}} = \frac{1}{Q_{coup}} + \frac{1}{Q_{prop}} \quad (2.4)$$

Sources of propagation loss come from the Si ring and the VO₂ patch[12], given by:

$$\frac{1}{Q_{prop}} = \frac{1}{Q_{ring}} + \frac{1}{Q_{VO_2}} \quad (2.5)$$

The dashed trend lines shown in Fig. 2.11(b) are produced by combining Equations (2.4) and (2.5) and assuming that the ring quality factor depends exponentially on the ring radius. This matches the experimental data, as we observe a decrease of Q_{VO_2} from 8,800

to 7,800. For smaller rings the Q-factor is limited by bending loss and for larger rings the Q-factor is limited by loss from the VO₂ patch. Infrared imaging of the 10 μm ring resonator (inset Fig. 2.11(b)) confirms that vertical radiation losses are mainly coming from the VO₂ patch. These results show that 6% VO₂ on a silicon ring is enough to produce a large resonant response with little effect on the total Q-factor of the 1.5 μm radius device. The resulting Q-factor (103) indicates a very short cavity lifetime (1 ps), making ultrafast modulation possible.

2.4 Pulsed Optical Modulation of Si-VO₂ Ring Resonators

In this section we examine the temporal behavior for Si-VO₂ ring resonator devices using nanosecond pulses to trigger the phase transition. Compared to our previous work using cw and thermal excitation, the all-optical switching demonstrated below eliminates the thermo-optic effects observed previously. Optical control of absorption or phase in non-resonant and resonant structures, is a necessary capability for optical modulators. Our hybrid devices demonstrate state-of-the-art values for optically induced absorption modulation (4 dB μm⁻¹) and intracavity phase modulation (π/5 rad μm⁻¹). In terms of compatibility, the processes used to produce these devices are consistent with current silicon-based fabrication technology.

2.4.1 Experimental

Figures 2.12(a) and 2.12(b) illustrate the devices used. These devices are fabricated by the same process described in the previous section. The experimental setup used to test the devices is presented in 2.12(c). A near-infrared (NIR) nanosecond laser is used to pump the device at 1064 nm (25 ns FWHM) while transmission of a tunable probe laser (1500-1600 nm) is monitored. The pump fluence is varied from (0.5-8 mJ cm⁻²).

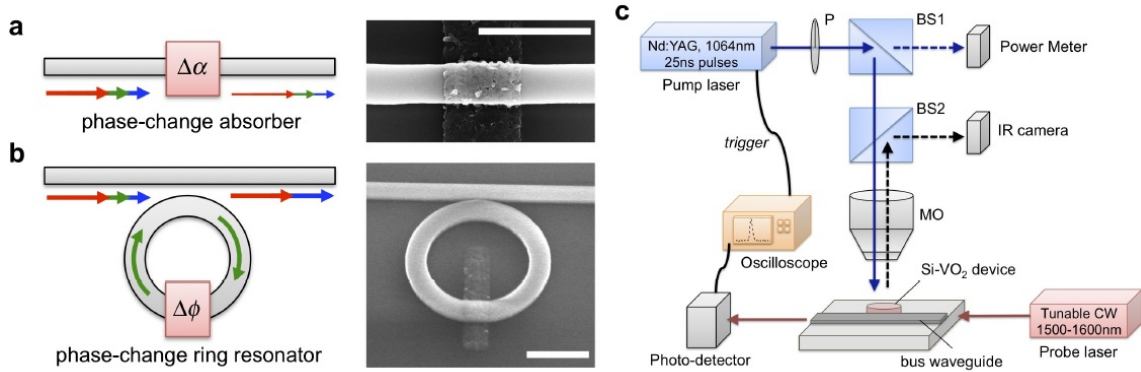


Figure 2.12: Si-VO₂ photonic devices and all-optical modulation. (a) Phase-change absorber where the SMT induces a broadband change in absorption Δ . SEM image of a compact Si-VO₂ absorber with a 1 μm VO₂ patch. (b) Phase-change ring resonator where the SMT induces phase modulation $\Delta\phi$. SEM image of compact Si-VO₂ ring resonator with radius $R = 1.5 \mu\text{m}$ and a 500 nm VO₂ patch. SEM scale bars are 1.5 μm . (c) Schematic of the experimental pump-probe set-up. Transmission is monitored with a photo-detector and oscilloscope. Nanosecond-pulsed pump light is focused onto the device with a microscope objective (MO) and the power is controlled by a linear polarizer (P)[73].

2.4.2 Results and Discussion

Figure 2.13(a) presents the time-dependent transmission for a waveguide with VO₂ in-line absorber and varying pump fluences (0.5-8 mJ cm^{-2}). Devices with two different VO₂ patch lengths are used, 1 μm and 0.5 μm . Regardless of the VO₂ patch length or excitation fluence, a sharp reduction in the optical transmission is observed after optical pumping and occurs on a time-scale comparable to the pulse FWHM. The modulation depth is observed to change (approximately linearly) with the pump fluence. In comparison to other modulators, the modulation depth is approximately 40 times that of monolayer graphene-on-Si absorbers (0.1 $\text{dB } \mu\text{m}^{-1}$) [82] and one thousand times larger than silicon based two-photon cross-absorption modulation (0.001 $\text{dB } \mu\text{m}^{-1}$)[83]. Broadband operation was verified, from 1500-1600 nm, as shown in Fig. 2.13(c).

Figure 2.14(a) illustrates the transmission for a ring-resonator device with $R = 1.5 \mu\text{m}$ and an integrated VO₂ patch 500 nm long by 70 nm thick. Due to bending losses, this device has a modest Q of ≈ 103 . Time-dependent transmission as a function of fluence is shown

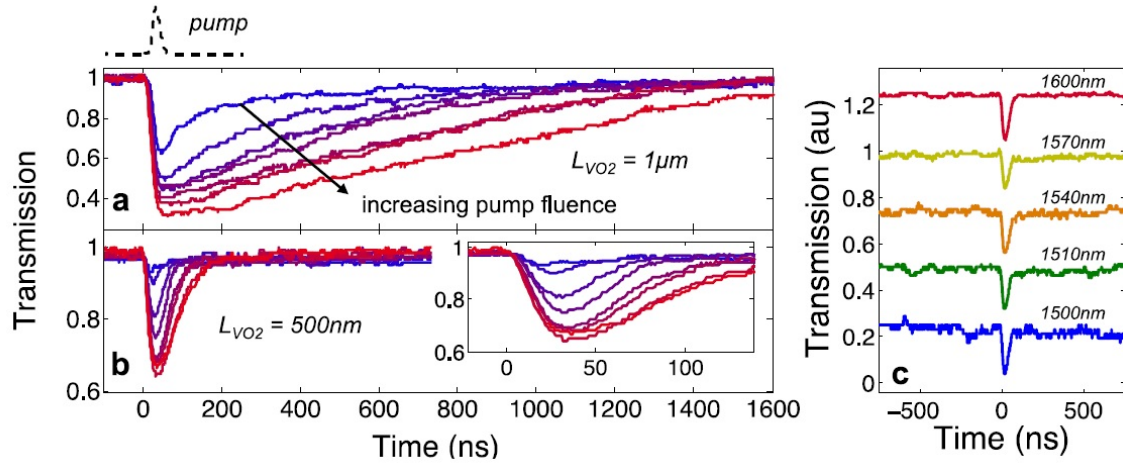


Figure 2.13: Normalized probe transmission through Si-VO₂ absorbers with (a) 1 μm and (b) 500 nm VO₂ patch lengths. The pump fluence is varied from 0.5-8 mJ cm⁻². Inset shows a magnified view of the temporal response. (c) Transmission through a 500 nm Si-VO₂ absorber from 1500 to 1600 nm, demonstrating that the SMT of VO₂ can produce broadband absorption modulation. Plots are shifted for clarity[73].

in Fig. 2.14(b), where probe wavelength is on resonance ($\lambda = 1588.5$ nm). Photoinducing the SMT generates an abrupt increase in transmission, (~ 7.2 dB), followed by slower relaxation to the initial value. The increased transmission observed for this modest Q-factor indicates that the resonance wavelength is significantly modified by the photoinduced SMT. In contrast, Si-only devices, using relatively weak electro-optic or nonlinear effects require high Q-factor, narrow band (less than 5 GHz) resonators for significant modulation[81].

As shown in Figure 2.14(b), the reverse transition is significantly slower than the SMT. Reversing the SPT is a thermal dissipation problem dependent on the device design and nucleation of the monoclinic phase[47, 84]. All-optical switching does not generate significant localized heating in the ring. This conclusion is justified by comparing the transmission in a ring with VO₂ to one without and discussed below (Figure 2.16). By holding the fluence below the critical level of 8-10 mJ/cm², significant improvements in relaxation time can be achieved by triggering the SMT without driving the SPT to completion[38, 39]. The behavior of VO₂ in the "monoclinic metallic state" state is explored more in Chapter 5.2.

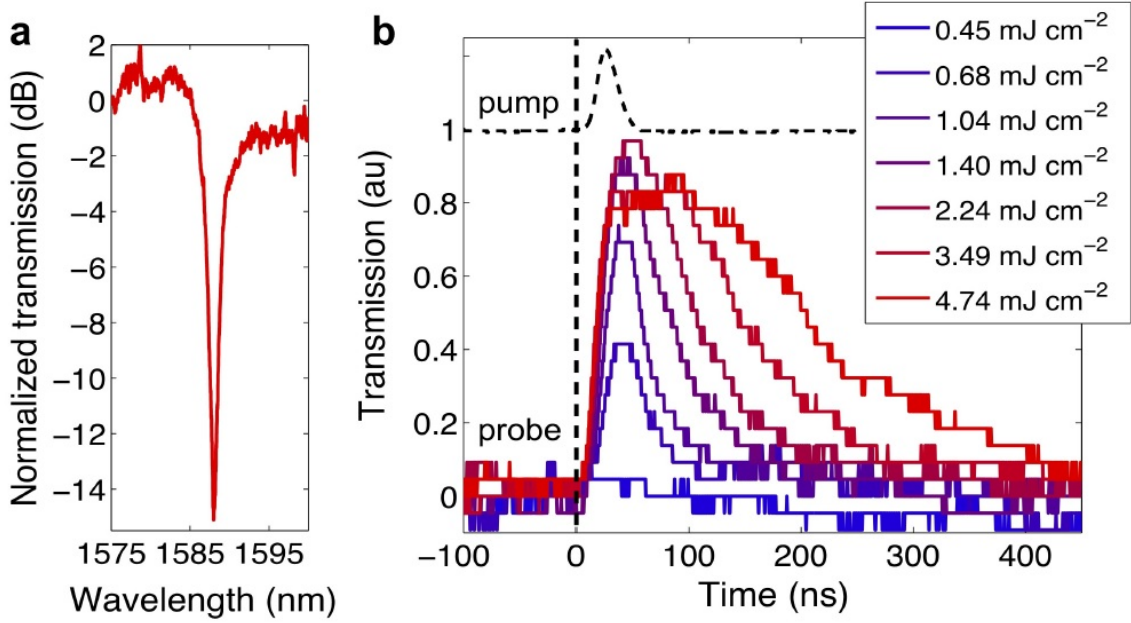


Figure 2.14: (a) Transmission spectra for a Si-VO₂ ring resonator with radius $R = 1.5 \mu\text{m}$. (b) Probe transmission at resonant wavelength ($\lambda = 1588.5 \text{ nm}$)[73].

Changing the VO₂ patch length to sub-micron dimensions (from $1 \mu\text{m}$ to 500 nm) reduces the decay time τ_{M-S} by one order of magnitude [Fig. 2.15(b)]. This faster relaxation time for shorter patches may result from the quasi-one-dimensional geometry of the waveguide. The Si-VO₂ hybrid ring resonators using short (500 nm patches) show similarly reduced relaxation times varying moderately with fluence, Figure 2.15(b). This suggests that the thermal properties of the interface play a significant role in the dynamics of the reverse transition and can be optimized.

Time-dependent measurements at varying probe wavelengths exhibit the spectral behavior of the resonator response to the phase transition. Figure 2.17(a) shows the performance of a device with a 500 nm VO₂ patch when pumped at 1.9 mJ/cm^2 , above the required fluence to complete the SMT. The optically triggered phase transition produces rapid modulation at the resonant wavelength estimated to be $\Delta\lambda_{SMT} = -3.07 \text{ nm}$ (Figure 2.17(a)), extracted by fitting the data to a Lorentzian line shape. The same experiment on a resonator without VO₂, resulted in a wavelength shift of $\Delta\lambda_{Si} = -0.057 \text{ nm}$, nearly sixty

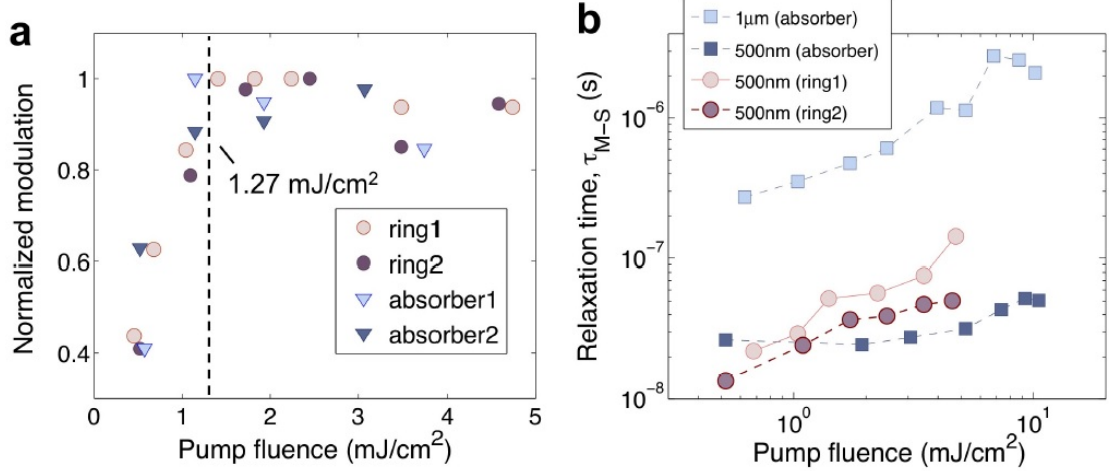


Figure 2.15: (a) Saturation of the probe signal is observed above the threshold fluence of 1.27 mJ cm². (b) Relaxation time, τ_{M-S} , from the metallic state to the initial semiconducting state for different pump fluences, plotted for Si-VO₂ absorbers and ring resonators with 500 nm or 1 μ m VO₂ patches[73].

times smaller (Figure 2.16). The large $\Delta\lambda_{SMT}$ change in resonant wavelength when VO₂ is incorporated arises from substantial modification of the VO₂ refractive index, $\Delta\text{Re}(n_{VO_2}) = -1.06$, the small $\Delta\lambda_{Si}$ is due to the weak silicon FCI, estimated to change by $\Delta\text{Re}(n_{Si}) = -1.6 \times 10^{-4}$.

In Figure 2.17(a), the SMT-induced resonance shift is completed in 25-30 ns, limited by the pulse FWHM. The reverse transition back to the semiconducting state occurs in 50-70 ns. This large $\Delta\lambda_{SMT} = -3.07$ nm shift requires only 0.275 μm^2 active area for 70 nm thick VO₂ patch, approximately 5.3% surface coverage of the ring.

A Si-VO₂ waveguide, with Si dimensions 220 x 500 nm and a 70 nm thick VO₂ layer, is expected to have a large change in effective index $\Delta N_{SMT} = -0.14$, as confirmed with FDTD calculations, Figure 2.17(b). To confirm that this effect is dominant and tunable, devices are fabricated with the same VO₂ patch area and with ring radii ranging from 1.5 to 10 μ m. $\Delta\lambda_{max}$ for each ring radius R was then measured using variable wavelength pump-probe measurements. In Fig. 2.17(c), the magnitude of the resonant wavelength shift is presented, $|\Delta\lambda_{max}|$, and follows a R^{-1} dependence, in agreement with calculations where

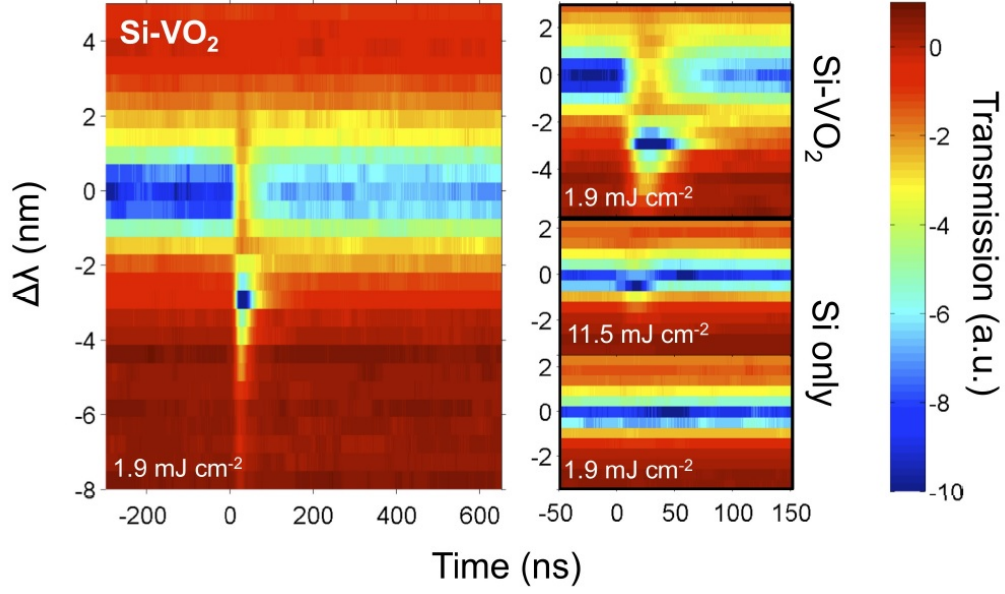


Figure 2.16: Spectral response of Si-VO₂ ring resonator. Optical transmission for variable wavelength pump-probe measurements above threshold (1.9 mJ/cm²). Right column shows magnified view of the same device along with a Si-only device pumped at 1.9 mJ/cm² and 11.5 mJ/cm². Color bar indicates a logarithmic scale[73].

the average effective index change is modeled as $\Delta N_{eff} = \Delta N_{SMT} L_{VO_2} (2\pi R)^{-1}$.

The broad resonant response of these devices allows them to operate in the presence of thermal fluctuations which are typically a problem for narrow resonance devices. The lack of temperature sensitivity is further demonstrated by the shaded region in Figure 2.17(c). This region represents the area where $\Delta\lambda \leq 0.3$ nm, corresponding to ± 3 °C temperature variation in silicon. All silicon devices which operate in this area are highly sensitive to thermal fluctuations and require active thermal compensation schemes. The longer cavity lifetimes for high-Q silicon resonators also limit the speed of operation. For these devices, the loss due to VO₂ results in a modest Q-factor which is more suitable for high speed operation. In addition, the Si-VO₂ platform provides a large response for a given device size, favoring compact device designs.

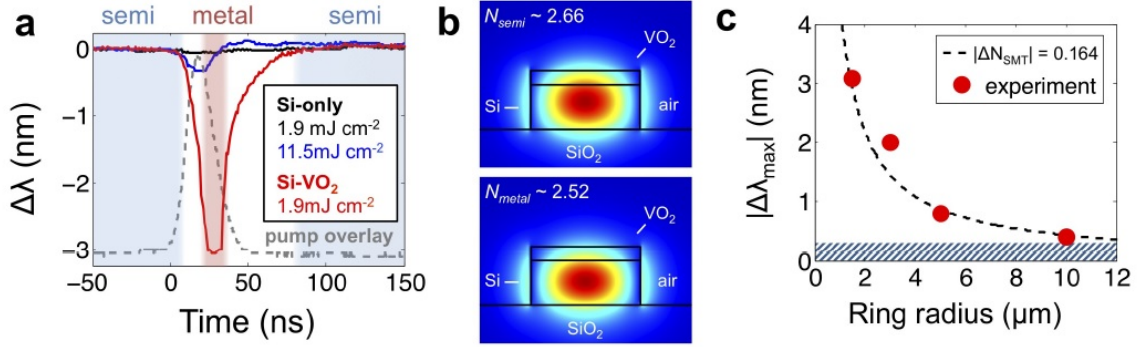


Figure 2.17: Analysis of Si-VO₂ ring resonator. (a) Resonant wavelength vs. time, extracted from pump-probe measurements shown in Fig. 2.16. (b) FDTD simulation for a hybrid Si-VO₂ waveguide, with Si dimensions 220 x 500 nm and a 70 nm thick VO₂ patch on top. (c) Resonance wavelength blue-shift $\Delta\lambda_{max}$, in response to the photoinduced SMT in Si-VO₂ ring resonators with varying radii and fixed VO₂ patch length. Shaded area represents $\Delta\lambda < 0.3$ nm, corresponding to thermo-optic changes of resonators due to temperature variations[73].

2.5 Conclusions: VO₂ Optical Devices

Compact ring resonator devices with large FSR are produced using relatively small patches of VO₂. A shift in resonant wavelength up to -3.0 nm is recorded for the smallest rings with a temporal response limited by the pump pulse duration (25 ns). VO₂ based modulators have very low sensitivity to thermal fluctuations in contrast to all silicon resonators with very narrow resonance wavelengths. The resonant wavelength shift and Q-factor for these devices can be easily tuned by varying the ring radius. Our devices have modest Q-factors and large modulation depths, making them ideal for compact high speed optical switching.

In Table 2.1 the performance metrics of our vanadium dioxide based ring resonator design (bottom row) are present along with those of competing devices. The large change in VO₂ optical properties allows a device footprint five times smaller than any other design. Our demonstrated bit rate (< 1 Gbit s⁻¹) is limited only by the laser pulse duration, not the fundamental physics of the phase transition, which can support Tbit s⁻¹ speeds. Further reduction in the energy per bit can be achieved by triggering the phase transition with optical

excitation closer to the band gap. The optical modulation depth is comparable to other designs; however, the working spectrum is much larger than other designs making our devices much more suitable for broad band operation. In summary, there is no fundamental reason why VO₂ based optical modulators could not provide “state of the art ” performance.

Table 2.1: Current optical modulator performance metrics as compiled by Reed[58].

Modulation principle	Structure	Device footprint	Speed achieved	Energy per bit (fJ bit^{-1})	Modulation voltage	d.c. modulation depth and insertion loss	Modulation depth / speed	Working spectrum
Depletion of a horizontal p-n junction[85]	MZI	$10^4 \mu\text{m}^2$	30 Gbit s^{-1}	3×10^4	6.5 V	>20 dB, 7 dB	1 dB/30 Gbit s^{-1}	20 nm
Forward-biased diode[86]	MZI	$10^3 \mu\text{m}^2$	10 Gbit s^{-1}	5×10^3	7.6 V	6-10 dB, 12 dB	-	-
Forward-biased diode[81]	Ring	$10^2 \mu\text{m}^2$	12.5 Gbit s^{-1}	300	3.5 V	>10 dB, 0.5 dB	3 dB/18 Gbit s^{-1}	0.1 nm
Reverse-biased p-n junction[87]	Disk	$20 \mu\text{m}^2$	10 Gbit s^{-1}	85	3.5 V	8 dB, 1.5 dB	-	0.1 nm
Forward-biased p-i-n diode[88]	Ring	$10^2 \mu\text{m}^2$	3 Gbit s^{-1}	86	0.5 V	7 dB, 1 dB	-	0.2 nm
Reverse-biased p-n junction[59]	Ring	$10^3 \mu\text{m}^2$	10 Gbit s^{-1}	50	2 V	6.5 dB, 2 dB	8 dB/10 Gbit s^{-1}	0.1 nm
Vanadium dioxide phase transition[73]	Ring	$4 \mu\text{m}^2$	$<1 \text{ Gbit s}^{-1}$	300	N/A	10 dB, 2 dB	7 dB/<1 Gbit s^{-1}	60 nm

Chapter 3

Er Doped VO₂

3.1 Introduction

The optical transitions in Er³⁺ ions, which occur at ~ 1550 nm, have made it a very popular material for optical amplification and switching in fiber optics. Erbium atoms alone do not luminesce in this spectral region and must be ionized to the Er³⁺ state. We produce a different form of optical modulator in this Chapter by incorporating optically active erbium into the VO₂ crystal structure. We show that the required erbium ionization state can be achieved in the VO₂ lattice without destroying the phase transition properties.

3.2 Er-Doped VO₂

Erbium is the 11th element in the lanthanide series and is of great technological importance to the optical fiber communications industry due to a first excited state to ground state transition at $\lambda = 1.54 \mu\text{m}$, the spectral region where optical fibers have their minimum loss. This transition may be pumped optically with 1 or 1.45 μm light, and produces maximum gain in the wavelength region between 1530-1560 nm[89]. Since the pump and lasing wavelengths are both compatible with optical fibers, erbium fiber lasers have become quite popular due to their compact size and simplicity, which eliminates many of the alignment issues encountered in other types of lasers. As a result, erbium doped fiber amplifiers have become a critical part of modern long-range optical communication and are expanding into other applications.

Being able to modulate optical emission at telecommunication wavelengths has driven interest in incorporating erbium with VO₂. In one example, Cuff and collaborators[90] designed a multi-layer device which uses the VO₂ phase transition to switch between magnetic dipole (MD) and electric dipole (ED) dominated emission from a erbium emitter

layer. By careful choice of material and layer thickness they engineer the local density of states (LDOS) to favor MD emission when VO₂ is in the insulating state and ED emission when in the metallic state. In the following sections a different scheme is explored, where erbium is incorporated into the VO₂ crystal structure and the phase transition is used to modulate the electronic environment directly around the optically active Er³⁺ ions.

3.2.1 Contributions

We explored the possibility of modulating the optical transitions in erbium using the VO₂ phase transition. These experiments were performed in collaboration with Prof. Jeffrey McCallum at the University of Melbourne; the full text can be found in *Applied Physics Letters*[91] and *COMMAD*[92].

3.3 Erbium Doped Films: Crystal Symmetry

ErO₆ clusters (as found in SiO₂) have stable ionic bonds and an electronic structure that supports the Er intra-4f transitions, including the one responsible for luminescence at 1.53 μm [93]. The monoclinic and rutile phases of VO₂ have a structure into which the ErO₆ clusters can fit. In Figure 3.1 the M1 and R structures are shown along with the oxygen octahedra surrounding each vanadium atom, shown in blue. ErO₆ can replace any of these octahedra, allowing optically active erbium to be incorporated in the VO₂ lattice without significant distortion.

3.3.1 Erbium Doped Films: Experimental

VO₂ thin films 100 nm thick were deposited and annealed in the same manner described in section 4.2. Er was then implanted into half of the samples by a NEC low energy ion implanter at 100 keV, with fluences ranging from 2x10¹³ cm⁻² to 1x10¹⁵ cm⁻². From simulations[94], the penetration depth of the Er ions is calculated to be 2.71 nm, with a

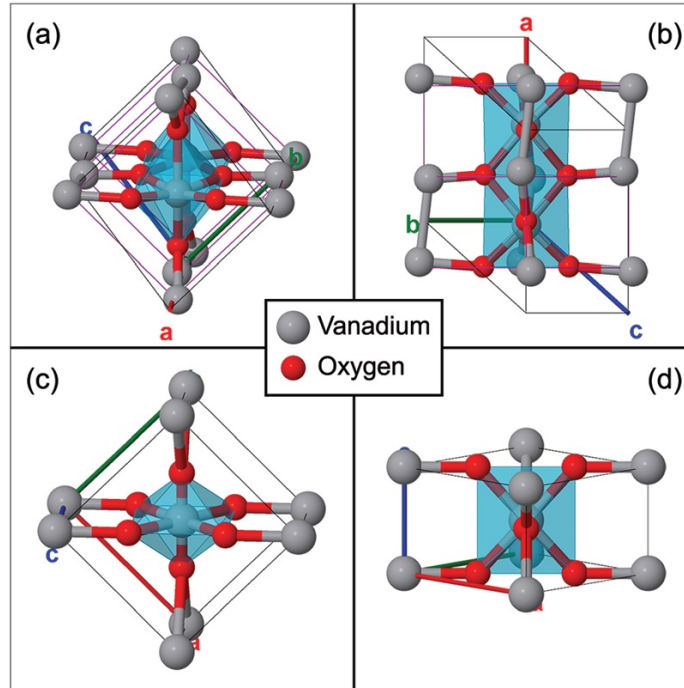


Figure 3.1: The monoclinic M1 ((a) and (b)) and rutile R ((c) and (d)) structures of VO₂ viewed along different directions. The translucent blue region indicates where the ErO₆ clusters fit[91].

standard deviation $\sigma = 7.2$ nm, the Er concentration averages to 1.00 atomic %. Implanted and the unimplanted samples were annealed separately for one hour in N₂, at temperatures from 400 °C to 1000 °C. Samples labeled as-prepared refer to the sample after annealing in oxygen but before Er implantation and anneal refers to the sample after Er implantation and annealing.

Raman spectroscopy was performed to examine the crystallinity of the VO₂ and understand how the Er was incorporated. Photoluminescence measurements confirmed the electronic structure around the erbium atoms. Measurement of the phase transition properties was accomplished by temperature resolved reflectivity measurements with a 1152 nm HeNe laser. A reference sample was used to calibrate the reflectivity and the effects of roughness on scattering were accounted for.

3.3.2 Erbium Doped Films: Results and Discussion

3.3.3 Raman Scattering

Figure 3.2 presents Raman spectra using 532 nm excitation, for a as-prepared VO₂ sample and another sample implanted with Er and annealed at 1000 °C. The room temperature and liquid N₂ temperature measurements both have Raman lines that agree well with spectra previously reported for VO₂[95]. The similarity at room temperature, between the sample with Er and the one without confirms that Er fits into the VO₂ lattice without distorting the structure. At liquid N₂ temperatures, additional peaks are observed and by switching the excitation wavelength, we confirm that they are photoluminescence (PL) peaks. The additional peaks correspond to Er³⁺ PL and the electronic transitions: ²H_{9/2} → ⁴I_{13/2} and ⁴S_{3/2} → ⁴I_{15/2}. The Raman intensity decreases after Er implantation, indicating a decline in the VO₂ crystallinity, however much of the intensity loss is recovered after annealing.

3.3.4 Photoluminescence

The PL spectra at -195.6 °C for a VO₂ sample implanted with Er and annealed is shown in Figure 3.3 b-g. All of the Er³⁺ electronic transitions are observed. The corresponding Er³⁺ electronic transitions are color coded in Figures 3.3 b-g and correspond to transitions in the energy level diagram in, 3.3a. PL around 1.53 μm (≈ 0.81 eV) is shown in Figures 3.3b. Two spectra were acquired in the monoclinic phase at -195.6 °C and 22.0 °C and one in the rutile at 100.0 °C. There is some decrease in the overall intensity when comparing the PL from the monoclinic and rutile phases, however the structure is quite similar, indicating that the symmetry around the erbium atoms is not changing dramatically.

Figure 3.4 compares the total intensity of the Er³⁺ PL at 1.53 μm for different Er concentrations and annealing temperatures. Er³⁺ PL was only observed for samples annealed at 800 °C or above, marking 800 °C as the critical temperature for activating the Er³⁺ in

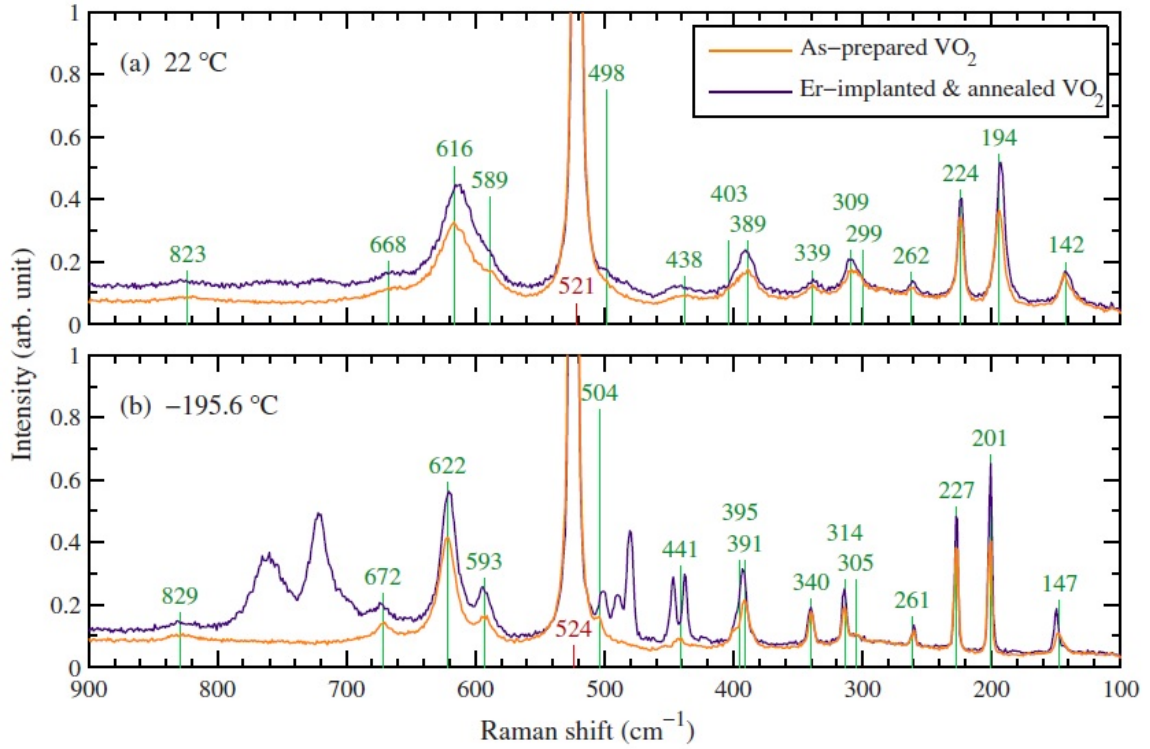


Figure 3.2: The Raman spectra of an as-prepared VO₂ sample and another VO₂ sample implanted with Er and annealed at 1000 °C. These spectra were recorded at (a) room temperature (22 °C) and (b) liquid N₂ temperature (-195.6 °C). The green annotations show the VO₂ Raman lines observed from the as-prepared sample and the red annotation shows the Si Raman, from the substrate. The unlabeled peaks in (b), are Er³⁺ PL from the: ${}^2H_{9/2} \rightarrow {}^4I_{13/2}$ and ${}^4S_{3/2} \rightarrow {}^4I_{15/2}$ transitions[91].

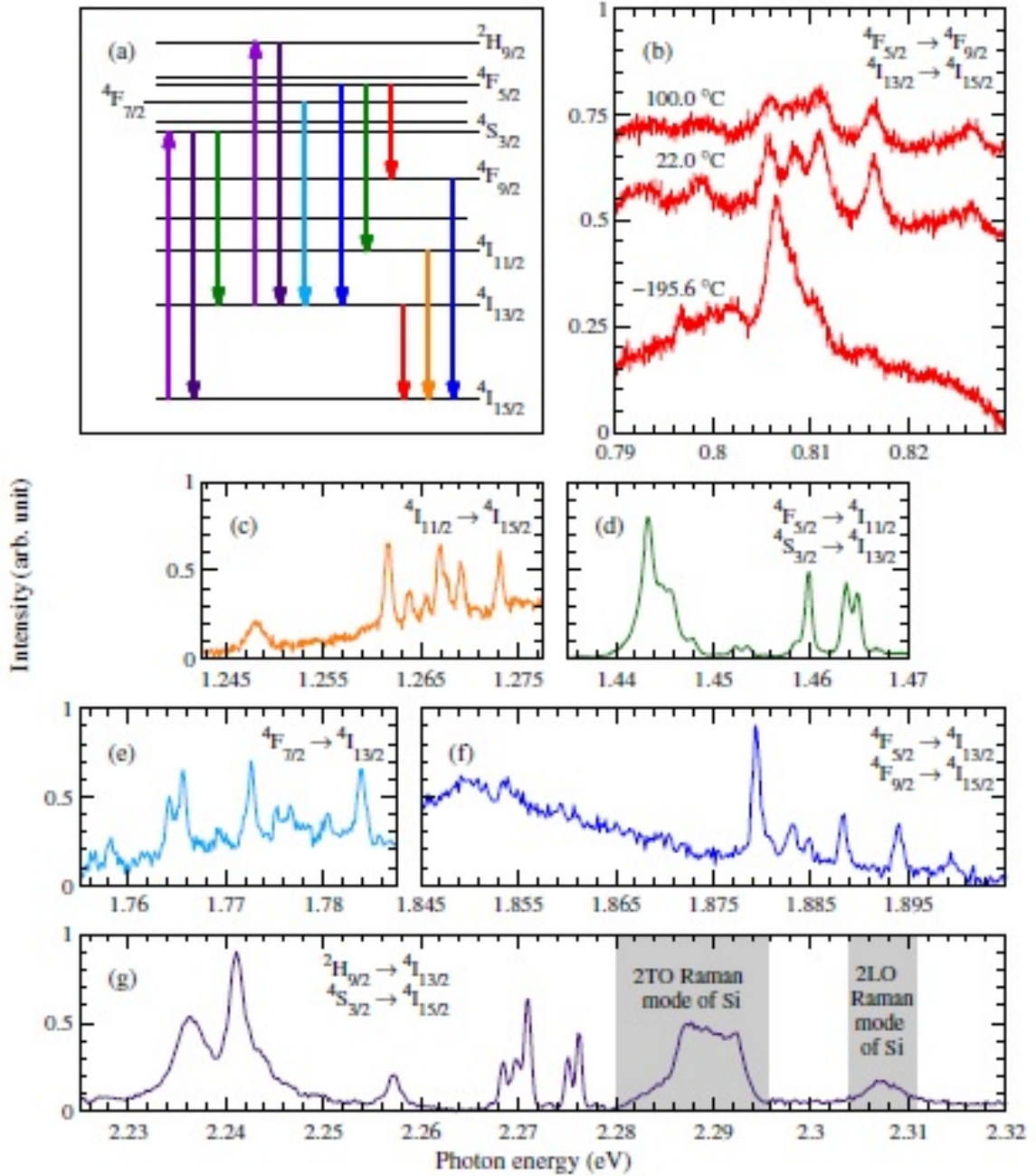


Figure 3.3: (a) Free-ion energy level diagram of Er³⁺, showing the transitions observed in the PL measurements. (b)-(g) PL spectra for a VO₂ sample with Er. Each spectrum corresponds to an electronic transition in (a) with the correspondingly color. The spectra in (b) were measured at three different temperatures (-195.6 °C, 22 °C, and 100 °C) as indicated; all other spectra in (c)-(f) were taken at near-liquid N₂ temperature (-195.6 °C). The peaks indicated by the shaded region in (g) are not due to the Er³⁺ PL, but to the 2TO and the 2LO Raman modes of the Si substrate[91].

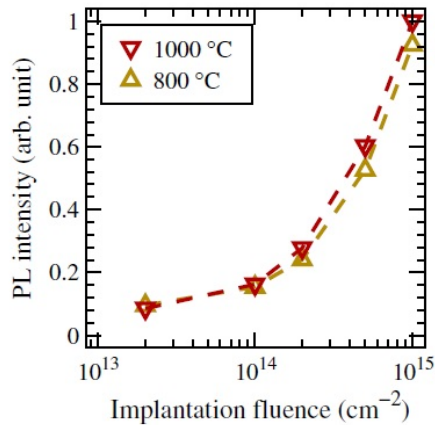


Figure 3.4: Total intensity of the Er^{3+} PL at 0.80580.8166 eV vs. the Er implantation fluence for two annealing temperatures. All data are obtained from measurements at room temperature using 532 nm excitation[91].

VO_2 . No significant difference is observed in the Er^{3+} PL intensity for samples annealed at 800 °C and those annealed at 1000 °C.

3.3.5 Reflectivity Switching

Figure 3.5a and b show the thermally induced change in reflectivity for a pure VO_2 sample annealed at 1000 °C and another VO_2 sample annealed with Er. These measurements show that erbium implantation does not destroy the hysteresis behavior. In thin films, the transition occurs in a percolative nature, with individual grains switching at a specific temperature. Typically a distribution of switching temperatures exist for the grains in a thin film. The shape of a particular hysteresis curve can be modeled as the sum of multiple Gaussian functions which represent the energetic distribution of the grains. In 3.5c and e, the distributions are shown for a pure film and in 3.5 d and f they are presented for the Er doped film. For pure VO_2 , single Gaussian functions are sufficient; however, multiple Gaussian functions are required for the Er doped film. For the heating side (3.5d) only one is needed, but on the cooling side 3.5f two are required. The broad distribution with low amplitude may be indicative of the defects resulting from ion implantation.

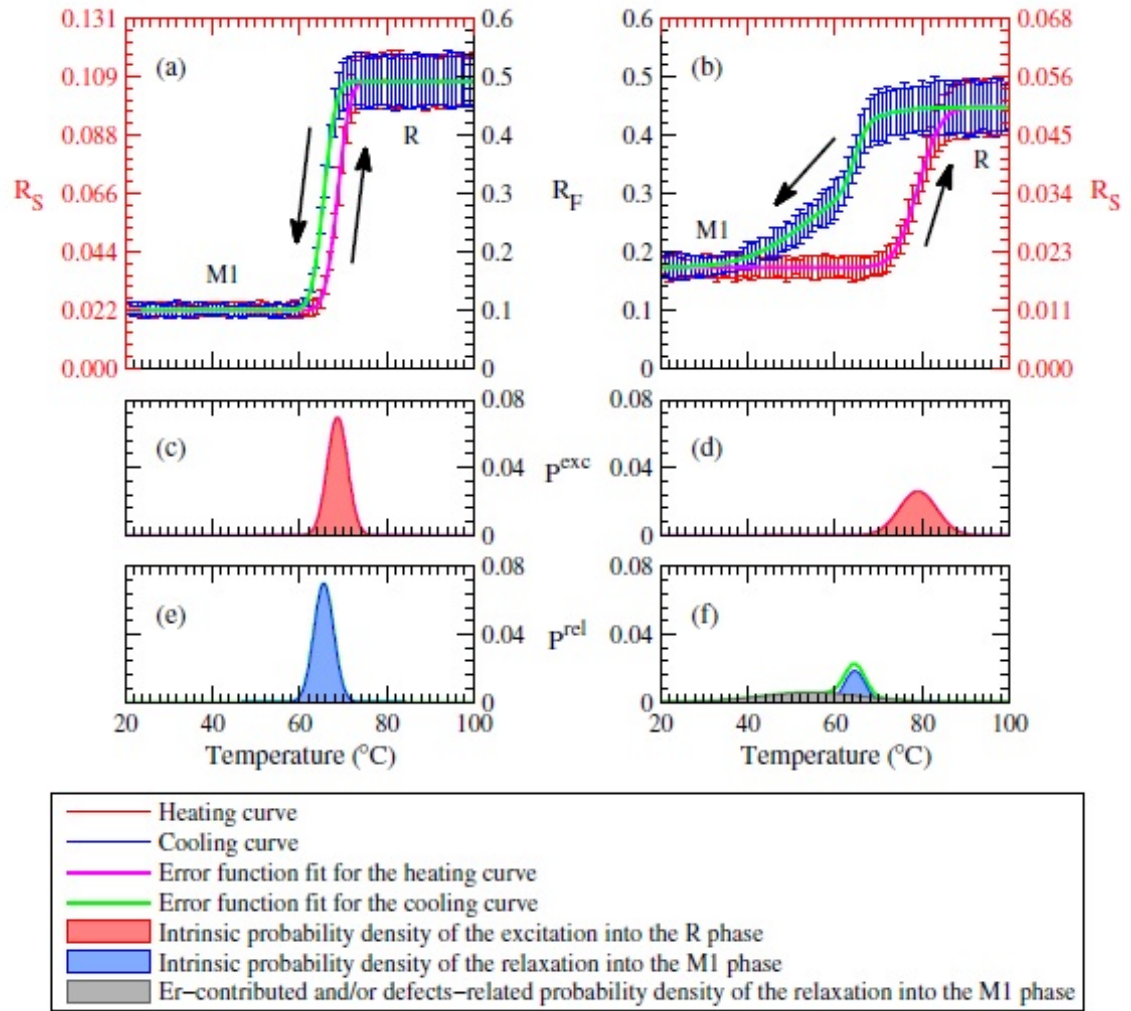


Figure 3.5: Temperature resolved reflectance for pure VO₂ annealed at 1000 C (a), and (b)Er implanted films annealed at 1000 °C. Black axes account for roughness dependent scattering, while red axes are the raw values. c-f) energy distribution for grains in the films. Color indicates heating or cooling. Distributions are plotted below their respective hysteresis curves[91].

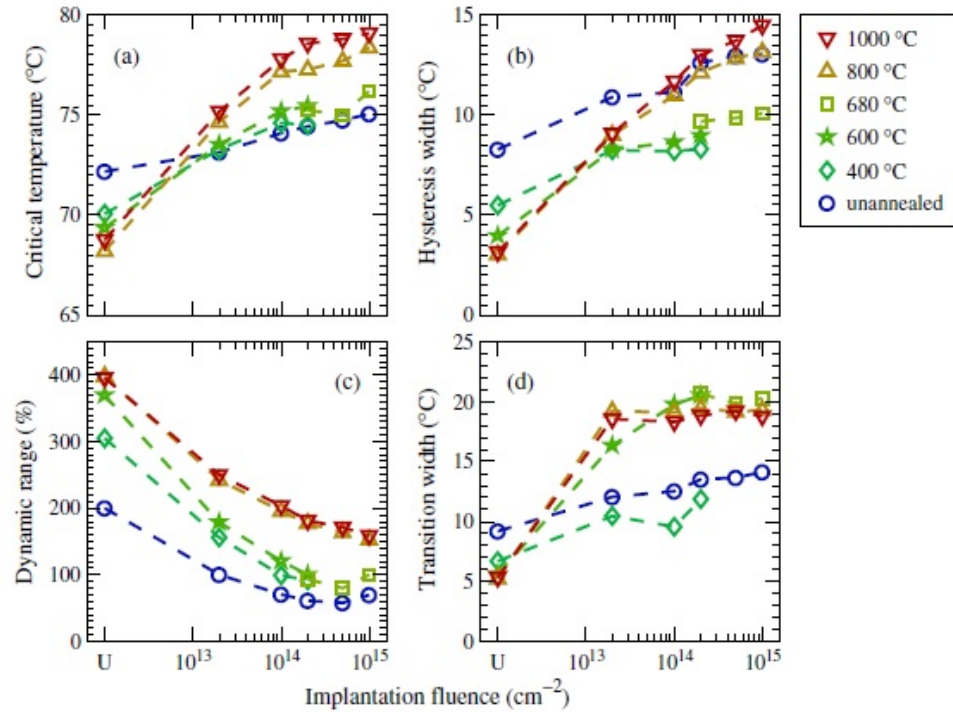


Figure 3.6: The phase transition parameters are presented with respect to implantation fluence and for different annealing temperatures. The x axis coordinate labeled U indicates unimplanted samples. The hysteresis parameters are (a) the critical temperature, (b) the hysteresis width, (c) the dynamic range, and (d) the mean transition width[91].

Figure 3.6 present the hysteresis parameters as a function of implantation fluence and for different annealing temperatures. For all samples the critical temperature increases with higher Er concentration, stabilizing the monoclinic phase and potentially eliminating defects or phase transition nucleation sites. The dynamic range (or hysteresis contrast) decreases with increasing Er concentration, but some of this can be recovered by annealing. In general, Er implantation is detrimental to the phase transition properties. This is consistent with many other reports on doping, all of which show that substituting other elements into the vanadium lattice is detrimental to the switching contrast.

3.3.6 Conclusions: Erbium Doped Thin Films

Incorporation of optically active erbium in VO₂ thin films has been demonstrated. The VO₂ crystal structure can provide the necessary octahedral oxygen atom coordination to support all of the Er³⁺ optical transitions without completely destroying the phase transition properties of the film. Annealing helps to recover some of the film phase transition properties but erbium implantation definitely degrades the hysteresis properties. The small change in luminescence may suggest that the crystal structure in VO₂ around the erbium atoms has not completely recovered from the implantation damage.

3.4 Erbium Doped Single Crystals

3.4.1 Erbium Single Crystals: Fabrication

VO₂ micro-beams were grown on silicon substrates using the same process described in Chapter 4.2. Er was then implanted by a low energy ion implanter at 80 keV and a fluence of $5 \times 10^{14} \text{ cm}^{-2}$. The single crystals were annealed at 825 °C in vacuum for half an hour to optically activate the erbium. Polarized Raman and PL measurements were used to examine the optical anisotropy.

3.4.2 Erbium Single Crystals: Results and Discussion

The results from polarization spectroscopy of a VO₂:Er micro-beam are presented in Fig. 3.7. To prevent the crystals from being damaged, the power of the excitation laser was limited and only a few of the Er³⁺ levels could be populated, preventing all of the levels from being observed. The Raman spectra observed were consistent with previous reports for VO₂[95], confirming the crystal quality. Only minor differences in the PL and Raman were observed when switching the polarization. The lack of polarization sensitivity could be due to the symmetry of the erbium electronic structure.

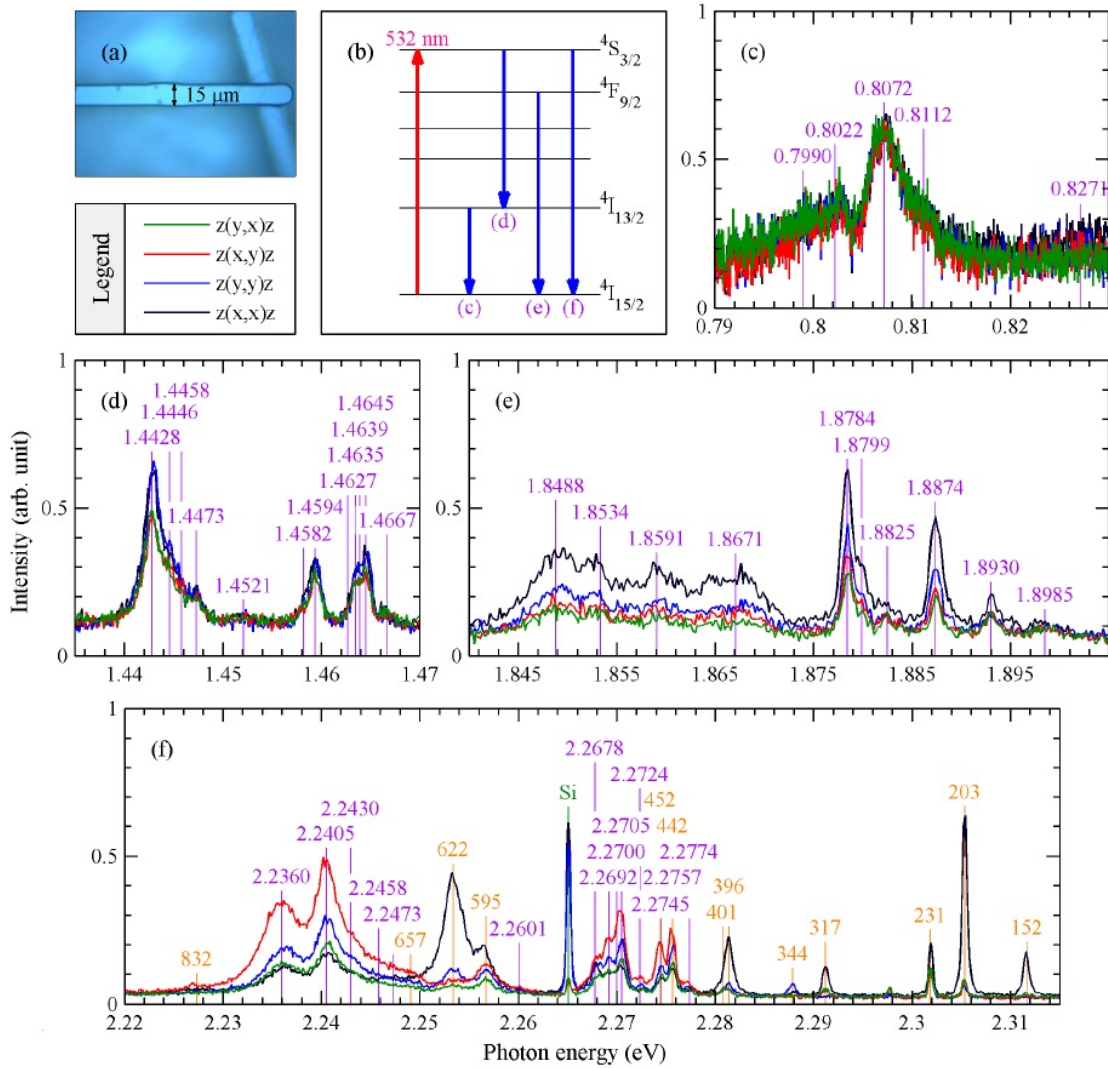


Figure 3.7: Polarization spectroscopy at $-195.6\text{ }^{\circ}\text{C}$ with 532 nm excitation and 2 mW power. (a) Photograph of the $\text{VO}_2\text{:Er}$ crystal being measured. The width of the beam is approximately $15\text{ }\mu\text{m}$. The polarization x-axis was oriented parallel to the crystal long axis. (b) Energy level diagram of Er^{3+} , showing the observed transitions. The measured PL spectra are shown in c-f. Different polarizations are plotted in each graph, as indicated in the legend. The positions of the Er^{3+} PL lines are labeled with purple texts (unit: eV). In f, the peaks labeled in orange are VO_2 Raman peaks, while the green peak is a Raman peak from the substrate[92].

3.4.3 Conclusions: Er Doped Crystals

The incorporation of Er^{3+} ions into VO_2 crystals was achieved via ion implantation followed by thermal annealing. From the PL measurements we determined that the required symmetry is achieved to optically activate the erbium. By increasing the Er implantation fluence, greater optical amplification through the Er^{3+} luminescence was achieved, however this occurs at the expense of the VO_2 transition properties. Annealing at $800\text{ }^\circ\text{C}$ or above is required to activate the optical transition in erbium. While annealing enhanced the reflectivity dynamic range, annealing at $1000\text{ }^\circ\text{C}$ degraded the VO_2 crystallinity. This work suggests that the optimal annealing temperature lies between $800\text{ }^\circ\text{C}$ and $1000\text{ }^\circ\text{C}$.

It is likely that the ion implantation process damages the single crystal significantly and can not be completely repaired by annealing. The damaged area around the implanted erbium ions may not be able to reconfigure easily, resulting in low PL signal from the erbium ions. To address this possibility we have attempted to incorporate erbium into VO_2 crystals during growth. First erbium metal was added to the V_2O_5 precursor, but no Er^{3+} PL was observed, likely due to the low vapor pressure, 10^{-6} Torr at $800\text{ }^\circ\text{C}$. Two other erbium precursors were added to the V_2O_5 precursor, erbium(III) oxalate decahydrate and erbium(II) nitrate hydrate. Both erbium precursors were consumed during the crystal growth and optical measurements are in progress to determine if optically activated erbium was incorporated.

3.5 Conclusions: Erbium and VO_2

Optically active erbium has been successfully incorporated into VO_2 thin films and single crystals using ion implantation and subsequent annealing. In thin films, the PL signal is large and all of the expected transitions are observed. In crystals the PL is much weaker and all the peaks are not observed. In films, weak modulation of the PL intensity at $1.53\text{ }\mu\text{m}$ is observed. Because the optical transitions of erbium are highly sensitive to the

local environment (oxygen octahedra), a better understanding of how the vanadium dioxide lattice forms around these dopants is needed. Incorporating erbium during film deposition or single crystal growth may help improve the crystal environment around the Er atoms and increase the PL intensity at $1.53 \mu\text{m}$. Ion implantation is known to damage crystalline materials[96] and direct examination of how the crystal structure recovers during annealing is needed to optimize performance.

Chapter 4

Processing VO₂ Thin Films and Crystals

4.1 Introduction

While producing electro-optic modulators, we observed significant differences in the electrical performance and reliability for devices with VO₂ produced by pulsed laser deposition (PLD) vs. sputtering. While the optical properties of films produced with these two processes were quite similar, the electrical characteristics were not. Devices with VO₂ produced by sputtering had sharper and more repeatable I-V curves while those made with PLD were not consistent and in many cases the yield per chip was very low. In the following Chapter, we explore the optical and morphological properties of thin films deposited by three different processes and consider the fundamental differences between the processes. We also produce crystals using a vapor transport process and attempt to control the size and shape.

4.2 Thin Films: Motivation

In the previous Chapter, two different mechanisms were used to drive the VO₂ phase transition, resulting in optical modulation. For ring-resonator devices, the phase transition was thermally driven by a heater or laser. In contrast, electro-optic modulators switch when voltage is applied across the VO₂ patch resulting in current flow through the patch and Joule heating[14]. On the micro-scale, these are very different mechanisms. When the transition is driven thermally (by external heater), the entire device is heated above the critical temperature and the phase transition occurs. Under slow optical excitation, the absorption of the device and power of the laser are large enough that everything is heated above the critical temperature. When electrical contacts are applied to a VO₂ film and the voltage is increased, a small conducting filament (string of metallic grains) forms

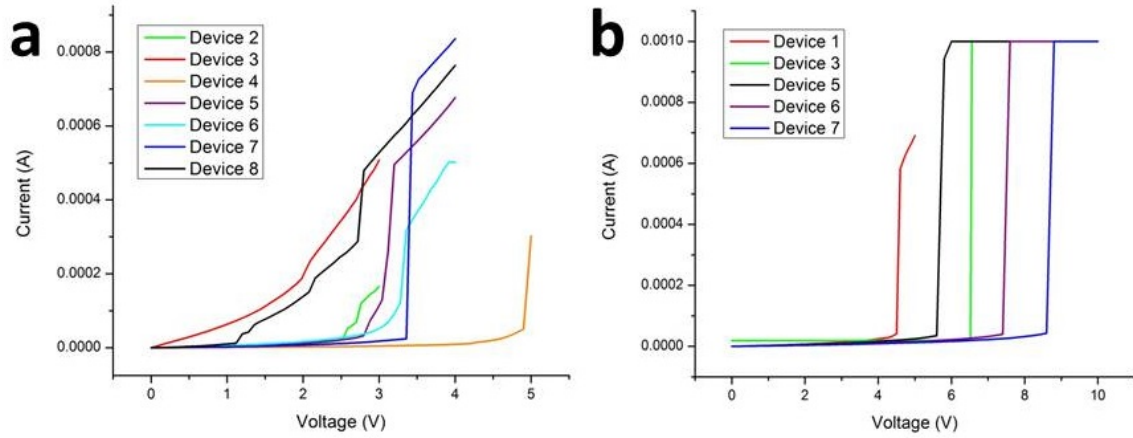


Figure 4.1: a) I-V curves for different VO₂ waveguide based optical modulators produced by pulsed laser deposition. b) I-V curves for the same devices but with VO₂ produced by sputtering.

connecting the contacts[97]. As current continues to flow through the initial filament, Joule heating increases the temperature of the initial filament and surrounding grains; increasing the number of metallic grains and the filament size.

The process of filament formation and growth depends on the transport properties of the film and therefore the grain structure. The first electro-optic devices were tested using VO₂ deposited by pulsed laser deposition (PLD). In Figure 4.1a, I-V curves for multiple devices produced by PLD are presented. There is large variation in the onset voltage and shape; in addition, few of the curves are sharp, resulting in very poor modulation characteristics. In comparison, the I-V curves for devices produced by sputtering, Figure 4.1b, have higher switching voltage and are much sharper. Devices with I-V characteristics similar to those shown in Figure 4.1b have much better reliability and are better optical modulators. After observing these differences, it became obvious that the properties of films deposited by different deposition processes needed to be explored. In the following sections, VO₂ film properties are compared for three thin film deposition processes: pulsed laser deposition, sputtering and e-beam evaporation.

4.2.1 Contributions

This section directly compares the performance and properties of thin films deposited on several substrates with different deposition processes. After fabricating the devices described in Chapter 2, it became obvious that a direct comparison was needed. The results of this work are published in *Acta Materialia*[98].

4.2.2 Introduction

The wide variety of VO₂ applications requires knowledge of film behavior on a variety of substrates, for different film thickness and across multiple deposition processes. However, to date there has been no systematic comparison of the influence of substrate and deposition process on VO₂ optical performance and morphology. Morphology, defects and strain are known to be critical for tuning the phase transition[99, 84, 5, 33, 100, 41, 42], highlighting the importance of understanding the influence of the substrate and deposition process.

In this Chapter we show how the film morphology and optical performance evolve with annealing time for films deposited by pulsed laser deposition (PLD), electron beam evaporation and rf magnetron sputtering. In contrast to many other processes which deposit VO₂ at elevated temperature[35, 99, 101, 102], we use post-deposition annealing to crystallize films deposited at room temperature, which makes this process compatible with PMMA based lithography and uses the lowest annealing temperature and shortest annealing time possible. Our results show that grain growth in films deposited by rf magnetron sputtering is dominated by deposition-induced strain. In contrast, dewetting plays a critical role in the evolution of film morphology when films are deposited by pulsed laser deposition or electron beam evaporation. The importance of lattice matching between the VO₂ film and sapphire is evident, in that films deposited by all three techniques on sapphire remained stable during prolonged annealing.

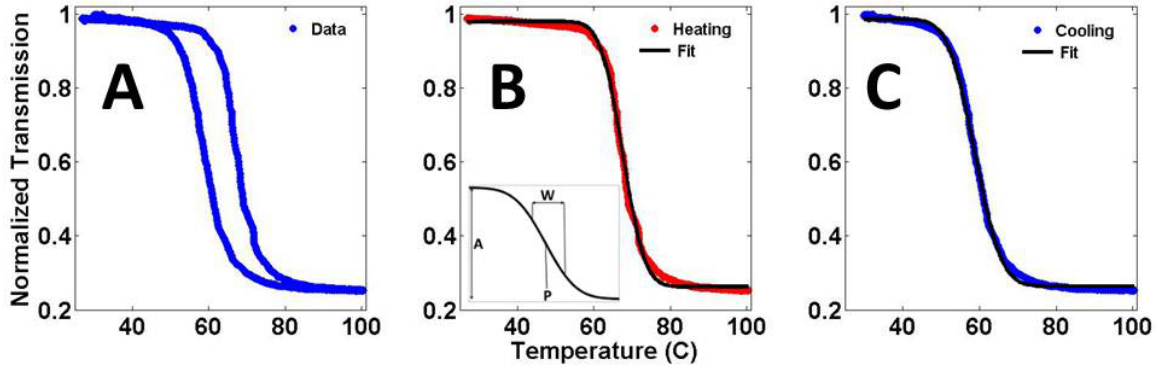


Figure 4.2: A) Optical hysteresis curve for VO₂ thin film (deposited by PLD on glass and annealed for five minutes) measured in transmission at 1550 nm. B) Heating curve with sigmoidal fit and inset illustrating fit parameters. C) Cooling curve with sigmoidal fit[98].

4.3 Thin Films: Experimental

4.3.1 Substrates

Amorphous VO_x films were deposited on three substrates: silicon (100) with an approximately 15 Å thick (as measured by ellipsometry) native oxide layer, sapphire (0001) and glass; more detailed information is provided in Table 4.1.

4.3.2 Deposition Processes

The deposition parameters for each physical vapor deposition (PVD) process were tuned such that the deposited film had the required 1:2 vanadium to oxygen atom stoichiometry, as verified by Rutherford backscattering spectrometry (RBS). All films were deposited at room temperature, as measured by a thermocouple in contact with the substrate holder and were deposited in a single run for each process type, eliminating run-to-run variations. As-deposited film thickness was confirmed using shadow mask lithography and a Dektak profilometer; all samples were determined to be 90±5 nm thick. For x-ray reflectivity measurements, large (4 cm x 4 cm) substrates were required and deposited separately. Table 4.2 compares the deposition processes.

Table 4.1: Tabulation of substrate physical properties. Information is provided from supplier data sheets unless otherwise noted.

Substrate	Supplier	Crystal Orientation	Epitaxial with VO ₂	Surface Energy (ergs/cm ²)	CTE (x 10 ⁻⁶ /°C)
Silicon	MTI	(100)	No	2130[103]	4.0
Sapphire	MTI	(0001)	Yes	890[104]	7.5
Glass	Corning 1737	NA	NA	260[105]	3.7

PLD deposition was performed using a Epion PLD-3000 system with a Lambda Physik (Coherent COMPex) excimer laser operating at 248 nm (KrF), 4 J/cm² per pulse, 25 hz repetition rate and 25 ns pulse duration. Prior to deposition the chamber was pumped down to 9x10⁻⁷ Torr. Ablation of a pure vanadium metal target was performed in ultra-high purity oxygen environment at 1.1x10⁻² Torr with 2 sccm flow. The laser beam was rastered across the rotating target, while the substrate holder, located 8 cm above the target, also rotated. The average deposition rate was 0.3 Å/s.

An Ångström Engineering Inc. deposition system was used for rf magnetron sputtering and electron beam evaporation; both processes were performed in the same chamber. For sputtering, a 5 cm diameter vanadium metal target was sputtered at 270 Watts, 6.0x10⁻³ Torr pressure, 20 sccm Ar and 1 sccm O₂. The chamber was conditioned under these conditions for 45 minutes prior to opening the sample shutter and beginning deposition. The deposition rate remained constant at 1 Å/s, as measured by quartz crystal microbalance. Electron beam evaporation was carried out at 5x10⁻⁶ Torr. The electron beam was rastered across the VO₂ powder precursor (Materion) while increasing the power until the evaporation rate stabilized at 1 Å/s, at which point the sample shutter was opened and the deposition initiated.

4.3.3 Annealing

The deposited films were annealed in sets of nine (three substrates and three deposition processes) inside a tube furnace for 2,5,10,30 and 90 minutes at 450 °C. The tube was

Table 4.2: Comparison of the three deposition processes. Energy given is for the ejected target material before contacting the substrate. The flux-to-diffusion ratio is a measure of how adatom mobility (Energy) is affected by atoms impacting the film surface (Rate) and is discussed more below.

Process	Species	Rate	Energy	Flux-to-Diffusion
Pulsed laser deposition (PLD)	UV photons	0.3 Å/s	50 eV[106]	0.006
Electron beam evaporation	electrons	1 Å/s	~200 meV[107]	5
RF magnetron sputtering	Ar ions	1 Å/s	10-40 eV[108]	0.04

pumped down to ~ 1 mTorr before annealing at 250 mTorr O_2 . After annealing for the specified time, the samples were moved out of the heated zone and allowed to cool in the tube before exposing them to ambient conditions. The labeling scheme used to identify the 45 different samples produced in this work is presented in Table 4.3. Without annealing films do not exhibit a phase transition.

4.3.4 Rutherford backscattering spectrometry

Rutherford backscattering spectrometry (RBS) was conducted at Vanderbilt University using a NEC 6SDH pelletron accelerator equipped with an Alphatross ion source. Helium ions (He^{++} , 2.0 MeV) irradiated the sample at an incident angle of 180° to the sample normal and the backscattered particles were detected at a scattering angle of 160° . The detector was calibrated with a Bi^{209} implanted (100) boron-doped silicon wafer, implanted to 5×10^{15} atoms/cm² at 30 keV. A total charge of 5 μC was collected on all samples.

4.3.5 X-ray photoelectron spectroscopy

X-ray photoelectron spectroscopy (XPS) data were collected using a Physical Electronics (PHI) VersaProbe 5000. A 200 μm diameter, 50 W monochromatic aluminum $K\alpha$ x-ray beam was used at a takeoff angle $10-80^\circ$ from sample normal. Post-annealed samples were analyzed at a takeoff angle of 45° relative to sample normal, rastering over a 400 $\mu m \times 400 \mu m$ area. Charge neutralization was accomplished using 1.1 eV electrons and 10

Table 4.3: Sample labeling scheme used in this work. Example: P_Sa_30 = is a film deposited by PLD on sapphire and annealed for 30 minutes

Deposition Process	Substrate	Annealing Time (minutes)
P = PLD	G = Glass	2,5,10,30,90
E = Electron Beam Evaporation	Sa = Sapphire 0001	2,5,10,30,90
S = RF Sputtering	Si = Silicon 100	2,5,10,30,90

eV Ar⁺. Survey and high-resolution spectra were acquired with pass energies of 187.85 eV and 11.75 eV, respectively. Data were analyzed using CasaXPS with PHI handbook[109] sensitivity factors. Spectral peaks were fit using 70%-30% Gaussian-Lorentzian peaks with a Shirley background function as shown in Figure 4.3.

4.3.6 X-ray reflectivity

A Panalytical X'Pert MRD instrument with Cu K α radiation, set up in a parallel beam geometry, was used to acquire X-ray reflectivity (XRR) curves from the deposited films. The film density, thickness, and surface roughness were obtained from simulations of the XRR curves using commercially available software (X'Pert Reflectivity, from Panalytical) and a model consisting of four layers: substrate, an interfacial layer accounting for the silicon native oxide and any ions that were subplanted/mixed within this layer, the bulk layer and a surface-contamination layer accounting for the surface roughness and any hydroxide/carbon contaminants present on the topmost surface when films were exposed to the ambient.

4.3.7 Optical Characterization

Optical characterization across the thermally induced phase transition was performed using a 1550 nm diode laser and an InGaAs photodetector in transmission geometry with 3 mm spot size. A transmission curve is presented in Figure 4.2A. A lock-in detector and chopper were used to record the optical intensity as the sample was heated from 25°C \rightarrow 100°C \rightarrow 25°C with a peltier heater. The hysteresis parameters were extracted by fitting the

sigmoidal function in Equation 4.1 to the temperature-resolved transmission during heating and cooling cycles separately.

$$I(T) = A \left[1 + \operatorname{erf} \left(2\sqrt{\ln 2} \frac{T - P}{W} \right) \right] \quad (4.1)$$

Where A determines the amplitude, P is the center of the transition curve and W is the full width at half maximum (see inset Figure 4.2B). The difference ($P_{heating} - P_{cooling}$) is the hysteresis width. The contrast is taken as the difference between the upper and lower steady-state transmission values. A sample hysteresis curve is presented in Figure 4.2A along with sigmoidal fits to the heating (Figure 4.2B) and cooling (Figure 4.2C) curves. A global fitting routine is used to minimize the error between experiment and fit, see S14 in Appendix A for the fit quality range.

Raman spectra were acquired using a Thermo Scientific DXR microscope with unpolarized 532 nm excitation using a 50X objective with 0.3 mW excitation power. VO₂ has 18 Raman modes[95] in the monoclinic state and one very broad peak in the rutile. Use of Raman spectroscopy provides compositional information about the bulk material, in contrast to XPS which is surface sensitive.

4.3.8 Morphology

Atomic force microscopy was performed using a JEOL 5200 Scanning Probe Microscope (AFM) in tapping mode, with a nominally 10 nm diameter tip. Using AFM provides high-quality images without regard to the conductivity of the the substrate, in contrast to SEM imaging which typically requires a conductive surface or substrate. Image leveling and analysis was performed using Gwyddion[110] software. RMS roughness values for each sample are recorded in Appendix A (S10).

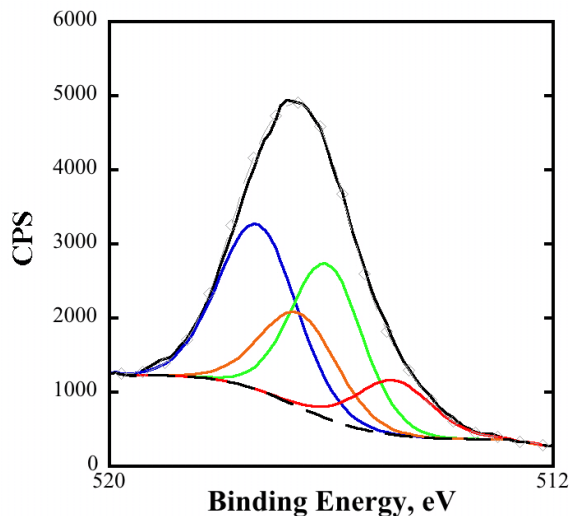


Figure 4.3: XPS spectra (Black) of $V2p_{3/2}$ peak for an as-deposited film sputtered on silicon. Peak deconvolution suggests the presence of four vanadium oxides, V_2O_5 (blue), V_6O_{13} (orange), VO_2 (green) and V_2O_3 (red).[111, 112, 98]

4.4 Thin Films: Results and Discussion

4.4.1 Composition

Each deposition processes was calibrated with RBS, prior to deposition, to ensure that all films contained the desired 1:2 vanadium:oxygen stoichiometry, reducing the impact of oxygen diffusion during annealing. XPS spectra were acquired on one, as-deposited film on silicon, from each deposition process. The $V2p_{3/2}$ peak was deconvoluted as shown in Figure 4.3, and the contribution of each bonding state to the total peak area is recorded in Table 4.4. The XPS data on the as-deposited amorphous films show that V_2O_5 and VO_2 are the dominant bonding states. The data do not indicate a trend in the distribution of bonding states between the three deposition processes. There is a small discrepancy between the stoichiometry measured by RBS and XPS (Appendix A, S11), most probably due to surface contamination. We emphasize that these are as-deposited amorphous films which do not exhibit a phase transition without annealing.

The spectra taken at 10 degrees relative to the sample normal provide information on

Table 4.4: Deconvolution of $V2p_{3/2}$ peak bonding states for as-deposited films. Values given represent the contribution to total peak area for each bonding state.

Sample	$V_2O_5(\%)$	$V_6O_{13}(\%)$	$VO_2(\%)$	$V_2O_3(\%)$
PLD on Si	62.2	-	35.4	2.4
E-beam on Si	41.1	7.0	42.6	9.3
RF sputtering on Si	35.5	20.0	29.5	14.9

the top 10-15 nm of the ~ 90 nm thick sample; however, we assume the analysis is representative of the bulk composition due to the low temperature of the deposition. As-deposited films produced by PLD appear to have the fewest number of bonding states, with V_2O_5 and VO_2 accounting for $\sim 97\%$ of the total. Zhang[113] measured almost the same composition for as-deposited ALD films as we do for PLD. Films deposited by e-beam start off with the most VO_2 (43%); however they appear to have the least stability during annealing, as demonstrated by the rapid degradation in switching contrast for long annealing times, Figure 4.4. In contrast, sputtered films have a composition almost uniformly distributed between the four oxides present and are the most stable for longer annealing times. When comparing the evolution of the hysteretic response for annealed films, the VO_2 content of the as-deposited films does not appear to matter.

4.4.2 Optical Performance

Optical and electrical measurements are typically used to characterize the phase transition properties of VO_2 films. Optical measurements, either in reflection or transmission geometry, take advantage of the large difference in dielectric function between the semiconducting and metallic states[11]. At any given point during the thermally induced phase transition some fraction of the crystal domains are semiconducting while the rest are metallic. The optical hysteresis is a composite measurement of the film optical properties within the beam spot. The width of the hysteresis depends on the density of defects, which provide nucleation centers for the phase transition[42]. Electrical measurements, on the other hand, rely on the large change in resistance between the insulating and metallic states, up

to five orders of magnitude[2]. Formation of a conductive path proceeds by small current avalanches[114], which occur as domains between the contacts turn metallic, culminating in a continuous percolation[115] path of metallic VO₂ with lowest resistance.

In both types of measurement, the percolation behavior determines the width and symmetry of the phase transition. For electrical measurements the contrast is highest for single crystals and smooth highly oriented films. For optical measurements the contrast depends on film thickness and the presence of non-stoichiometric phases. Electrical and optical measurements of thin VO₂ films on glass and ITO coated glass have recently been compared[102], demonstrating that substrate and morphology significantly influence hysteresis contrast for electrical measurements. In comparison, the optical measurements show nearly identical contrast with expected differences in the cooling curve shape primarily due to grain size and defects[42]. Given that a continuous conductive path must form, it is to be expected that grain boundaries and separation between grains will significantly influence electrical measurements. Since the morphology of the films produced in this work is quite varied and in some cases not continuous, we have elected to use optical measurements as a figure of merit for the phase transition, as it is difficult for electrical measurements to differentiate between a discontinuous morphology and the presence of non-switching vanadium oxide.

By using 1550 nm laser illumination for hysteresis measurements, we take advantage of the significant change in extinction coefficient accompanying the phase transition, from $k = 0.3$ at 25 °C to $k = 3.4$ at 90 °C [11]. Given the film thickness and optical properties we can use Beer's law, Equation 4.2, to calculate the expected change in transmission across the phase transition.

$$I(T) = I_0 e^{-\alpha(T) \cdot z} \quad (4.2)$$

I_0 is the incident light intensity, α is proportional to the temperature dependent extinction coefficient k and z is the film thickness. Using the average film thickness (90 nm) and

the optical constants above, the expected change in transmission across the phase transition is calculated to be 90 %. When comparing samples, the effect of surface roughness on the intensity of transmitted light can also be accounted for, as outlined by Bennett[116], however the contribution does not exceed 1% until the RMS surface roughness is in excess of 40 nm at 1550 nm. Hence, degradation in switching contrast cannot be attributed to increased surface roughness even in samples annealed for very long times.

From the hysteresis contrast values plotted in Figure 4.4, films on silicon and glass substrates appear to be unstable for longer annealing times; this is also the case for sputtered films but is not as pronounced. The hysteresis contrast for films deposited on sapphire is stable across the full range of annealing conditions, likely due to the epitaxial relationship between the film and substrate[70]. Given that glass is the most prone to dewetting (see section 4.4.3) and lacks any long-range crystal structure for epitaxy, it is not surprising that films on glass have poor stability with prolonged annealing.

The hysteresis width provides information about the competition between grain size and defect formation[42]. In general, for films deposited by PLD and e-beam the hysteresis width decreases or remains constant, with increasing grain size. Lopez[117] and Appavoo[41] observe similar trends, where the hysteresis width is observed to decrease with increasing grain size, a result of the reduced density of phase transition nucleating defects. In contrast, sputtered films show increased hysteresis width as the grain size increases. In the context of the above theory, it is not clear why sputtered films have the opposite trend.

The small variation in hysteresis width observed for films deposited by electron beam evaporation is in line with the minimal increase in surface roughness observed and lack of well-defined grains. It is surprising that the significant decrease in switching contrast observed for annealing times longer than 30 minutes is not accompanied by a change in the hysteresis width. The degradation of switching performance clearly indicates the formation of other oxides (film defects) but they do not affect the hysteresis width. It is possible that

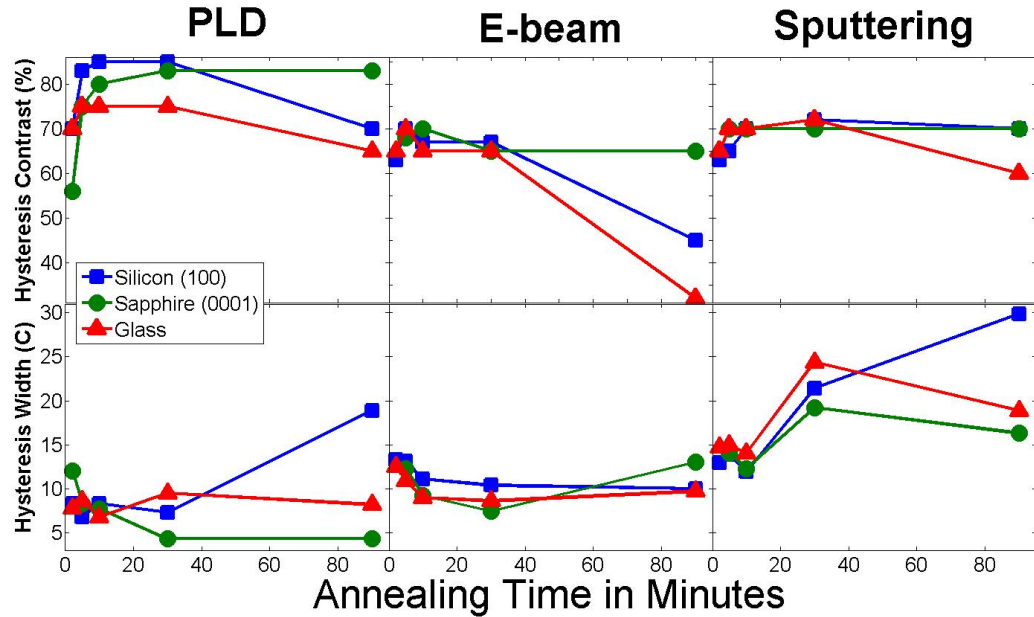


Figure 4.4: Optical hysteresis parameters measured across the thermally induced phase transition at 1550 nm. Lines connecting the data points are added to clearly demonstrate the trends with annealing time[98].

entire grains are converted to another oxide of vanadium without influencing the phase transition properties of the surrounding VO_2 grains. Another point of interest is the constant hysteresis width observed for the P_Sa series of samples. Despite an obvious increase in grain size (see section 4.4.3), the hysteresis width remains constant, indicating that the defects required to maintain a narrow hysteresis are not being eliminated by grain growth[42]. The stability of this series of films highlights the benefits of the epitaxial relationship between film and substrate, and demonstrates the well known capability of PLD to deposit high-contrast stable films[33].

To investigate the steep decline in hysteresis contrast with prolonged annealing for films deposited by electron beam evaporation on silicon, we compare Raman spectra and XPS measurements for E_Si_30 and E_Si_90 (see Appendix A, S11 and S14). XPS shows that V_2O_5 and VO_2 are the only oxides present, and that the amount of V_2O_5 almost doubles

from 30 minutes to 90 minutes of annealing. The Raman spectra show peaks that can be clearly assigned to VO₂ and the silicon substrate, however there are several prominent peaks that cannot be attributed to either V₂O₅ or V₂O₃. It is likely that amorphous material on the surface is responsible for the XPS signal, while bulk crystalline material underneath provides the Raman signal. Given the well-defined granular structure of the film and the large holes throughout (Appendix A, S4), XPS should be sensitive to composition throughout the entire film thickness via the holes and deep grain boundaries. It is not clear why strong peaks in the Raman spectra do not show up in XPS.

4.4.3 Morphology

The influence of VO₂ film grain structure on the phase transition has recently been highlighted[99, 84, 100]. Using near-field scanning microscopy (NSOM) to image the percolation behavior of the phase transition, Liu *et al.*[99] observe stripe evolution in the percolation for films deposited by reactive ion sputtering on TiO₂ which is in contrast to previous work[84] which showed a more random behavior for sol-gel deposited films on sapphire. They attribute this behavior to the strain state of the film, demonstrating how the percolation behavior can vary. Lysenko *et. al.*[100] performed ultrafast scattering measurements and observed variation in switching time for grains of different sizes. They attribute this behavior to defects, which have been shown to play a key role in nucleating the phase transition[41]. These examples highlight the importance of the film structure and underscore the critical role that it plays in determining the phase-transition properties.

Figure 4.5 presents a set of AFM images representative of the regimes of morphological evolution observed. PLD deposited films on glass and silicon exhibit the evolution shown in 4.5A and 4.5B, in contrast, films deposited on sapphire grow as shown in 4.5E and 4.5F. All films deposited by e-beam exhibit the "star shaped" patterns shown in 4.5C for short (10 minutes or less) annealing times and with longer times have three-dimensional grain growth as shown in 4.5D. The third evolution regime is presented in 4.5E and 4.5F

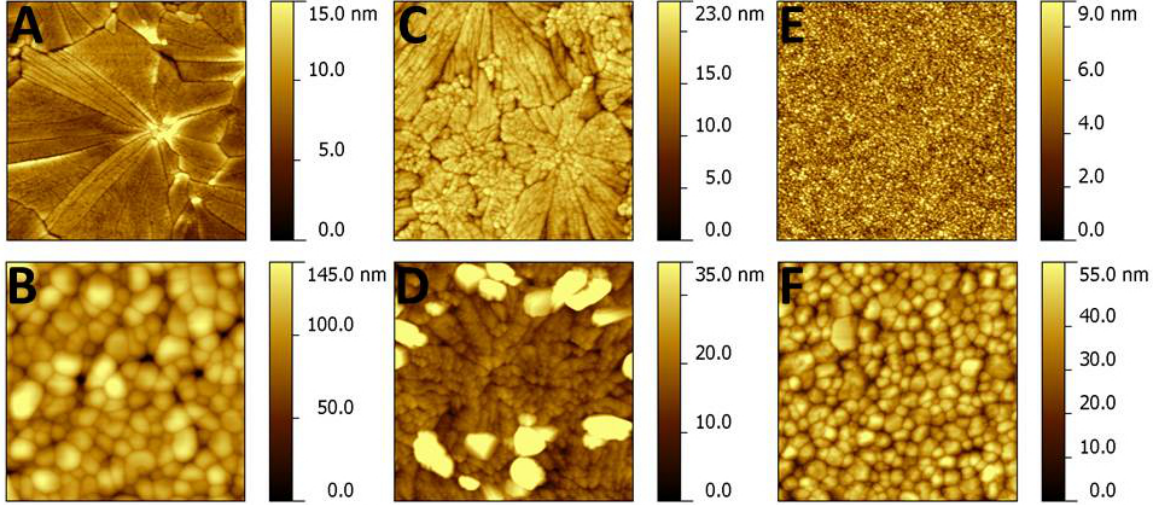


Figure 4.5: Film morphology evolution regimes, A) P_G_10, B) P_G_30, C) E_Sa_10, D) E_Sa_30 , E) S_Si_5 and F) S_Si_90. Detailed sample description is found in Table 4.3. All images are $2\mu\text{m} \times 2\mu\text{m}$ [98].

and is observed for all films deposited by sputtering. For sputtering, the grain size varies when comparing substrates but the size distribution and shape are similar. AFM images for all samples produced in this work can be found in Appendix A, S1-9.

Surface energy forces, and specifically dewetting, are known to have significant influence on the morphological evolution of thin films[118]. A film is stable against dewetting forces if the following condition is satisfied;

$$\gamma_s > \gamma_i + \gamma_f \quad (4.3)$$

where γ_s , γ_i and γ_f are the substrate, interface and film surface energies respectively. Although the film and interface energies are not known for VO_2 , the three substrate surface energies are: 2130 ergs/cm^2 silicon (100)[103], 890 ergs/cm^2 sapphire (0001)[104] and 260 ergs/cm^2 for glass[105]. Thomas[119] performed contact angle measurements on silicon samples with oxide thickness from $30\text{-}10000 \text{ \AA}$, and found comparable behavior to bulk glass at 500 \AA . Films in this work are deposited on silicon with 15 \AA oxide thickness and the value quoted above for silicon surface energy is probably high; however the relative

ordering should still be accurate. The ordering of these surface energy values is consistent with the RMS roughness trends (see Appendix A, S11), with roughness values increasing for decreasing surface energy, consistent with Equation 4.3. The one exception is for the P_Sa_90 film which has considerably lower roughness than P_G_90 or P_Si_90. Sapphire substrates, across all deposition conditions, have comparable RMS roughness values (15-17 nm) even after 90 minutes of annealing, likely stabilized by the epitaxial relationship between the VO₂ (010) and sapphire (001) crystal planes.

Closer examination of the AFM images shows that dewetting plays a significant role in the morphological evolution. Edge retraction (Figure 4.6C) and fingering instability, (Figure 4.6B) are two mechanisms which contribute to hole formation. In Figure 4.6A significant ridges are observed on the edges of the retracting film indicating that mass transport from the triple line (substrate-film-ambient interface) has occurred, characteristic of dewetting, as opposed to cracking behavior due to mismatch in thermal expansion. Perpendicular to the retracting edges, evidence of fingering instability is observed. The combination of these two dewetting mechanisms drives the evolution of the film structure for the P_Si, P_G, E_Si, E_Sa and E_G samples, as shown in Figure 4.7.

In Figure 4.7 the P_Si series of samples is used to demonstrate how the evolution of film structure is governed by dewetting phenomena. After two minutes of annealing, grooves form, emanating from a central point, Figure 4.7A. With continued annealing, the initial grooves become well defined and new grooves form, also emanating from the same central point, Figure 4.7B. After thirty minutes the grains are well defined and are oriented with the longer dimension parallel to the initial grooves. Rather than extending the entire length of each groove, the grains are broken perpendicular to the initial grooves due to fingering instability, Figure 4.7C. It is clear that for annealing times up to 30 minutes the grain growth and orientation are controlled by dewetting. For samples deposited by PLD, annealing times longer than thirty minutes produce a film structure that can no longer be related to the initial dewetting behavior; however, this behavior is not observed for samples deposited

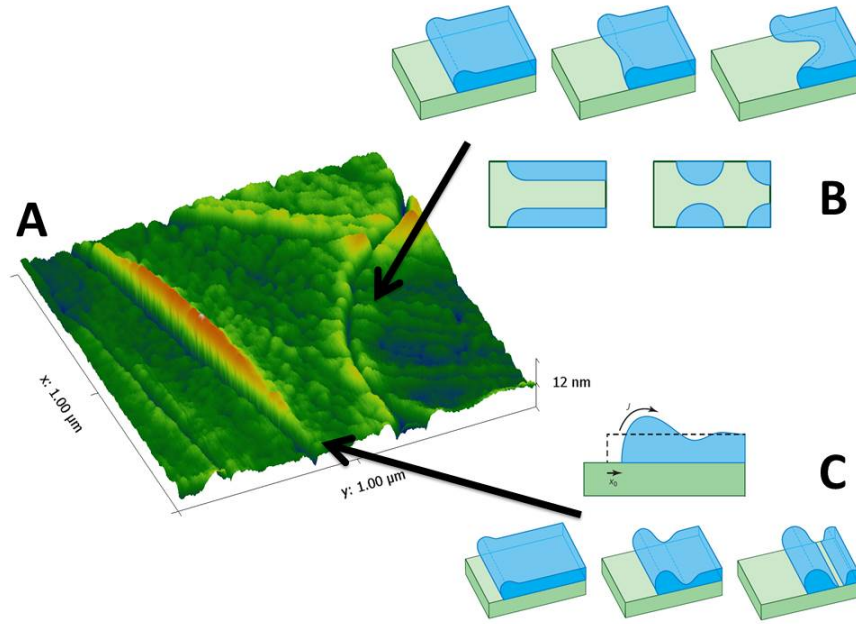


Figure 4.6: AFM image of VO_2 film (A) showing evidence of dewetting; fingering instability (B) and edge retraction (C)[98]. B and C reprinted with permission from the Annual Review of Materials Research, Volume 42 2012 by Annual Reviews, <http://www.annualreviews.org>

by PLD onto sapphire substrates.

For films deposited by e-beam evaporation there is evidence of similar evolution, as described in Figure 4.7, though not as pronounced. These films appear much more granular after short annealing times, similar to the sputtered films, possibly due to faster grain growth or increased dewetting for e-beam films compared to PLD. The most striking feature occurs on films annealed for thirty minutes and longer, with large structures projecting out of the film typically 40 nm high or more, Figure 4.5D (see Appendix A S4-6). The formation of these out-of-plane features is not accompanied by a reduction in the hysteresis contrast, indicating that they are switching VO_2 crystallites. Given that the structures appear and then disappear for longer annealing times and do not affect phase transition properties (E_Sa series), it is likely they are formed as a stress-relaxation mechanism.

In contrast to the films grown by PLD and e-beam evaporation, the growth of films deposited by sputtering does not appear to be strongly influenced by the substrate. During

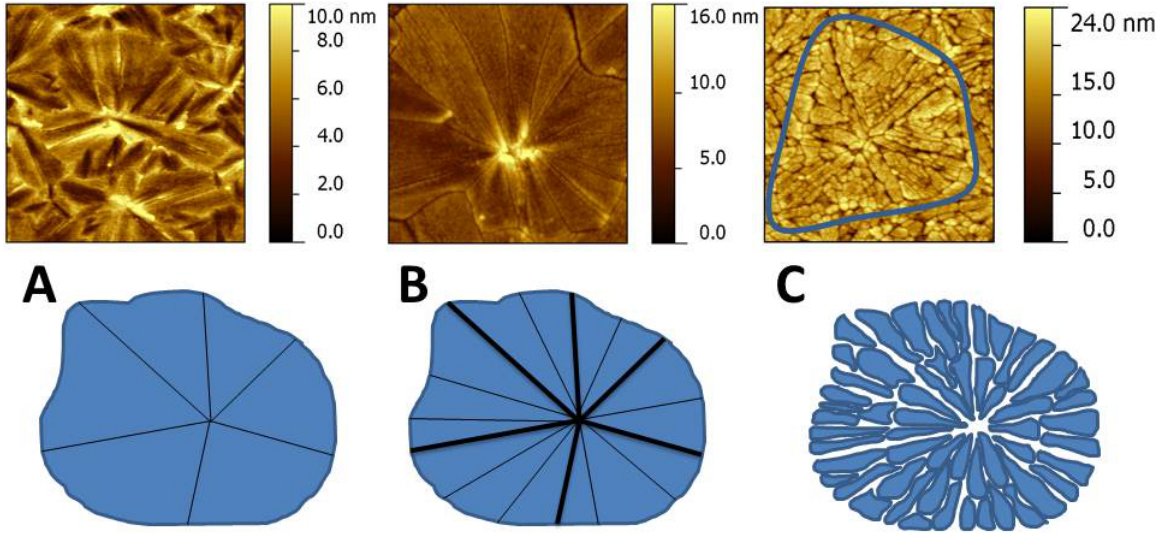


Figure 4.7: AFM images (top) are accompanied by schematics (bottom) to illustrate how dewetting drives the morphological evolution. Films initially show poorly defined grooves (A) P_Si_2. With longer annealing times the initial grooves deepen and new grooves form (B) P_Si_10 and with prolonged annealing edge retraction and fingering instability dominate the grain structure of the film (C) P_Si_30. All images are $2\ \mu\text{m} \times 2\ \mu\text{m}$ [98].

sputtering, the substrate and growing film are subject to resputtering and ion bombardment, which have been shown to influence the morphology [120]. When sputtering, the target and substrate are the electrodes between which the plasma is formed [108]. The uniform grain structure of the sputtered films is due to the presence of compressive strain imparted during the deposition [121], a result of the “shot peening” [122, 108] characteristic of sputtering that is consistent with films produced by other groups [102, 101]. This description of the sputtering process is consistent with the increased density measured by x-ray reflectivity and presented in section 4.4.4.

We consider other possible mechanisms which could produce the morphology observed above. The flux-to-diffusion ratio considers how atoms impacting the substrate (deposition rate, Table 4.2) limit the surface diffusion of existing adatoms (energy, Table 4.2). Low flux-to-diffusion indicates that adatoms are highly mobile and form a more dense film while high values indicate reduced mobility and lower film density. The flux-to-diffusion ratio for each process is presented in Table 4.2. PLD and e-beam films both have similar mor-

Table 4.5: Layered structure of films deposited on silicon as determined by x-ray reflectivity measurements.

Layer	PLD on Si		Sputter on Si		E-beam on Si	
	Density (g/cm ³)	Thickness (nm)	Density (g/cm ³)	Thickness (nm)	Density (g/cm ³)	Thickness (nm)
Surface	2.4	10.1	2.3	10.6	3.4	9.2
Bulk	4.0	129.0	4.5	99.3	3.8	81.5
Interface	2.2	1.7	1.8	2.0	2.1	1.6
Substrate	2.3	6x10 ⁵	2.3	6x10 ⁵	2.3	6x10 ⁵

phologies, but three orders of magnitude separate the flux-to-diffusion ratio. Another factor potentially influencing grain structure is thermal mismatch between the substrate Table 4.1, and VO₂ (2.1x10⁻⁵/°C[123]). Films sputtered on all three substrates have nearly identical small scale structures, with no differences that can be attributed to thermal expansion.

4.4.4 X-ray reflectivity

To provide additional insight into the film structure and crystallization we performed x-ray reflectivity measurements on ~100 nm films, on silicon and sapphire substrates annealed for 10 minutes. The reflectivity data are modeled using four layers with thickness and density varying for each, as outlined in section 4.3.6. The density and thickness values which produced the best agreement between experimental data and the model are presented below in Table 4.5 and Table 4.6. For the silicon interface, a 1-2 nm thick layer was measured with a density of 1.7-2.1 g/cm³, most likely silicon native oxide (SiO₂ 2.0 g/cm³). Other possibilities might include VSi₂ and other oxides of vanadium; however the density for these materials ranges from 3.4-4.8 g/cm³.

The density of the bulk layer is observed to be highest for sputtered films and lowest for e-beam deposited films. The density of VO₂ is 4.5 g/cm³ and agrees well with the sputtered film. Films deposited by e-beam and PLD are less dense, but can still be identified as VO₂ since they exhibit a phase transition with the expected optical contrast. Finally, a surface contamination/oxide layer ~10 nm thick is observed for all samples.

The interface layer density for films deposited by PLD and sputtering on sapphire is 4.8-4.9 g/cm³ and agrees well with V₂O₃ (4.87 g/cm³). This is further supported by the work of Zhou [124], who observed by TEM a V₂O₃-like interfacial layer for VO₂ films deposited by PLD on c-sapphire. The composition of the interfacial layer for the film deposited by e-beam is difficult to assign because the density is consistent with multiple oxides of vanadium including VO₂. The density of the bulk film agrees with the values measured for films on silicon and shows the same trend with sputtered films having the highest density and e-beam the lowest. When comparing the surface layer properties, the only noticeable difference is the reduced thickness for films deposited by e-beam. It is important to note that the surface layer accounts for roughness, voids and contamination which decrease the density. In contrast, XPS is only sensitive to the contamination, which makes a direct comparison between XPS and XRR surface measurements difficult.

4.5 Thin Films: Conclusions

We have shown that the optical properties during the phase transition, morphology, density and stability of vanadium dioxide thin films depend heavily on the substrate and deposition process. When considering films deposited by sputtering it is clear that the morphological evolution is dominated by strain imparted during the sputtering process. For films deposited by PLD and electron beam evaporation, the substrate plays a more important role, with substrate dewetting and epitaxy determining the film structure during solid-phase crystallization. The stability of vanadium dioxide, as measured by optical hysteresis contrast, is a function of the deposition process and the substrate. In addition, we have shown that maximum switching contrast may be obtained for annealing times of ten minutes or less for all substrates and deposition processes, producing films with RMS roughness values less than 4 nm in all cases. This result is especially relevant to applications where annealing time and temperature must be minimized and where smooth films are required.

Table 4.6: Layered structure of films deposited on sapphire as determined by x-ray reflectivity measurements.

Layer	PLD on Al ₂ O ₃		Sputter on Al ₂ O ₃		E-beam on Al ₂ O ₃	
	Density (g/cm ³)	Thickness (nm)	Density (g/cm ³)	Thickness (nm)	Density (g/cm ³)	Thickness (nm)
Surface	1.9	9.3	2.5	9.6	1.7	4.8
Bulk	3.9	108.6	4.2	94.3	3.7	102
Interface	4.8	3.2	4.9	3.5	4.3	2.0
Substrate	3.9	6x10 ⁵	3.9	6x10 ⁵	3.9	6x10 ⁵

However, unresolved issues remain; the relationship between the deposition process parameters and the amorphous as-deposited films should be explored. We have seen that the amount of VO₂ initially present in an as-deposited amorphous film does not guarantee the best quality film or correlate with stability; understanding the role of oxide composition is important. For PLD and sputtering, the relationship between process parameters such as pressure and particle energy has been observed to influence the properties of films. In the case of sputtering it would be useful to vary the substrate bias, thereby changing the ion energy to produce films with a range of densities. For PLD, increased pressure during deposition transitions from a plasma plume to a more particulate one, also influencing density. For all processes, varying the deposition rate could potentially be used a means to control the density and structure of the as deposited films.

4.6 Single Crystals: Introduction

Control of defects in solid-state materials, ranging from surfaces and grain boundaries to dopants and atomic vacancies, is the single greatest way to influence their physical, optical and electrical properties. Typically, single crystals provide improved transport properties but are more difficult to fabricate and often do not handle thermal strain without cracking. In contrast, thin films are generally easier to fabricate and handle thermal stress better, but have less favorable transport properties due to grain boundaries. Vanadium dioxide is a prime example of this: single crystals have a very large change in electrical conductivity (5

orders of magnitude[2]), but the fabrication methods are not compatible with most silicon-based processing and the large crystals crack after multiple phase-transition cycles. Thin films are easily deposited and can survive millions of transition cycles but typically only provide a 2-3 orders of magnitude change in resistivity.

Hydrothermal methods[125] have long been used to fabricate VO₂ crystals[1]. However, more recently vapor transport methods, as described by Guiton[126] have become popular. The exact process by which the vapor phase condenses and forms VO₂ crystals is still unknown. V₂O₅ is a common precursor for single crystal growth and several reports suggest that an intermediate V₂O₅ or V₆O₁₃ phase forms either before or in combination with VO₂[127]. Despite the structural continuity of single crystals, the phase transition has been observed to occur in a somewhat random fashion spatially, and is not reproducible[128]. Even though the crystals lack consistency, they provide a uniform crystal environment in which to study doping (see section 3.2) and transport.

4.7 Single Crystals: Fabrication

A vapor transport process has been used at Vanderbilt to produce a range of different VO₂ crystal sizes and shapes, as shown in Figure 4.8. V₂O₅ powder is placed in a two inch tube furnace upstream of the substrate. Argon gas flows at 20 sccm across the powder precursor and transports the vapor to the substrate. The growth occurs at 850 °C and 5 mTorr for 0.5 - 3 hours. After the growth is complete, the furnace cools to 100 °C (over the course of four hours) at which point the tube furnace is vented and the substrates are removed.

The substrate and surface roughness are critical factors and determine the crystal size, shape, growth orientation and density. On roughened quartz substrates, very high aspect ratio wires grow at a range of out-of-plane angles, producing a dense, intertwined carpet of wires. At the substrate edge, Figure 4.8a, very long wires are often found growing off the edge. On sapphire, Figure 4.8b, short kinked wires grow almost exclusively in-plane and

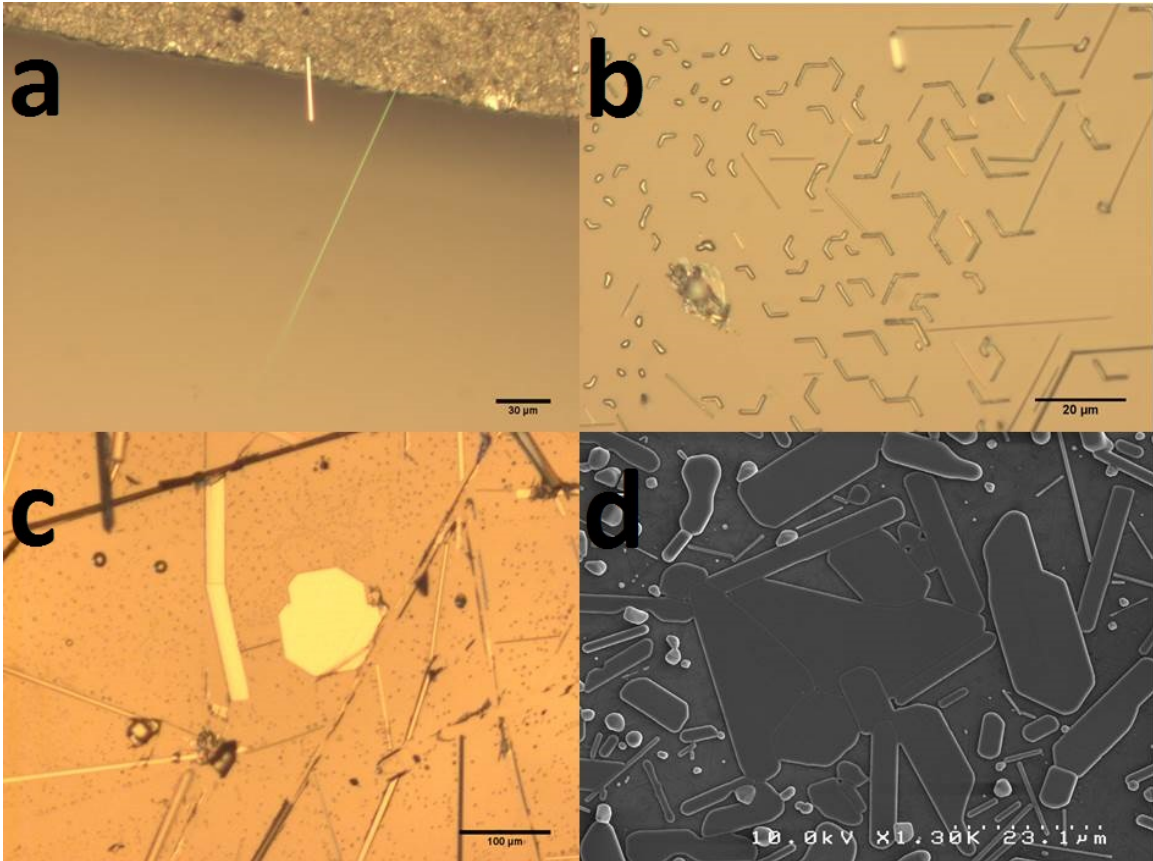


Figure 4.8: a) VO₂ high aspect ratio single crystal wire growing off the edge of a silicon substrate. b) Wires grown on sapphire exhibit the hexagonal symmetry of the substrate. c) Approximately 100 μm² single crystal grown on a quartz substrate. d) SEM image of low aspect ratio single crystal cluster on silicon.

follow the hexagonal structure of the substrate. On a polished quartz substrate, both high-aspect and low-aspect-ratio crystals are found, however, large (100 μm x 100 μm) crystals are rare (Figure 4.8c). On polished silicon substrates (with native oxide) the crystal size and shape distribution is quite varied and often crystals grow in clusters Figure 4.8d, with the highest concentrations found at the edge of the substrate.

Unlike vapor-liquid-solid (VLS) growth methods, which generally use patterned metal particles to catalyze and control crystal growth, the origins of VO₂ crystal nucleation are not known. Kim[127] was able to control the regions where crystals nucleated to some extent by patterning selected areas on a substrate with VO₂ and V₂O₅ powders by a sol-gel process (Figure 4.9). At Vanderbilt, attempts were made to use arrays of VO₂ nanoparticles,

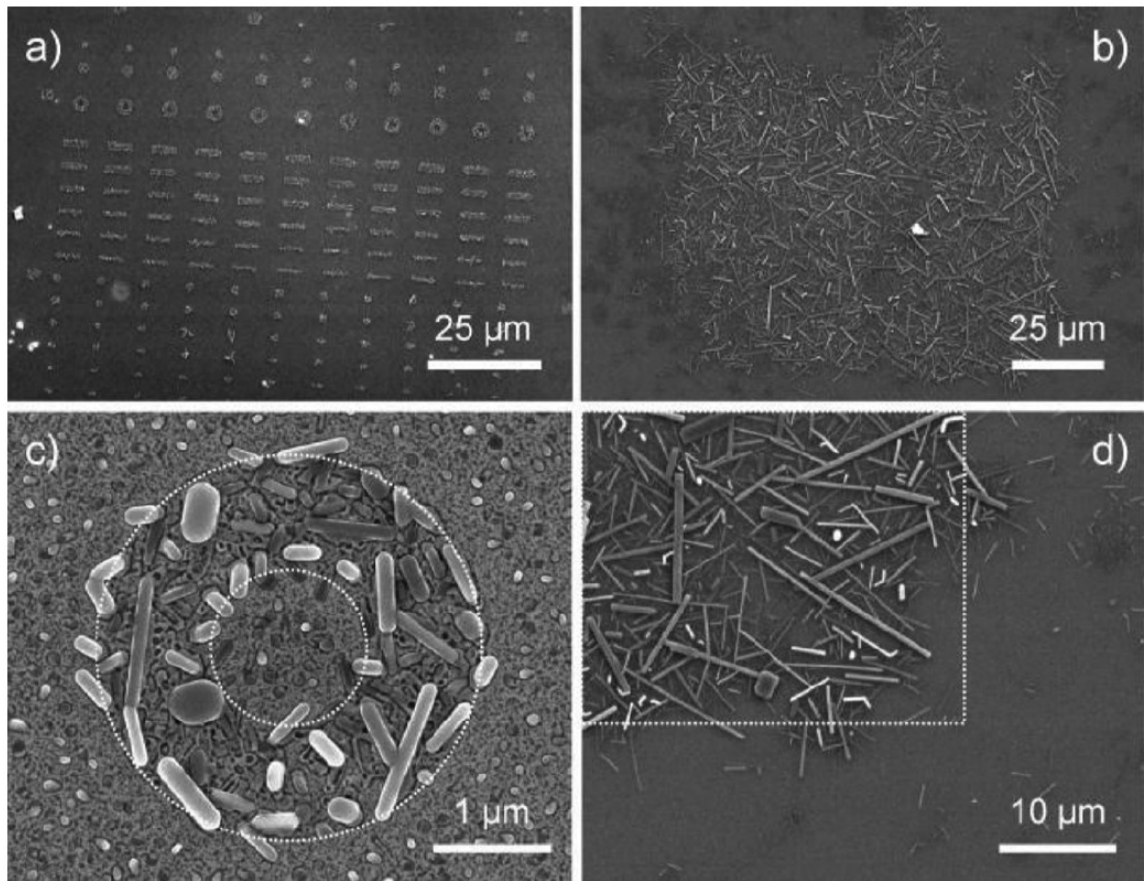


Figure 4.9: a,b) Preferential growth of VO_2 nanobeams on solgel derived VO_x patterns after growth for 3 min and 2 h, respectively. (c) Formation of VO_x nanoparticles upon annealing of solgel derived thin film (dashed lines are a guide to the eye indicating location of the VO_x pattern) prior to growth. (d) Higher magnification image of (b) taken at the bottom right corner. Image take from Kim[127].

patterned by EBL on silicon and sapphire substrates, as a template to catalyze and control crystal growth. None of these attempts was successful. Cheng[129] proposed a mechanism for growth on roughened quartz substrates, where VO_2 crystals grew out of V_2O_5 puddles located in the valleys of the roughened substrate. Initial growth proceeded upwards out of the “valley” along the surface and at longer times became free standing. In an attempt to test this mechanism on a different substrate, arrays of inverse pyramids were etched into silicon substrates using anisotropic silicon etchant (PSE 3000). Multiple growth attempts under different conditions showed no preference for the etched areas over the unetched.

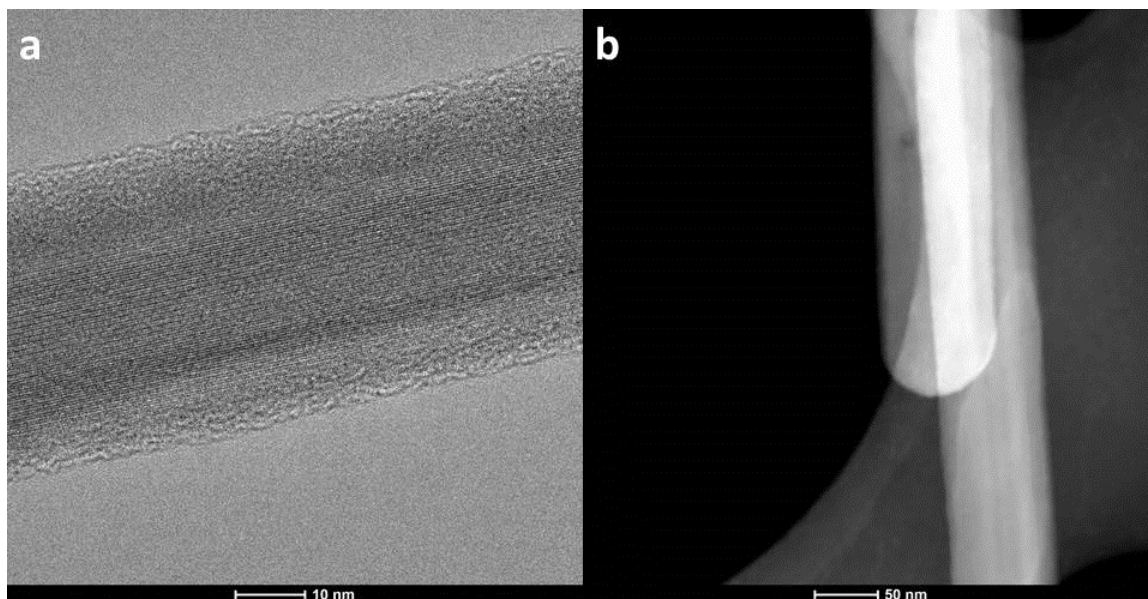


Figure 4.10: a) High resolution TEM image of VO₂ wire. b) HAADF image of VO₂ wire.

Table 4.7: Quantitative breakdown of elemental species observed in Figure 4.11.

Element	Weight %	Atomic %
Oxygen	24.87	50.64
Vanadium	70.43	45.08
Aluminum	1.78	2.15
Potassium	1.64	1.36
Iron	0.99	0.58
Calcium	0.26	0.21

TEM analysis of wires grown on roughened quartz revealed a well ordered lattice structure in the center with some amorphous material on the surface (Figure 4.10a). In Figure 4.10b, the rounded end of a wire is observed and is believed to be the top or “end” of the wire, the other end is attached to a clump of material, possibly part of the substrate. To determine if the top of the wire catalyzes the growth, energy-dispersive X-ray spectroscopy (EDS or EDX) measurements were conducted to determine the composition of the wire at this point. The results of the EDS mapping are presented in Figure 4.11. As expected, vanadium and oxygen are found uniformly across the wire along with potassium and aluminum, the origins of which are unknown. Interestingly, calcium and iron appear in small amounts at the tip of the wire.

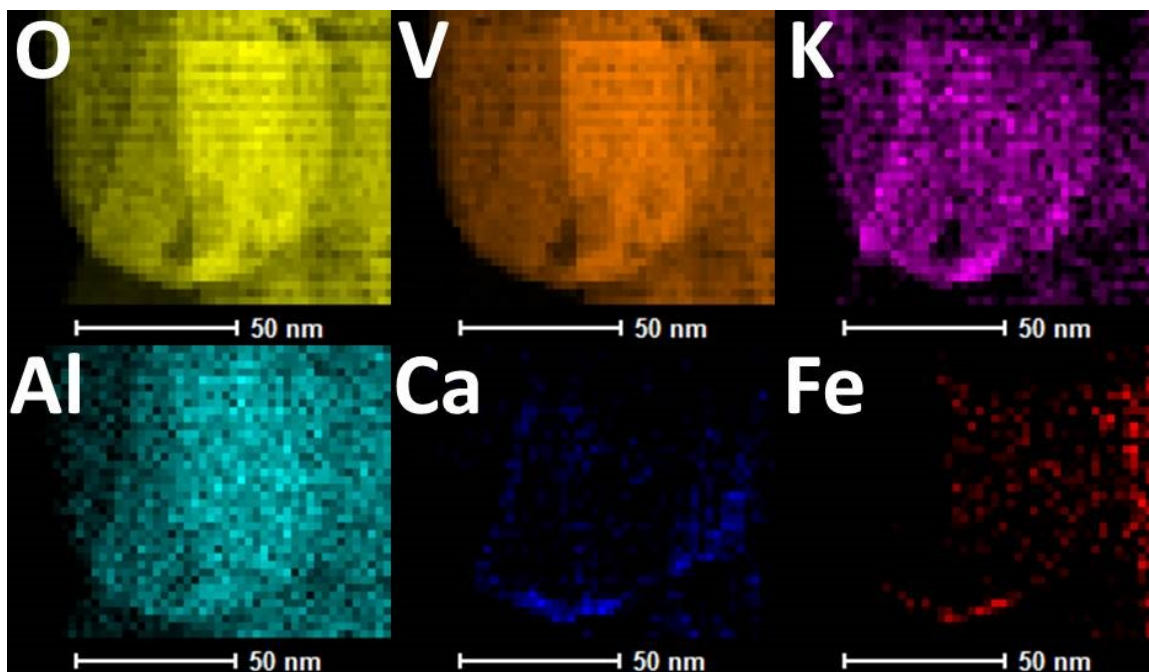


Figure 4.11: EDS images of the the rounded end of VO₂ wire pictured in Figure 4.10b. Letters in the upper left hand corner of each image indicate the elemental species being mapped.

To determine if calcium and iron are potential growth catalysts, batches of substrates were treated with calcium and iron. Powdered forms of each were sonicated in solvent (2-propanol) and then deposited on the growth substrates by spin coating. After allowing the solvent to dry a hazy layer was observed on the surface. Wire growths performed simultaneously with treated and untreated substrates did not show any difference between the substrates treated with calcium and iron and those without.

4.8 Conclusions: Single Crystals

To date, single crystals of VO₂ have been used exclusively for studying the fundamental properties and physics of VO₂ and have only a few applications[25]. Two factors have limited the development of single crystals for a wider range of applications. First, the fabrication process for high quality single crystals requires temperatures in excess of 800 °C[126]. Many dielectric materials and metals are not dimensionally stable at these high

temperatures. Single crystals must be removed from the growth substrate and placed on an existing device or onto a bare substrate in preparation for device fabrication. Second, very little control over the crystal size and nucleation has been demonstrated. In most cases a distribution of crystal sizes are produced and crystals of the desired dimensions must be removed selectively. The few attempts made to control crystal nucleation have only been able to produce crystals $\sim 1 \mu\text{m}$ in dimension, with random orientations but confined to the desired area. At the very least, the nucleation and crystal size needs to be controlled before single crystals can be practically used.

4.9 Conclusions: State of VO₂ Fabrication

In Figure 4.12, a few optical devices that incorporate VO₂ are presented which highlight some of the processing challenges that must be met. To successfully build multi-layer structures or devices in which VO₂ is deposited on metals the stability of each layer at $\sim 450^\circ\text{C}$ must be considered. In Figure 4.12a, a metamaterial with tunable dispersion is demonstrated by alternating layers of VO₂ and TiO₂. This structure is successfully produced because TiO₂ can be sputtered under the same conditions (450°C) as VO₂. A tunable emitter structure is shown in Figure 4.12b, however this has only been demonstrated theoretically. The issue with this and many other metamaterial structures involving VO₂ is the metal (gold). A highly reflective metal is often used as a back plane or element in many metamaterial designs, however, gold is not stable at the temperatures required to crystallize VO₂.

For many optical structures, having VO₂ everywhere will result in high loss. The terahertz switchable quarter-wave plate shown in Figure 4.12c uses photolithography to place micron scale patches of VO₂ at specific locations on the cross-shaped resonator. Patterning at the micron scale has been quite successful; however, nanoscale patterning has proven more difficult. Figure 4.12d presents a design for a metamaterial perfect absorber based on a 50 nm wide, 35 nm thick VO₂ patch (shown in red). Direct patterning of VO₂ patches

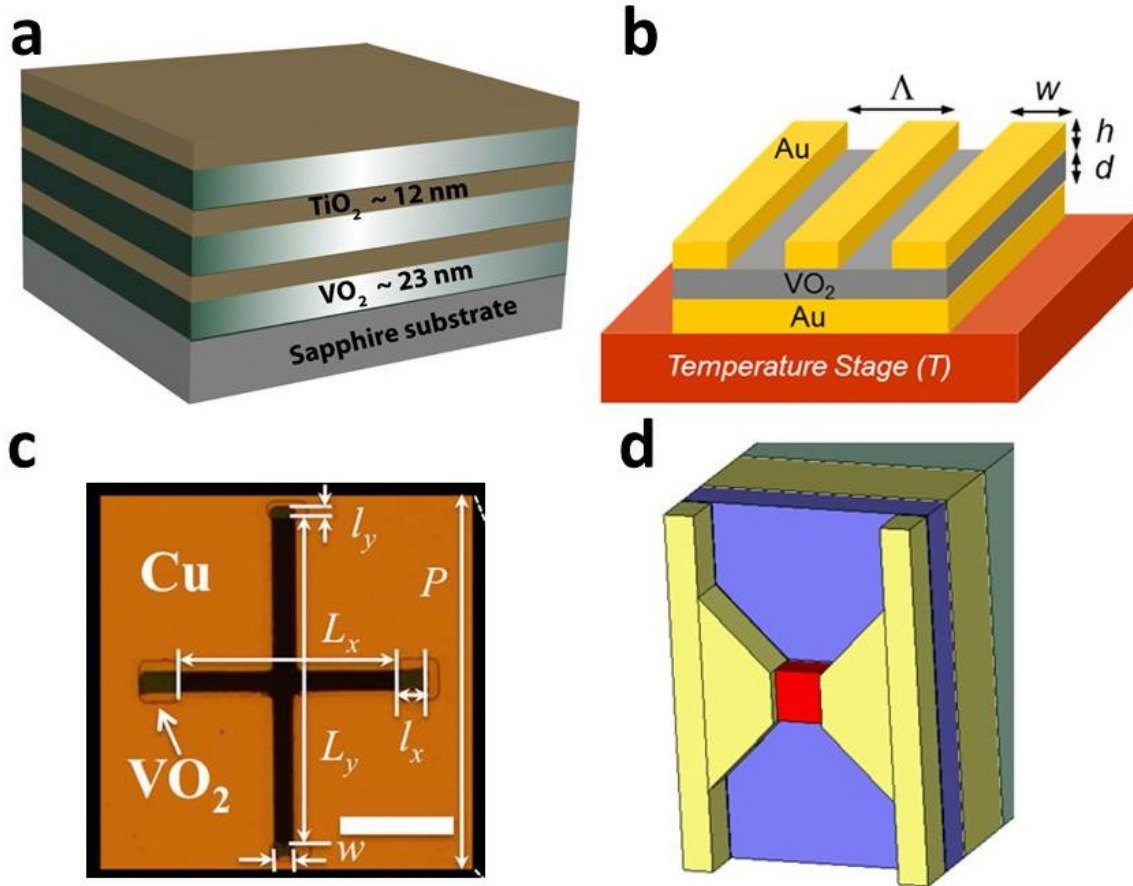


Figure 4.12: a) Tunable dispersion meta-material.[130] b) Tunable emitter.[131] c) Switchable quarter-wave plate.[132] d) Meta-material perfect absorber.[133]

has worked to some extent but etching would be preferable.

As outlined in this Chapter, a wide range of processes can be used to produce vanadium dioxide. In thin film form, large areas (m^2) can be coated by sol-gel processes and MBE can produce wafer scale switching films as thin as 2 nm. Single crystals can be produced with different shapes and dimensions up to millimeters, but with less control. The future challenges are not simply determining what synthesis methods produce the best VO_2 , but finding ways to incorporate VO_2 with other materials. Developing etch recipes and deposition methods that are compatible with other materials will allow VO_2 to serve as an active material for a wide range of uses. Process development with a strong focus on compatibility with other materials holds the key to future success in device fabrication of all kinds.

Chapter 5

The Non-equilibrium Metallic Response of VO₂

5.1 Introduction

A key part of any optical modulation device is the speed at which it can be reconfigured. Only recently was it confirmed that large changes in the VO₂ optical properties could be observed without triggering the structural phase transition, thereby avoiding the much slower structural recovery. In the first part of this Chapter, a brief history of the time resolved physics of vanadium dioxide is presented. The results from a research effort are summarized, demonstrating that the electronic transition occurs in less than 100 femtoseconds and is complete before the atoms begin to move. Also presented are data which examine the properties of the monoclinic-metallic state when excited with different wavelengths. Understanding the dynamics of the monoclinic metallic state is crucial for producing high-speed optical modulators.

5.2 Dynamics of Femtosecond Laser Pulse Excitation in Vanadium Dioxide

Most of the static phase-transition properties of VO₂ have been known since 1968. In 1971, the possibility of a optically induced fast phase transition was first suggested and demonstrated on nanosecond timescales by Roach[46]. A decade later in 1981 this work was extended to picosecond time scales[134]. The first femtosecond measurements were performed by Becker[135, 136] in 1994 and 1996. In 2001, Cavalleri[48] conducted the first experiments with sub-100 femtosecond resolution and definitively demonstrated that the phase transition occurs on sub-picosecond time scales. Cavalleri's work showed that it was possible for the optical, structural and electronic properties to change on femtosecond time scales, making high speed VO₂ based devices possible. This work also coincides with a significant increase in the citation rate as shown in Figure 1.1.

5.2.1 Contributions

In this section we discuss the time-resolved properties of vanadium dioxide and present two sets of experimental work which contribute to our understanding in the context of high speed optical switching applications. Results of time-resolved photoelectron spectroscopy (TR-PES) experiments performed with our collaborators are summarized; the full description can be found in *Physical Review Letters*[28]. In the second part, experiments performed at Oak Ridge National Laboratory are presented and a preliminary analysis is provided.

5.2.2 Introduction to Time Resolved Spectroscopy

Time-resolved spectroscopy provides information about electron dynamics in atoms, molecules and nanostructures and atomic dynamics in molecules and solids[137], as shown in Figure 5.1. The importance of this information can not be overstated, as the behavior of electrons is at the root of all phenomena in physics, chemistry and biology. Understanding the behavior of electrons requires development and implementation of experimental techniques which can resolve behavior with characteristic times ranging from a few hundred femtoseconds (10^{-13} s) to less than 1 attosecond (10^{-18} s). Optical pump-probe techniques using pulses shorter than electron-lattice relaxation times are the only way to achieve the high temporal resolution required to study these phenomena.

Ultrafast science has brought about significant advances in chemistry and biology, allowing researchers to observe intermediate states in chemical reactions and understand how electronic energy is redistributed into atomic and molecular motion[138, 139]. In condensed matter, absorption of an ultrafast laser pulse by optical phonons can lead to understanding of how electronic excitations relax and transfer energy to the atomic lattice[140]. In many condensed matter systems, coherent acoustic phonons can be launched by an intense laser pulse, and then used to probe thermal transport, electron behavior and lattice

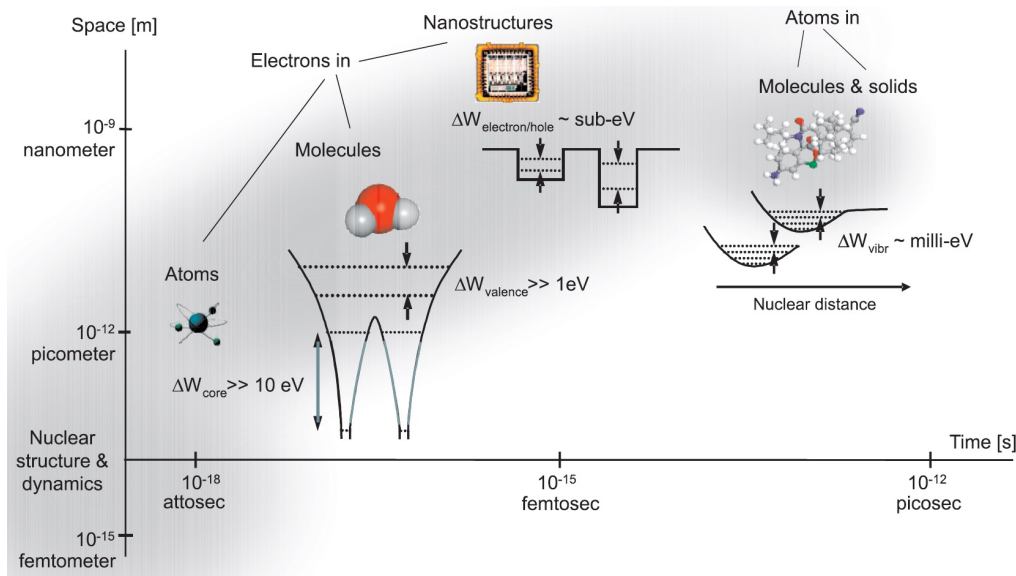


Figure 5.1: Length and time scales for electronic and atomic dynamics. Figure taken from [137].

elasticity [141, 142]. More recently, ultrafast optical excitation has been combined with electron and x-ray sources to allow for direct measurements of structural properties with femtosecond time resolution.

The basic concept of a pump-probe experiment (known also as ultrafast laser spectroscopy) is quite simple, however the implementation and interpretation of results can be much more complicated. In the simplest case, a single pulse from a coherent light source (laser) is divided by a beam splitter into two. Each pulse then travels a different distance before encountering a sample. If the optical path length (OPL) traveled by each of the pulses is the same, both will reach the sample at the same time. If the OPL is varied so that one pulse travels three μm more, the difference in arrival time between the two pulses will be one femtosecond. In most cases the two optical pulses have very different fluences (mJ/cm^2), the pump typically has a fluence 10-100 times greater than the probe. The higher fluence is used to pump (excite or initiate) dynamics in the sample while the lower-energy pulse probes the pump-induced dynamics, ideally without contributing to the sample response. By careful choice of pump and probe parameters and controlled variation of the

OPL for one pulse, electronic and lattice dynamics can be initiated and monitored with very high temporal resolution.

Many variations on this technique exist. In the simplest case, the pump and probe pulses are the same wavelength (degenerate pump-probe), but much more exotic combinations exist. By tuning the wavelength and species (photons or electrons) different physical characteristics can be directly measured. Higher energy photons (or x-rays) probe core-shell electrons or can be used for atomic diffraction while infrared radiation can be used to directly excite lattice vibrations. In addition to probing specific phenomena, intense radiation produces highly non-equilibrium conditions in materials and can result in unique phases.

These experiments can be carried out on a single optical bench, or require an entire facility, such as a synchrotron light source or an X-ray free-electron laser. In Table 5.1 some variations are listed along with their contributions to our understanding of dynamics in VO₂.

The first report of an optically induced “fast” phase transition (in VO₂) was published in 1971 and demonstrated that the phase transition occurred within 20 nanoseconds and was the result of a photon → electron → phonon energy transfer process[46]. Almost 10 years later, Bugaev[134] and coauthors confirmed that the transition occurred in less than a picosecond, too fast for their setup to resolve. In 2001 Andrea Cavalleri[48] used an optical pump x-ray probe experiment to show that the VO₂ lattice moved on a time scale of less than a picosecond and was therefore not a thermal process. In an attempt to understand the driving force behind the phase transition and determine precisely how fast the transition occurred, Cavalleri[143] performed optical-pump/optical-probe measurements with 15 fs time resolution and varied the pulse duration. Figure 5.2 presents the most important result of this experiment, evidence of a structural bottleneck. As the pulse duration is decreased, the transition time decreases down to 80 fs, at which point no further reduction in transition time is observed. The 80 fs limit corresponds to approximately one half cycle of the

Table 5.1: Pump-probe techniques and ultrafast VO₂ dynamics.

Pump	Probe	Contribution to VO ₂
Optical (800 nm)	Optical (800 nm)	First experiment indicating high-speed phase transition and evidence of phonon bottle neck[143].
Optical (1-20 μm)	Optical (800 nm)	Below gap excitation can trigger transition.[144]
Optical (800 nm)	Broadband (520-690 nm)	Provide simultaneous information about electronic state (400 nm) and lattice (800 nm)[38].
Optical-Optical (800 nm)	Broadband (520-690 nm)	Excited state VO ₂ is probed in pump-pump-probe technique[38].
Optical (800 nm)	THz (12-30μm)	Coherent V-V atom oscillation is important[47].
Optical (800 nm)	X-ray (Diffraction)	Sub-picosecond structural transition[48].
Optical (800 nm)	X-ray (Attosecond Pulse)	Changes in the vanadium 3p core level spectrum are observed.[145]
Optical (800 nm)	Electron (Diffraction)	Optical signatures of the metallic state are observed while the monoclinic structure is present[29].
Optical (800 nm)	X-ray (PES)	Instantaneous band gap collapse due to photoexcitation.[28]

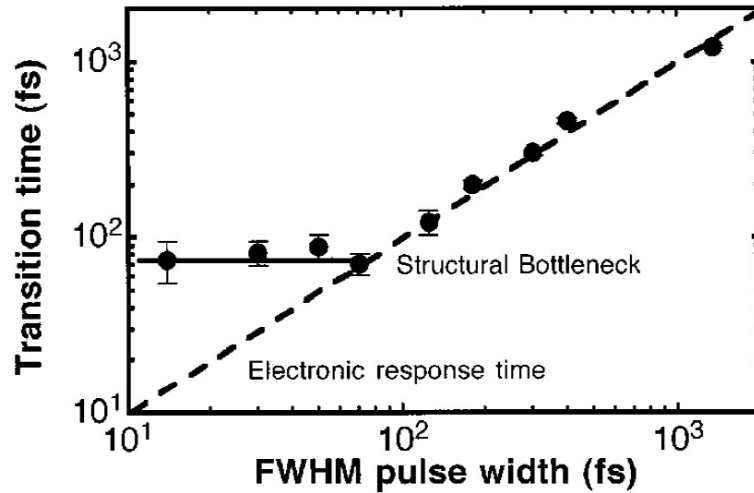


Figure 5.2: Phase transition time for different pulse durations. Figure taken from [143].

dominant coherent phonon modes, indicating that the rutile structure is necessary for the electronic portion of the phase transition to be completed. This work added support to the Peierls theory of the VO_2 phase transition and set a lower limit for the phase transition speed. These conclusions were not conclusively disproved for another ten years.

Despite the sub-100 femtosecond transition time, using VO_2 as an active element in electronic and photonic switching applications has not been practical due to slow recovery time from the rutile state, on the order of 10 ps - 10 ns depending on substrate and excitation. The work of Wen [20] demonstrates this problem well and is summarized in Figure 5.3. They studied the relaxation dynamics for a thin VO_2 film pumped at 800 nm and probed optically at 800 nm and structurally with x-rays. This allows the structural and electronic excited state decay to be directly measured and compared. The points (dotted line) and scale on the left show the change in lattice parameter, calculated from the shift in diffraction angle for the (400) peak. From 0-2 ns, the lattice is still changing rapidly and after 7 ps the recovery is flat but still not back to the original value. The changes in optical density track well with changes in the lattice and increasing the fluence increases both the modulation depth and the recovery time. Clearly, exciting VO_2 with sufficient fluence to complete the structural phase transition results in a very long decay time and is

not a successful strategy for high-speed device operation.

Excitation with laser fluence below that required to fully complete the phase transition results in a large modulation of the electronic structure and vibration of the atomic lattice around the monoclinic coordinates. It is this fluence regime, with large electronic modulation and moderate atomic vibration, where VO₂ may function as a ultrafast switch. This is the so-called “monoclinic metallic state” of VO₂, and understanding the dynamics of this state will determine the suitability for high speed switching applications.

One of the first experimental reports suggesting that the structural and electronic parts of the phase transition are distinct for thermal excitation and that the structural transition may not be a prerequisite for the electronic transition, was published in 2012[50]. In this work, the hysteresis parameters extracted from temperature-resolved x-ray diffraction measurements are compared to those from optical measurements. The structural phase transition (temperature-resolved XRD) was found to have a hysteresis approximately 2.5 times wider than the electronic transition (optical measurements), demonstrating the non-congruence and indicating the possible existence of a “monoclinic metallic state”. In 2014, similar disagreement between the electronic and structural transition temperature scales was reported by Laverock[30] who used low energy electron microscopy (LEEM) and low energy electron diffraction (LEED) to measure the electronic and structural behavior at different temperatures.

Two groups published reports in late 2014 demonstrating the non-congruence of the SMT and SPT. In one report[28], in which Vanderbilt was a collaborator, an optical pump was combined with a photoelectron probe, showing with femtosecond resolution the instantaneous collapse of the monoclinic band gap. This work is described in detail in section 5.3 of this Chapter. The 80-fs bottleneck reported by Cavalleri[143] is not observed and the bandgap collapses on a time scale much too fast for atomic motion. In the second report[29], a more direct method, time-resolved electron diffraction, confirms that all the signatures of the electronic transition are observed while the monoclinic atomic structure is

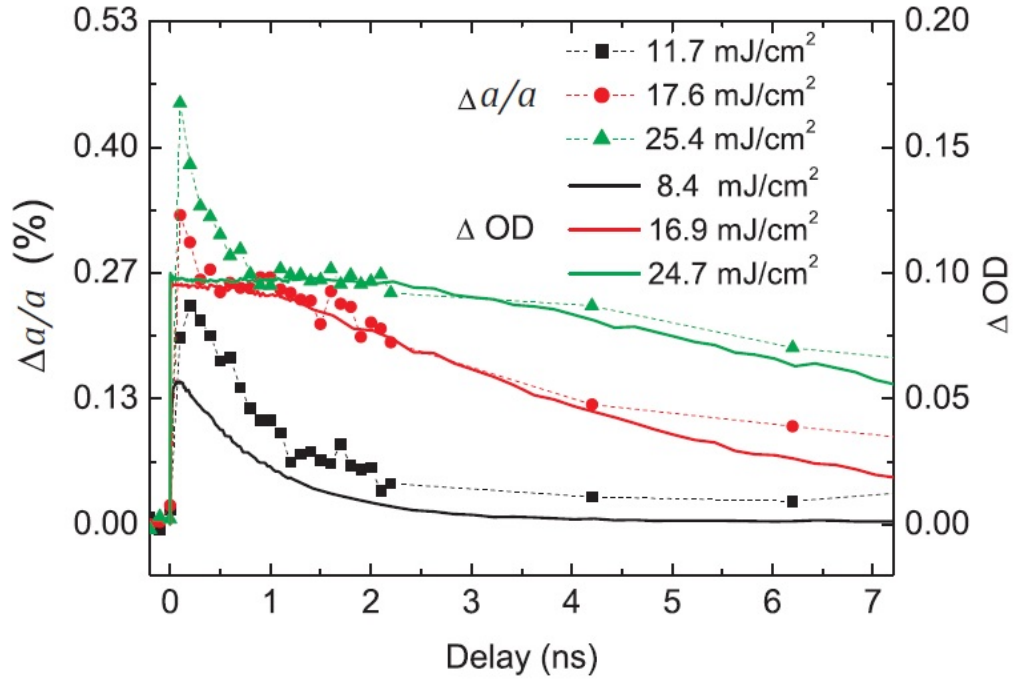


Figure 5.3: The changes in lattice constant($\Delta a/a$) and optical density(ΔOD) are plotted as a function of pump-probe delay for varying pump fluence. Figure taken from[20].

still present. The relevant results of this work are presented in Figure 5.4. The Figure inset shows changes in the optical transmission for three different fluences across 3 ps of delay. At 3.7 mJ/cm^2 the transmission saturates, indicating that optically the film is completely metallic. In the main part of the Figure, the $(30\bar{2})$ and (220) diffraction peak intensities are plotted. The $(30\bar{2})$ intensity is directly related to the vanadium atom dimerization and is a good indicator for the structural phase transition. The (220) diffraction peak is not expected to change abruptly during the phase transition. Examining the electron diffraction intensity, it is clear that up to 7 mJ/cm^2 , there is little or no change in the $(30\bar{2})$ diffraction peak intensity. At nearly twice the pump fluence required to saturate the optical response (electronic transition), there is still no indication that the atomic structure has changed. This clearly demonstrates that all of the optical, and by extension electrical, properties of metallic VO_2 can be obtained without the structure changing.

It is clear that high speed electronic and photonic devices need to operate in a region

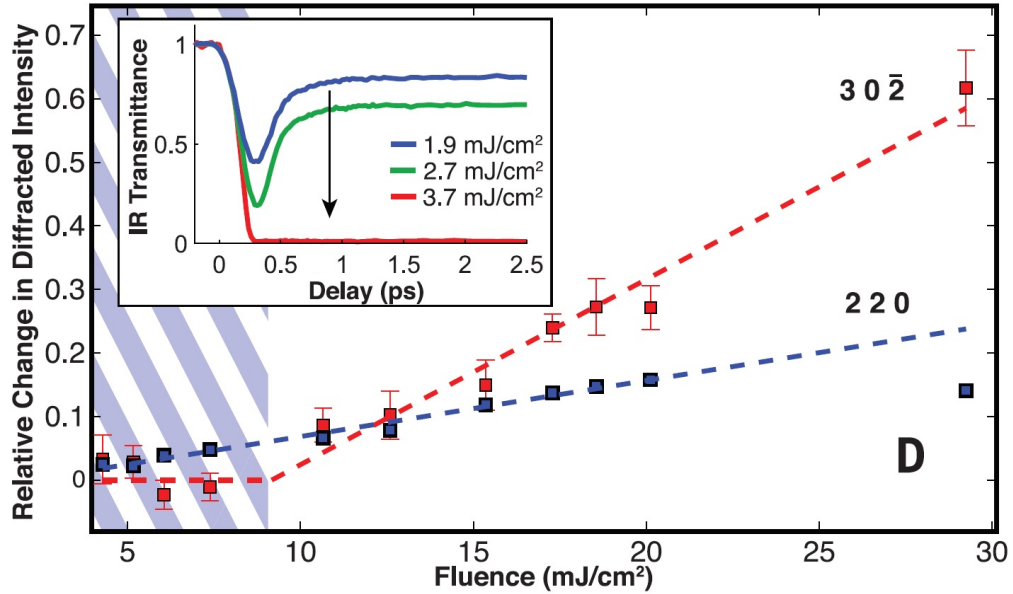


Figure 5.4: Changes in the optical transmission at $5 \mu\text{m}$ (inset) are plotted for different fluences and as a function of delay. The main graph shows changes in the $(30\bar{2})$ and (220) diffraction peak intensity for different pump fluence values. Figure taken from [29].

where the excitation fluence is just below that required to complete the phase transition. Detailed studies of VO_2 dynamics at fluences lower than required to initiate the structural phase transition (7 mJ/cm^2) occurred several years before the existence of the monoclinic metal phase was confirmed [47, 38, 146]. In optical pump THz probe experiments, Kubler [47] excited electron-hole pairs with 12-fs 1.55 eV pulses and probed the response with broadband THz radiation (40-100 meV). At low fluences, the lattice dynamics are consistent with coherent stretching vibrations of the V-V dimers. At moderate fluences, the strong correlation between binding electrons on the V-V dimers is temporally disturbed, allowing a short-lived increase ($<1 \text{ ps}$) in the mid-infrared conductivity. At fluences above 7 mJ/cm^2 , the mid-infrared conductivity saturates at the steady-state value after approximately one V-V oscillation cycle (170 fs). The electronic transition is complete, but the lattice continues to evolve for much longer.

The most comprehensive study of below-threshold dynamics was published in a pair of papers by Wall [38, 146]. By exciting thin films with 40 fs 800 nm light and probing

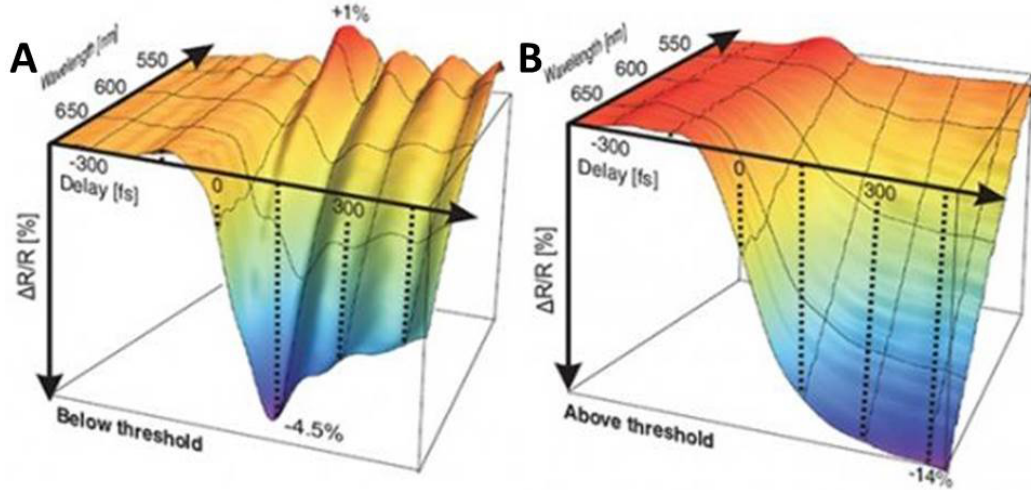


Figure 5.5: Response of VO₂ films in white light pump-probe experiment A) below phase transition fluence and B) above fluence[38].

with a broadband (520-700 nm) 20 fs probe, oscillations in reflectivity, due to coherent phonons, are observed across the probe wavelength range as in Figure 5.5. The dynamics below the phase transition fluence threshold (F_{TH}) are shown in Figure 5.5a and above are presented in Figure 5.5b. The most striking difference between the spectra are the oscillations observed below F_{TH} , which are attributed to the four strongest monoclinic structure phonon modes, at 5.67, 6.7, 4.3 and 10 THz.

Examination of single-wavelength traces at 525 nm reveals that the oscillations are most pronounced at $0.7 F_{TH}$, Figure 5.6a. After subtracting a double-exponential background from the data, periodic oscillations are clearly observed at 525 nm with decaying amplitude, Figure 5.6b. In contrast, the oscillations are very weak at 800 nm (Figure 5.6b upper plot). The solid red line in each plot is a two-component fit to the data, assuming modes at 5.67 and 6.7 THz dominate. These two modes are of A_g symmetry, involve vibrations of the vanadium and oxygen atoms and are the most prominent in Raman scattering measurements. After subtracting the two-mode fit from the data, frequency domain analysis of the residual [Figure 5.6b(inset)] indicates that lower amplitude modes at 4.3 and 10 THz are also present.

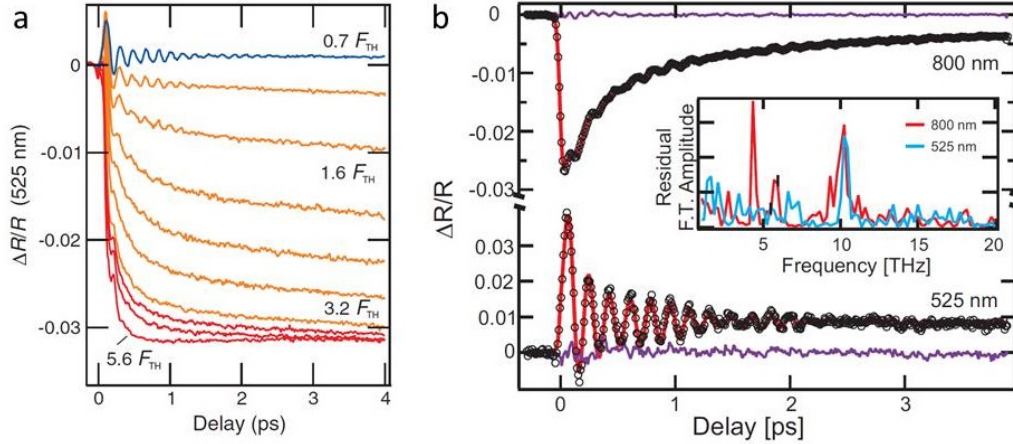


Figure 5.6: a) Change in reflectivity for a VO₂ film at 525 nm excited at different fluences. b) Below F_{Th} behavior at 800 nm and 525 nm, inset shows Fourier transform of experimental data. Figure taken from[146].

The mechanism responsible for producing coherent phonon oscillations VO₂, known as displacive excitation of coherent phonons (DECP), has been observed in many other materials and was formally proposed by Zeiger[140] in 1992. The basic concept behind DECP is that the relaxation dynamics of carriers excited above the bandgap instantaneously shifts the lattice potential energy surface (PES) and therefore the equilibrium positions of the nuclei, producing coherent vibrations in the lattice. Only materials with A₁ vibration modes, which are singly degenerate, can be visualized as breathing modes and do not lower the lattice symmetry, can be excited coherently by DECP. Since the breathing modes are symmetric, the lattice (and mode) symmetry is not disturbed by their excitation and a continuous range of displacements is available. Non-symmetric and multiply degenerate modes distort the lattice symmetry by definition and can not be produced coherently.

5.3 Introduction: Time-Resolved Photoelectron Spectroscopy

In contrast to optical measurements, time-resolved photoelectron spectroscopy (TR-PES) directly monitors changes to the electronic structure without sacrificing high temporal resolution. In optical measurements, the response is primarily due to changes in the

dielectric function while modification to the underlying electronic structure of the material is not observed. By using TR-PES, changes in the density of states around the Fermi energy, which define the conductivity of a material, can be directly monitored and isolated from changes in the dielectric function, without sacrificing high temporal resolution. Time-resolved photoelectron spectroscopy was performed previously on vanadium dioxide, however the temporal resolution (>150 fs) was not high enough to resolve the dynamics of the electronic phase transition[147].

5.3.1 Experiment

A 45 nm VO_2 film grown on c-sapphire (0001) by pulsed laser deposition at Vanderbilt, as described in Chapter 4.2, was used for these experiments. Ultrafast dynamics were initiated by a 800 nm (1.55 eV) pump pulse and 200 nm (6.19 eV) probe pulses generated photoelectrons. The poor thermal conductivity of the UHV environment necessitates using pump fluences below 7 mJ/cm^2 , allowing the sample to cool between pulses. A hemispherical electron energy analyzer is used to collect electrons and the spectra are plotted as a function of energy with respect to the equilibrium Fermi level of the sample.

5.3.2 Results and Discussion

The change in intensity across the photoelectron spectrum is plotted in Figure 5.7 for the thermally induced phase transition; spectra are presented for increasing temperature on the left and decreasing on the right. The changes in spectral intensity around the Fermi energy (E_F) exhibit hysteretic behavior as shown in the center Figure. The difference between the monoclinic and rutile photoelectron spectra (shown in Figure 5.7) is plotted in Figure 5.8(b) (green). When compared to the Fermi-Dirac distribution (black curve), there is excellent agreement between the data and model. In Figure 5.8(a), the photoelectron spectra before arrival of the pump (blue) and after (red) are shown. The change in photoelectron spectra across the optically induced phase transition at these fluence levels is expected to be on the

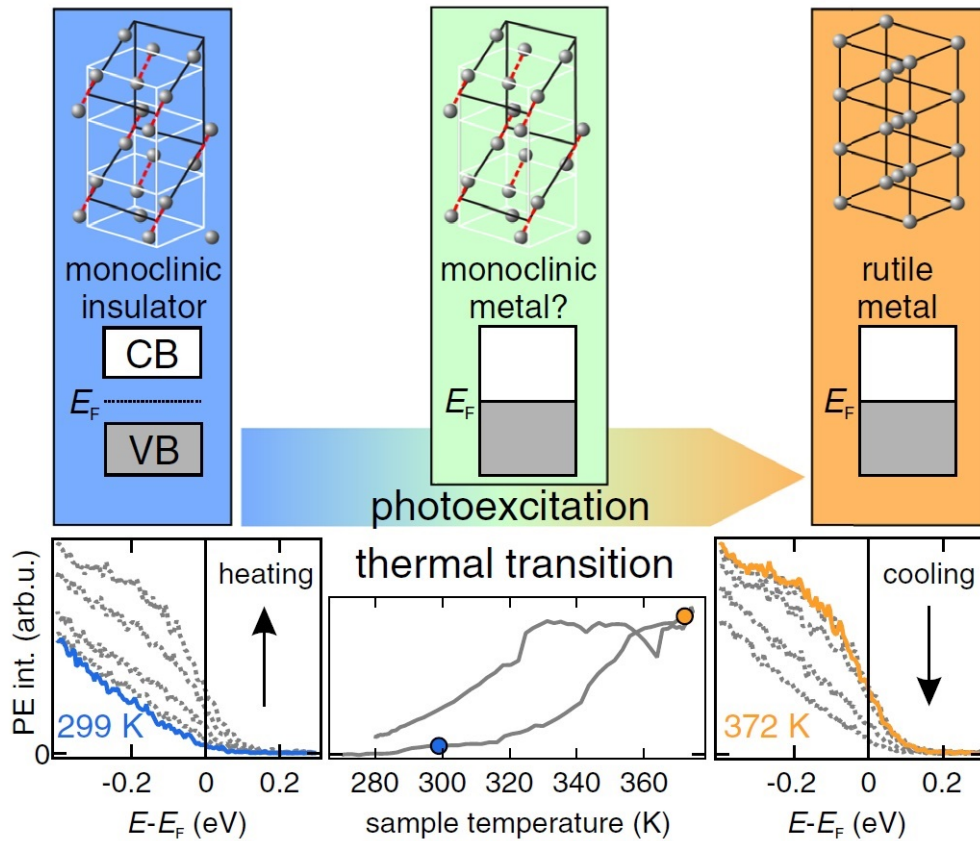


Figure 5.7: Top: schematic of the atomic and electronic structure evolution in vanadium dioxide during the photoinduced phase transition. Bottom left and right: change in photoelectron spectrum when heating (left) and cooling (right). Integrated PE intensity ($0.2 \text{ eV} < E-E_F < 0.0 \text{ eV}$) shows hysteretic behavior (center)[28].

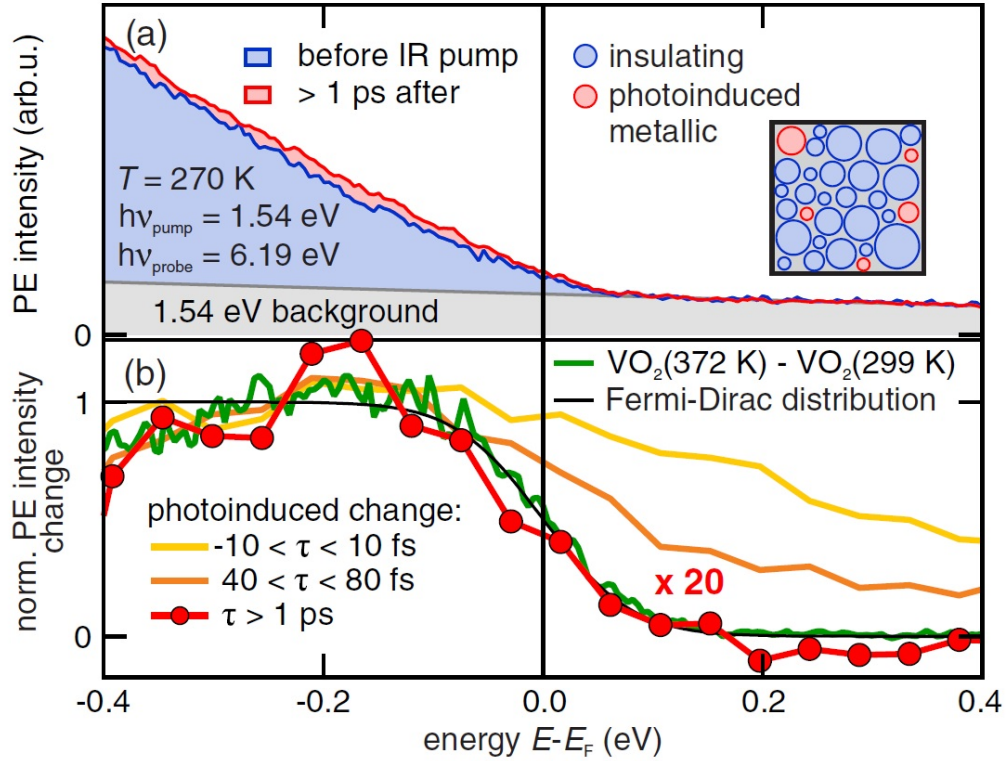


Figure 5.8: (a) Photoelectron spectra before (blue) and 1 ps after pumping (red, $6.7 \text{ mJ}=\text{cm}^2$). Inset: schematic showing of partial phase transition and film domain structure. (b) Thermally induced changes (green) and photoinduced changes (yellow, orange, red)[28].

order of 1-10% of what is observed in thermal measurements[148, 48, 38]. Because the pump pulse fluence is not high enough to make the entire film switch (see inset of Figure 5.8(a)), scattered metallic domains exist in a sea of insulating grains, resulting in a much lower signal. Low pump fluence is required to insure that the film has recovered the initial state before the next pump pulse arrives.

The photoinduced change in photoelectron spectra is shown by the red curve in Figure 5.8(b) and multiplied by 20 to account for the much lower signal. The shape of the photoinduced curve agrees well with the thermally induced transition and with the Fermi-Dirac distribution, demonstrating that the Fermi edge can be directly observed. By directly observing the Fermi edge (which is a signature of metallicity), contributions from excited states in the valence and conduction bands can be ruled out. In addition, any changes in

the dielectric function due to the structural transition are also eliminated. Optical probes are only able to detect changes in the dielectric function, which can result from all of these phenomena.

In Figure 5.9, the time resolved dynamics of the photoinduced electronic PT are presented. Optically induced changes in the PE energy spectrum are shown as a function of pump-probe delay, Figure 5.9(a). Cross sections of the dynamics are presented in Figure 5.9b, where dynamics above E_F are shown in purple and those below in green. Dynamics above the Fermi level are mainly due to excited electrons and have a faster decay time ($\tau_e = 160$ femtoseconds) while energies below the Fermi level probe the behavior of holes and have a longer decay time ($\tau_h = 210$ femtoseconds). As mentioned above, optical experiments are only sensitive to changes in the dielectric function, dominated by behavior above E_F , while changes below E_F are a good indicator of the metallic phase via changes in the Fermi-Dirac distribution. The behavior below E_F has stabilized after 1 ps and is observed not to change for 400 ps. The constant nature of this behavior indicates that the underlying atomic motion does not affect the Fermi-Dirac distribution and that the band gap collapses in less than 1 ps. If the electronic structure were still evolving after 1 ps, changes in the below band gap signal would be observed.

The photoelectron intensity in the gap changes nearly instantaneously after photoexcitation as shown in Figure 5.9b. A delayed rise, with a time scale of 80 fs, as expected for a structural bottleneck[143], is not observed in the intensity below E_F . Theoretical calculations indicate that a redistribution of the electron and hole populations in the valence band (VB) and conduction band (CB) can lead to a collapse of the band gap. This is in contrast to most semiconductors where free-carrier excitation leads to minimal narrowing of the bandgap[149, 150, 151, 152, 153] and do not produce a complete band gap collapse[153]. The high sensitivity of VO_2 to changes in the population of the V 3d states is a hallmark of strongly correlated materials[154].

A schematic representation of the processes involved is presented in the inset of Fig.

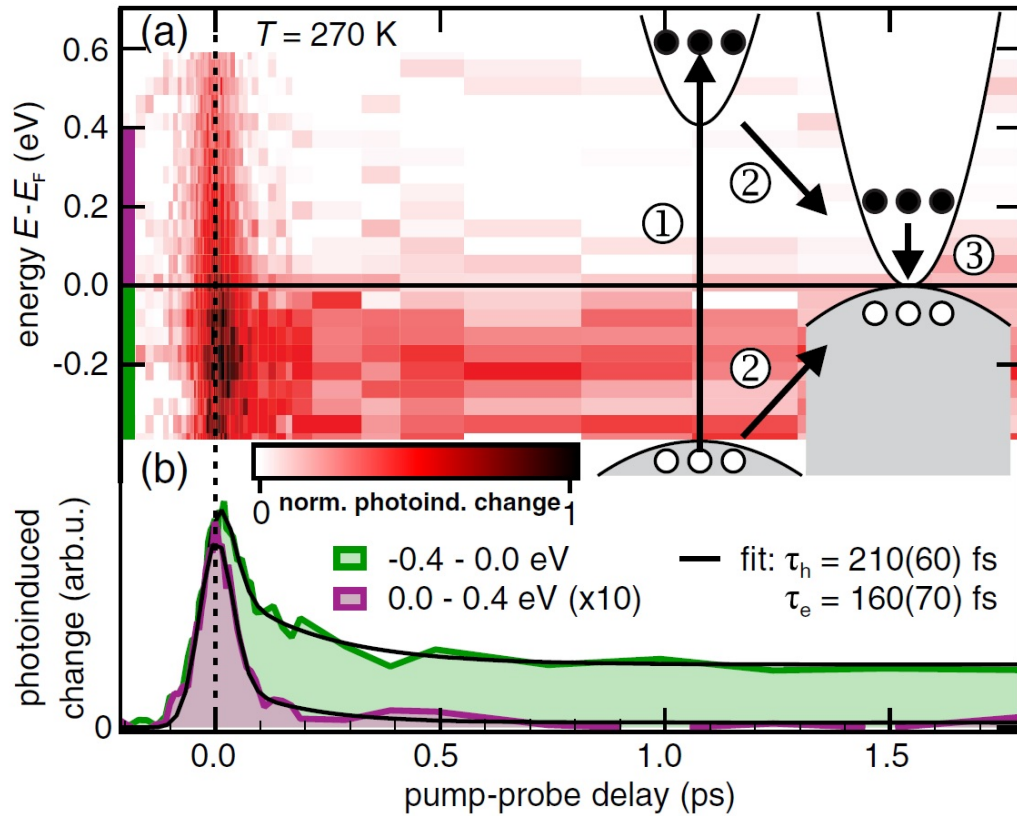


Figure 5.9: (a) PE intensity change versus pump-probe delay close to E_F . Photoelectrons are detected immediately in the gap, showing the quasi-instantaneous collapse (cartoon energy axis is to scale). Integration of the PE intensity above (purple) and below (green) E_F yields the respective transients in (b). The empirical fit (black) quantifies the averaged hot electron(hole) lifetimes[28].

5.9(a). Absorbed pump photons excite localized electrons from the top VB into the CB of insulating VO₂. This electron doping causes an instantaneous breakdown of the gap and subsequent relaxations of excited electrons and holes towards equilibrium at E_F. Photoexcitation in vanadium dioxide produces an excited metallic state, which after hot carrier relaxation, has optical and electrical properties similar to the thermally driven material but without the slow relaxation from the rutile crystalline phase.

5.3.3 Conclusion: PES

Time-resolved photoelectron spectroscopy has provided a description of the fundamental processes involved in the photoinduced electronic PT in VO₂ by combining experiment and theory. By separating the response of free carriers from that of the underlying electronic structure, we observed the instantaneous collapse of the bandgap under photoexcitation and the sensitivity of VO₂ to changes in valence band is highlighted. The band gap collapses in under 80 fs, proving the absence of a structural bottleneck and demonstrating that the electronic transition is complete before the atoms begin to move.

5.4 Coherent Phonon Generation

As discussed above, it is not desirable to complete the full structural phase transition in high-speed switching applications. In the previous section we have demonstrated that changes in the electronic properties across the phase transition occur before the atoms have begun to move. It is clear that investigating the properties of excited VO₂ in the fluence regime below that required to drive the full structural phase transition is important. In the following sections we examine the behavior of excited monoclinic VO₂ using variable wavelength pump pulses and white light probe.

5.4.1 Experiment

A 100 nm thick VO₂ film was deposited on glass substrates by rf-sputtering as described in section 4.2. Temperature resolved white-light absorption spectroscopy confirmed the transition temperature and hysteresis under equilibrium conditions. In Figure 5.10 the experimental setup used for time resolved spectroscopy is drawn schematically. Femtosecond pulses with ~40 fs duration are produced at 1 kHz by a regeneratively amplified titanium:sapphire (Ti:Sa) laser. For all measurements, approximately 4% of the pulse power is directed towards a sapphire plate for white-light continuum generation (probe). Sufficient intensity is generated from 350 nm to 1100 nm with a band from 750-850 nm lost due to a filter required to remove the fundamental wavelength (~ 800 nm). Probe absorption is measured by a fiber coupled spectrometer and recorded in reference to the probe intensity for a pulse without pump, as given by Equation 5.1.

$$Absorption = -\log \frac{(IntensityProbe)_{withpump}}{(IntensityProbe)_{withoutpump}} \quad (5.1)$$

The nominal pulse duration is ~40 fs (as measured by auto-correlation) for the 800 nm fundamental pulse when it exits the amplifier. The white-light probe pulse duration is reasonably estimated to be ~100 fs but has not been directly measured. 400 nm pump pulses are produced by second harmonic generation (SHG) in a beta barium borate (BBO) crystal. Pump pulses at 800 nm come directly from the amplifier while 1200, 1400 and 1500 nm pump pulses are generated by an optical parametric amplifier (OPA). According to the laser manufacturer (Coherent) the probe pulse duration for wavelengths other than the fundamental is 1.0-1.5 times the fundamental duration.

5.4.2 Results and Discussion

In Figure 5.11 the raw absorption data for these experiments are presented. For all cases, oscillations in the absorption amplitude occur as a function of delay time. The

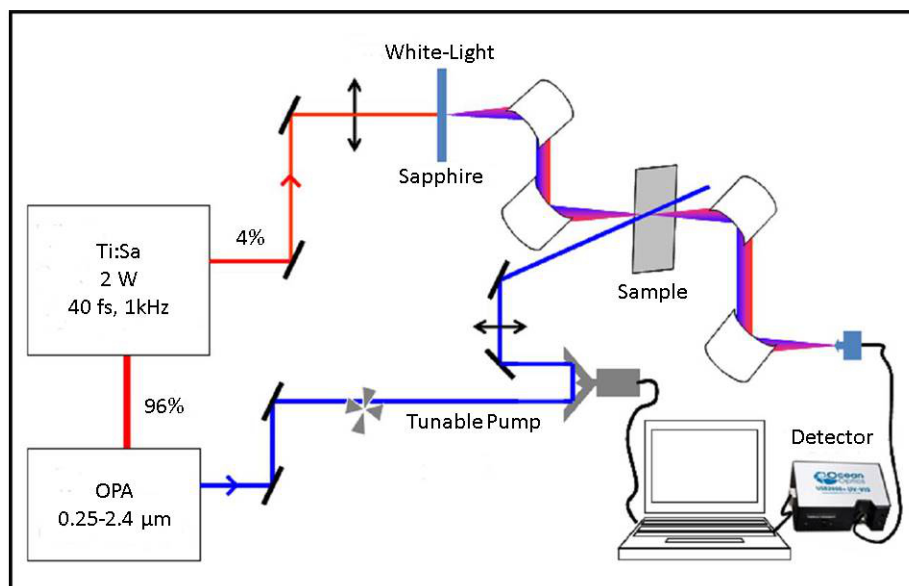


Figure 5.10: Schematic representation of the OPA pump white-light probe system at the Center for Nanophase Materials Science, Oak Ridge National Laboratory (courtesy of Aziz Boulesbaa)

oscillations are most clearly defined when pumping at 800 nm, likely the result of a shorter and more uniform pulse profile. The curvature in the data, which appears to suggest that dynamics at 450 nm occur before those at 750 nm, is the result of chirp induced in the data from dispersion in the optical components of the system. The system chirp has been characterized by performing the same set of experiments on a glass substrate, which shows a large spike in absorption, due to the “coherent artifact”, only when the pump and probe pulses overlap in space and time. All additional analysis is done on data which have been corrected to account for the system chirp.

To analyze the experimental data presented in Figure 5.11, we employ a slightly different approach than used previously by Wall[38]. The coherent oscillations are extracted at each wavelength from the absorption spectra by first subtracting out a double exponential background from the raw data. The two parts of this exponential represent the energy exchange between the excited electrons (~ 200 -300 femtoseconds) and the fast thermal relaxation and energy transfer from the excited electrons to the lattice (~ 1 picosecond and longer). In Figure 5.12a, the raw data are presented and in 5.12b, the double exponential

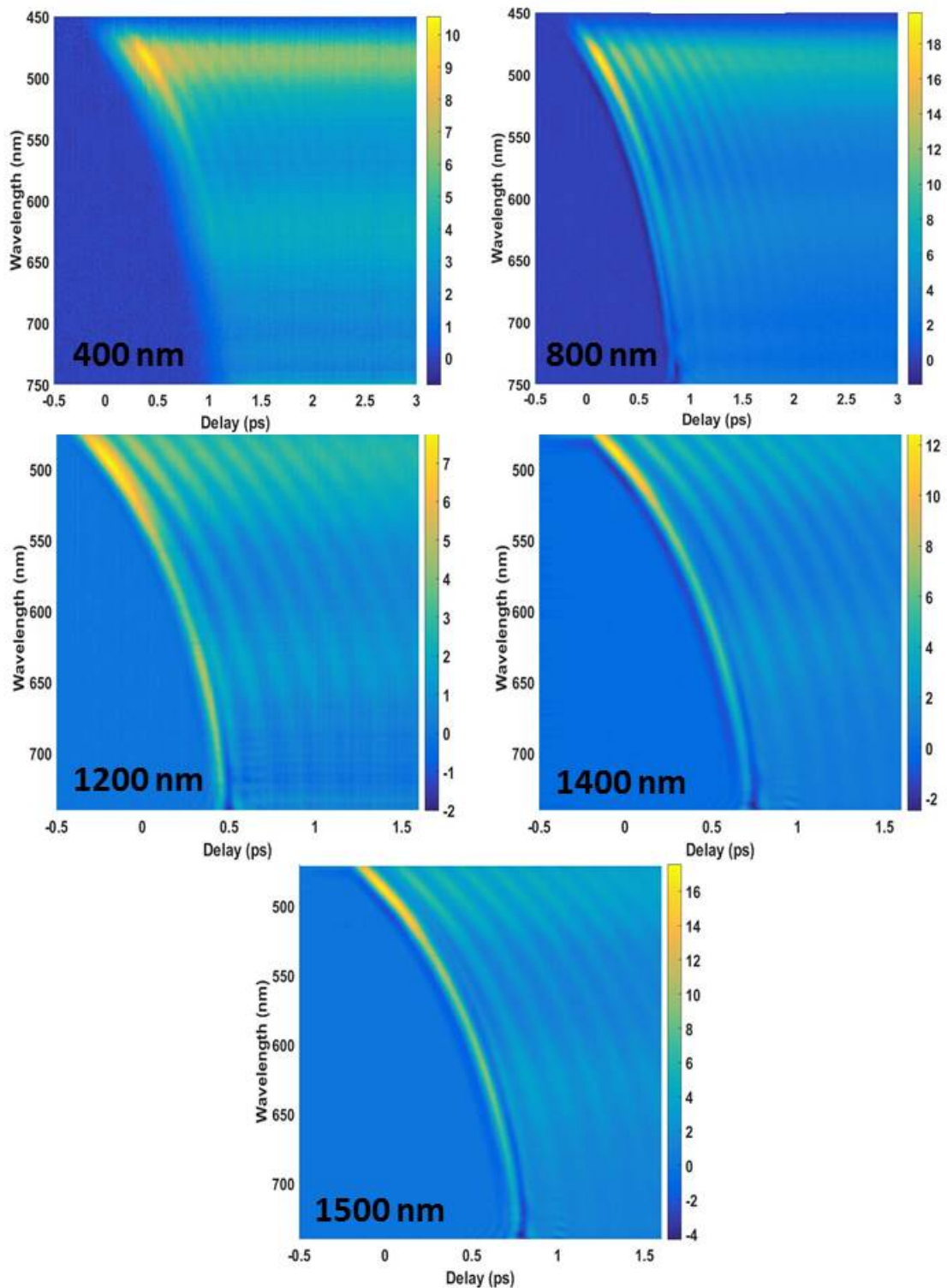


Figure 5.11: Raw absorption data for variable wavelength pump, white-light probe measurements on VO₂ films at fluence values less than required to complete the structural phase transition. The pump wavelength used is recorded in the bottom left hand side of each plot. The color scale on each plot represents the absorption.

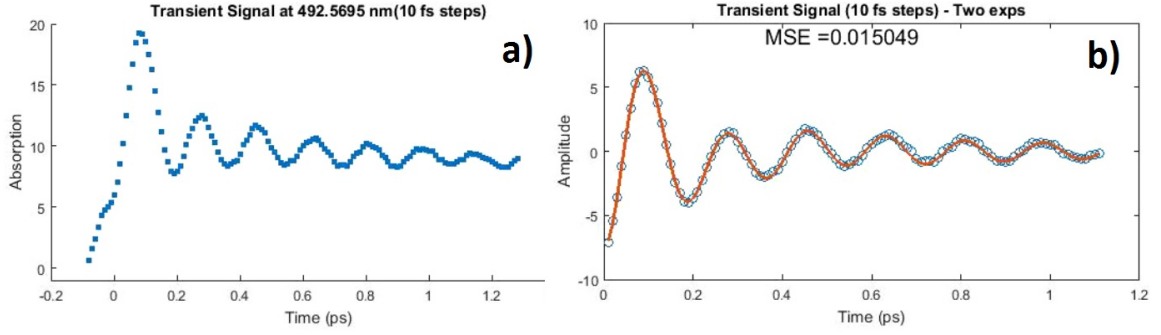


Figure 5.12: a) Raw absorption data at 492 nm when pumped at 800 nm. b) Absorption transient from a) with double exponential subtracted. Red line is a three-function fit to experimental data. The quality of the fit is quantified by the mean squared error (MSE) and displayed at the top.

has been subtracted and the model (red line) fit to the data.

To capture the oscillatory dynamics in absorption (Δa), a function of the form given by Equation 5.2 is fit using a global minimization algorithm in Matlab,

$$\frac{\Delta a}{\Delta t} = \sum A_i * e^{-B_i t} * \sin(C_i t + D_i) \quad (5.2)$$

where A,B,C and D are the free parameters which determine the initial amplitude, decay constant, frequency and phase of the coherent phonon oscillations. We choose to sum three oscillators by comparing the mean-squared error (MSE) as a function of i and observe a fourfold reduction in the MSE for each additional oscillator up to three. A sample of the agreement between the data and model when three oscillators are used is presented in Figure 5.12b. This analysis is performed on each wavelength from 470-590 nm resulting in 120 fits per pump wavelength. The fit parameters A,B,C and D are recorded for each oscillator and wavelength, a discussion of the trends follows.

The normalized contributions for each oscillator in the model (Equation 5.2) are plotted across the wavelength range for five different pump wavelengths, Figure 5.13. The contributions are calculated by integrating the $A_i * e^{-B_i t}$ term for each oscillator and normalizing to the total area. In all graphs, the red points represent the largest contribution to the model

followed by the green (second largest) and finally the blue (smallest). When pumped at 400 and 800 nm the data are noisy and there is no clear trend in the dispersion. Some of this noise can be attributed to the large amount of energy that is being dumped into the lattice. When pumping at 400 nm (4.5x band gap) and 800 nm (2.5x band gap) a significant amount of excess energy must be absorbed by the lattice as the excited electron relaxes to the Fermi level. For lower energy pump wavelengths, 1200 nm (1.5x band gap), 1400 nm (1.3x band gap) and 1500 nm (1.2x band gap) there is less noise and some dispersion appears.

Another possible source of noise in these measurements could be the pump-pulse temporal characteristics. As mentioned above, the 400 nm pump pulse is generated in BBO, the 800 nm pulse comes directly out of the amplifier and the 1200, 1400 and 1500 nm pulse are generated by an OPA. The 800 nm pulse duration was measured by autocorrelation to be ~ 40 femtoseconds. Since 800 nm is the fundamental wavelength of the laser system, we expect this pulse to be the shortest, have a Gaussian temporal profile and most closely resemble impulsive excitation of the vanadium dioxide electronic structure. As the driving force for an oscillating system approaches an instantaneous impulse, the decay time increases. According to the OPA manufacture (Coherent), pulses generated by the OPA are expected to be 1.5 times longer than the input pulse. We expect the 400 nm pulse, generated in BBO to have the longest pulse duration. The higher noise for the 800 nm pump (shortest pulse) and decrease in noise as we approach the band gap seem to indicate that the pulse duration is less of a factor than pulse energy.

A possible explanation for the dispersion may lie in the underlying phenomena which influence the optical behavior at different wavelengths. As confirmed by the work of Wall[38], the shorter wavelengths are more sensitive to changes in the atomic structure through the hybridization of the O-2p-V-2d $_{\pi}$ levels and the longer wavelengths are sensitive to changes near the Fermi level. However, this was confirmed by comparing dynamics at 525 nm with those at 800 nm, a larger wavelength range than examined by the probe pulse in these experiments.

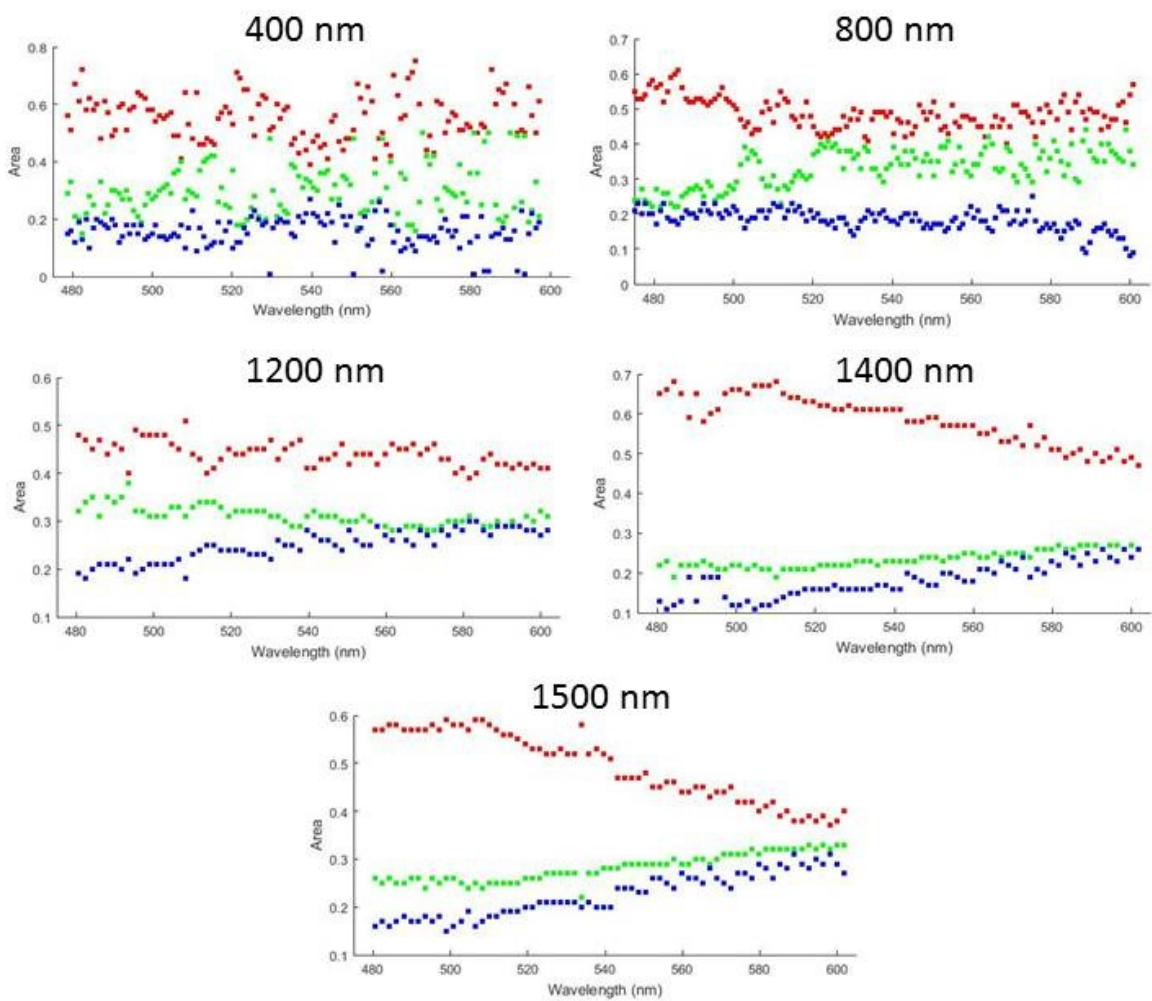


Figure 5.13: Area of each oscillator (integral of each $A_i * e^{-B_i t}$ term) normalized to the total area with pump wavelength displayed at the top. See text for more detailed description.

Plotting the frequency of each oscillator in the model *vs.* wavelength and for the five different pump wavelengths (same style as Figure 5.13 but not shown) yields a similar trend in terms of noise. For higher-energy pump pulses, the data are more noisy while lower energy pulses are less so. The dominant oscillator for all pump wavelengths is in the 5.7-6 THz range, corresponding to an A_g phonon mode in the monoclinic phase and has been previously observed by multiple groups[48, 38, 47, 39]. Some dispersion is observed for the two other oscillators at 400, 800 and 1200 nm pump wavelengths. This must be noise, since the oscillatory nature of the absorption is due to the coherent phonon oscillations and cannot have a wavelength dependence.

For all pump wavelengths, a lower frequency mode is observed between 1.7 and 2 THz. There is no monoclinic phonon mode in this frequency range. However, Gervais[155] calculated that modes in the 2-4 THz range could exist when considering lattice vibrations that extend to multiple unit cells (V_2O_4). The data also show a third mode with frequency that increases with pump wavelength. When pumping at 800 nm the third mode first appears at ~ 5.5 THz and moves to 8 THz when pumping at 1400 nm. When pumping at 1500 nm, the mode is still at 8 THz. The two commonly observed Raman modes are at 5.7 and 6.7 THz. Above this the next mode with A_g symmetry is at 9.3 THz. A mode with B_g symmetry exists at 7.9 THz, however this can not be driven by DECP.

Impulsive stimulated Raman scattering (ISRS)[140] is another mechanism capable of generating coherent phonons and the associated oscillations in absorption. Unlike DECP, ISRS can excite phonon modes of any symmetry and there is typically a π phase difference between between DECP excited modes (cos) and ISRS excited modes (sin). In Figure 5.14 the oscillator fits are plotted on absorption data at 570 nm when pumped at 1500 nm. The dominant 6 THz mode is shown in yellow along with the 1.7 (red) and 8 (purple) THz modes. The initial oscillations of the 8 THz mode are out of phase with the 6 THz mode. A peak in the absorption data also appears around 0.5 ps. This peak is observed in the raw data (Figure 5.11) and becomes more prominent at longer wavelengths. Potentially both

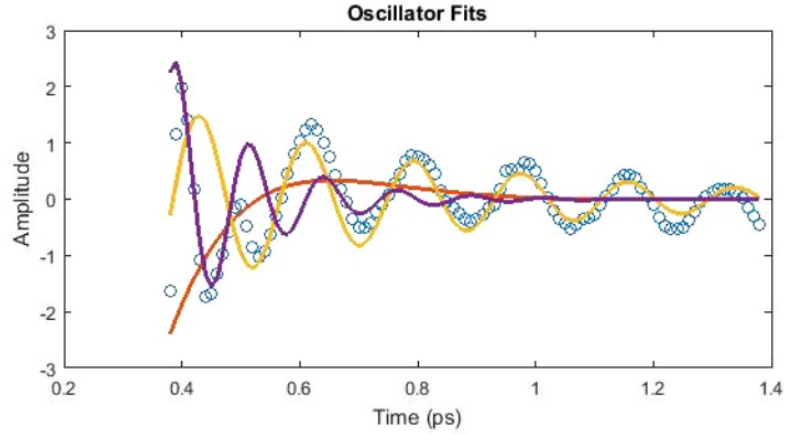


Figure 5.14: Plot showing 1.7(red), 6(yellow) and 8(purple) THz modes and data (blue circles). Absorption at 570 nm for film pumped at 1500 nm is shown (blue circles).

mechanisms are contributing to the coherent phonon generation, however it is not clear why this is more evident at longer pump and probe wavelengths.

The time constant data (B_i) indicate that the 6 THz mode has the longest lifetime for all pump wavelengths. However, at longer pump wavelengths the 6 THz time constant appears to decrease while the 1.7 and 8 THz time constants increase. The increasing time constant is consistent with excitation closer to the band gap. By pumping closer to the band gap, less electronic energy is transferred to the lattice as the excited electrons drop back down to the band edge. A lower lattice temperature should reduce phonon scattering and increase lifetime. The increase for 1.7 and 8 THz modes, at the expense of the 6 THz modes, may also have to do with coupling between modes. A closer examination of what atomic displacements these modes represent may help confirm this.

The behavior of the time constant will also depend on the temporal profile of the pump pulse. As discussed above, a shorter pulse can more easily be approximated as an impulsive excitation and more effectively drive the coherent oscillations. Without knowing the exact pulse shape, it is difficult to deconvolute the contribution to the time constant from the initial driving force (pump pulse) or the system damping.

5.4.3 Conclusions: Coherent Phonon Generation

We observe the signatures of coherent phonon motion when pumping with a wide range of wavelengths. The 6 THz mode is present along with one higher (8 THz) mode that shifts position and one constant lower (1.7 THz) frequency mode. The appearance of the 6 THz mode is consistent with the previously observed excitation mechanism (DECP) while the 8 THz mode suggests that ISRS may also play a role. At longer pump wavelengths, the phase difference between the 6 THz mode (DECP) and the 8 THz mode (ISRS) approaches the expected value of π . In general the data are fit much more cleanly when pumped at longer wavelengths. Pumping closer to the band gap deposits less energy into the lattice possibly resulting in better fits. The emergence of ISRS behavior at longer pump wavelengths is not understood.

5.5 Conclusions: Ultrafast Behavior

The existence of the monoclinic-metallic (mM) state in VO₂ has been demonstrated for the thermally and optically induced phase transition. All of the optical and electrical properties of the phase transition are now accessible without the slow structural phase transition. This result is most significant for high-speed optical modulator applications where slow recovery from the full phase transition has limited the modulation speed. However, the mM state has not been well explored. We have shown that coherent phonons can be generated when pumping VO₂ with 400 (3.0 eV), 800 (1.55 eV), 1200 (1.0 eV) 1400 nm (0.88 eV) and 1500 nm (0.82 eV) femtosecond pulses.

Differences in coherent phonon behavior may emerge when pumping closer to the band-gap (0.67 eV) with femtosecond pulses. For practical application of VO₂ as a high speed modulator, understanding the phase transition physics when pumping at 1550 nm is critical. Are there processing parameters or dopants which can further separate the electronic and structural portions of the phase transition? The effect that doping and processing param-

eters have on VO₂ optical and electrical properties has been well documented, but similar studies have not yet been conducted to determine how the temporal behavior changes. Can the non-congruence between the structural and electronic transitions be modified by processing or structuring the film? The answers to these questions will determine if vanadium dioxide is truly a material suitable for high-speed optical modulation.

Chapter 6

Electronic Structure and Optical Properties of Tungsten Doped VO₂

6.1 Introduction

Apart from substrate choice, processing and strain, one of the best ways to modify the properties of VO₂ is by doping. Among the many elements used to dope VO₂, tungsten produces by far the largest changes in T_c for a given concentration. Tungsten atoms in monoclinic phase VO₂ metalize the surrounding film[156] creating islands of metallic VO₂. The metallic domains surrounding each tungsten atom may help to lower the threshold fluence for optical excitation and seed conductive paths for electro-optic modulation. The influence of tungsten on the transition temperature, electrical properties and absorption has been well documented, but the optical constants (n and k) have not been reported.

To produce optical modulators, the optical constants must be known. In this Chapter we use spectroscopic ellipsometry (0.3-40 μm) and UV/VIS absorption measurements to understand how the optical constants and electronic structure of vanadium dioxide change with tungsten doping. In the NIR spectral region, this information will help determine if tungsten doped VO₂ can enhance the performance of optical modulators. Optical properties in the phonon region (10-40 μm) provide insight into the dynamics of the monoclinic metallic state.

6.2 Tungsten-Doped Vanadium Dioxide

Of the nearly twenty oxides of vanadium that exist, about half a dozen exhibit a thermally induced phase transition. The VO₂ phase transition is the most convenient to work with because it occurs close to room temperature at 340 K, compared to V₄O₇ and V₃O₅, the next closest, which switch at 238 K and 430 K, respectively. For some applications it is desirable to reduce the VO₂ transition temperature even further and doping has emerged

as the best way to achieve this. Typically, elements with higher oxidation states such as W^{6+} , Mo^{5+} and Nb^{5+} reduce the phase transition temperature while lower oxidation state elements such as Cr^{3+} , Al^{3+} , Fe^{3+} and Ga^{3+} tend to increase the transition temperature. Of the known dopants, tungsten is by far the most effective at modifying the transition temperature, reducing the transition temperature by roughly 50 K per atomic percent[157].

Tungsten atoms have been shown to fit substitutionally into the VO_2 lattice for individual vanadium atoms and create a locally strained environment.[156, 158] Electrical measurements typically observe an increase in conductivity for the monoclinic state with little change to the rutile. Optical measurements (absorption) also show little change in the rutile state but absorption in the monoclinic state increases. In general, the monoclinic state is significantly modified by tungsten doping with little or no change to the rutile phase. In the following sections, we present the optical constants (n and k) as measured by ellipsometry from 0.3-40 μm , for VO_2 thin films doped with tungsten, and attempt to understand changes in the band structure using UV/VIS/NIR absorption measurements from 0.4-7.0 eV.

6.2.1 Contributions

We use ellipsometry and UV/VIS/NIR absorption measurements to characterize the optical properties and electronic structure of vanadium dioxide thin films doped with tungsten. To the best of our knowledge, this is the first work to measure the optical constants of tungsten-doped VO_2 . This work will provide a fundamental understanding of how tungsten is incorporated into the VO_2 lattice and is a critical part of a current NASA phase II SBIR project.

Atomic % Vanadium	Atomic % Tungsten	Label	T _c C
100	0	100-0	70
98	2	98-2	56
95	5	95-5	45
93	7	93-7	34
92	8	92-8	32
90	10	90-10	27

Table 6.1: Sputtering Target Composition

6.3 Optical Properties of Tungsten Doped VO₂

6.3.1 Fabrication

Thin films (~ 100 nm thick) of tungsten doped vanadium dioxide were deposited on silicon substrates by reactive RF sputtering as described in Chapter 4.2. Composite sputtering targets with different vanadium-to-tungsten ratios were used to achieve different doping levels. The target composition, labeling scheme and transition temperature, as recorded by white light reflectivity measurements, are presented in Table 6.1. To collect optical data on the 90-10 sample in the monoclinic state would have required cooling the sample to below room temperature; no method of dealing with condensation was available. Prior to deposition, the backside of each substrate was roughened by sandblasting to eliminate backside reflections.

6.3.2 Experimental Setup

Two J.A. Woollam spectroscopic ellipsometers were used to collect Ψ and Δ at three angles (50° , 60° and 70°) and at 25°C and 85°C , where Ψ and Δ are defined by Equation 6.1

$$\tan(\Psi)e^{i\Delta} = \frac{R_p}{R_s} \quad (6.1)$$

and R_p and R_s are the Fresnel reflection coefficients for p and s polarized light, respectively. A M2000 ellipsometer with heated stage accessory recorded data from 0.3-1.6 μm and an IR-VASE unit with home-built heater provided data from 1.6-40 μm . The data were modeled with CompleteEASE software from J.A. Woollam. Each data set was modeled with a silicon substrate layer, 2 nm native oxide layer and ~ 100 nm thick oscillator layer. For the IR data, up to thirteen oscillators with three free parameters each were used to model the data, while in the visible, no more than five were required. For all IR spectra, fits with a mean-square error (MSE) of less than 10 were achieved and in the visible less than two. Additional optical characterization was performed with a Raman microscope and UV/VIS/NIR spectrometer.

6.3.3 Results and Discussion: 10-40 μm

Since ellipsometry is a model-based technique, and the models used for this analysis have up to 45 free parameters, it is necessary that the resulting optical constants be compared to existing work. The optical behavior will be primarily described in terms of the imaginary part of the dielectric function (k) because it is being modeled directly (by oscillators) while the real part (n) is calculated by Kramers-Kronig analysis of the imaginary part. The infrared optical properties of pure vanadium dioxide in the phonon region, 10-40 μm (200-800 cm^{-1}), have been investigated previously by Huffman[159] and the most relevant results of this work are presented in Figure 6.1 (a) and (b). From the symmetry of the monoclinic structure, 15 IR active phonon modes must exist; seven longitudinal (Figure 6.1a) and seven transverse (Figure 6.1b). The eighth longitudinal mode has been observed before[160] but is outside the spectral range for this work (and Huffman) at 53 μm (189 cm^{-1}).

The imaginary part of the dielectric function for a undoped VO_2 film on silicon is shown in Figure 6.2. The positions of the oscillators used by Huffman[159] are shown by red (longitudinal modes) and black (transverse modes) dotted lines. The agreement is

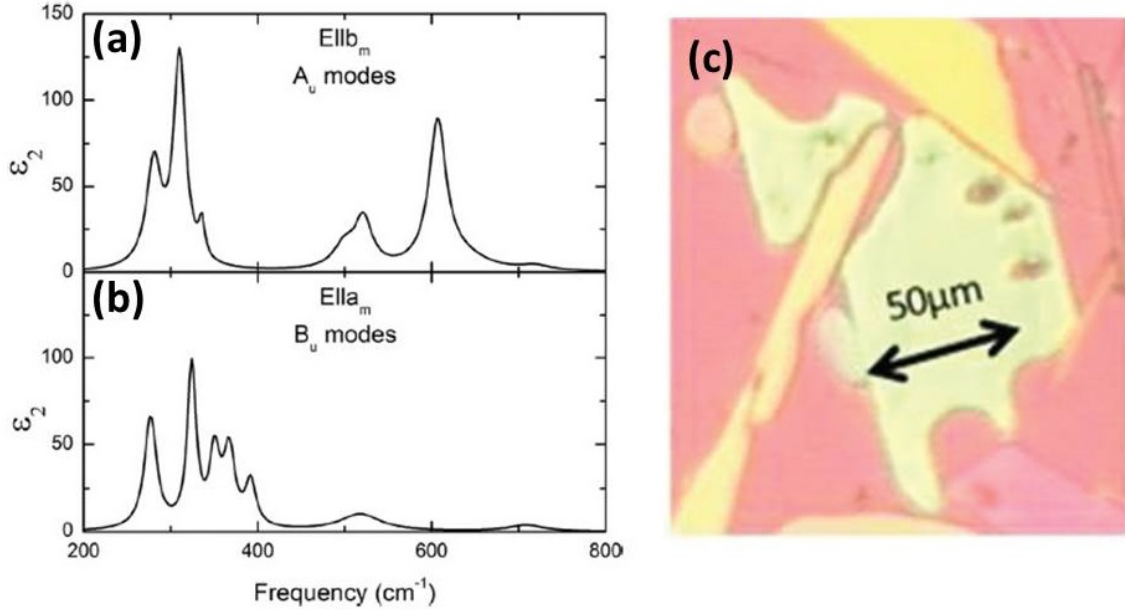


Figure 6.1: Imaginary part of the VO₂ dielectric function as measured along the monoclinic b_m (a) and a_m (b) crystal directions by Huffman[159]. (c) Large single crystal platelet of VO₂ used in experiments by Huffman[159].

quite good, with peaks in absorption lining up with oscillator positions. It is important to consider that significant differences exist between the two samples; a large single crystal grown on quartz at high temperature and a thin film on silicon. Thin VO₂ films grown on silicon do not have a preferential crystallographic orientation and it is expected that the structure of the dielectric function should be some convolution of the spectra in Figure 6.1 a and b. In addition, there is almost certainly a difference in the strain state for a thin film with ~ 100 nm grains and a 50 μm single crystal, however a direct analysis has not been carried out.

In Figure 6.3, the imaginary part of the dielectric function is plotted for pure VO₂ along with doped films with four different tungsten concentrations. The raw magnitude of k for the five samples does not show any trend when plotted and makes interpretation difficult; the curves are shifted for clarity and to illustrate trends. Phonon modes, initially positioned at ~ 525 cm^{-1} and ~ 645 cm^{-1} in pure films, shift to lower frequency with increased tungsten concentration. The peak initially at position A (~ 275 cm^{-1}) becomes

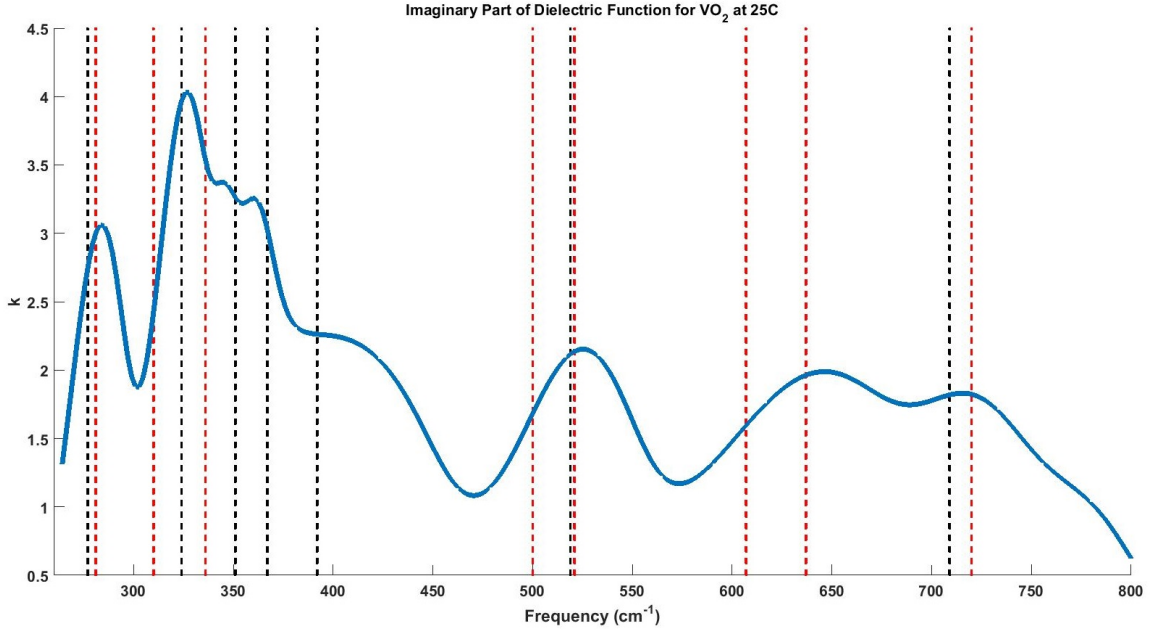


Figure 6.2: Imaginary part of the monoclinic dielectric function measured for a undoped VO_2 film deposited on silicon. The vertical red dotted lines show the position of oscillators representing longitudinal modes while the black dotted lines indicate the position of those for the transverse modes, as used by Huffman[159]. Two oscillators are used to capture the asymmetry of the longitudinal mode between 600 and 650 cm^{-1} .

broader and the magnitude is decreased with increasing tungsten concentration. The peaks at position B in the pure film (transverse modes) appear to merge and decrease in amplitude with increasing tungsten concentration.

The most striking feature in the imaginary part of the dielectric function for the rutile phase is seen in the 100-0 film, Figure 6.4. Due to the rutile phase crystal symmetry, seven IR modes exist and three of these are doubly degenerate. Huffman[159] observed four and only two of these are in reasonable agreement with our data (285 and 460 cm^{-1}). The peak at 710 cm^{-1} (14 μm) is observed in infrared absorption measurements (Figure 6.7b) confirming that it is not an artifact of the modeling. It is not clear why the discrepancy exists. However, the behavior for all of the doped films looks very similar. Work examining the influence of tungsten doping on the monoclinic and rutile phase properties has consistently shown that doping modifies the properties of the monoclinic state to make it

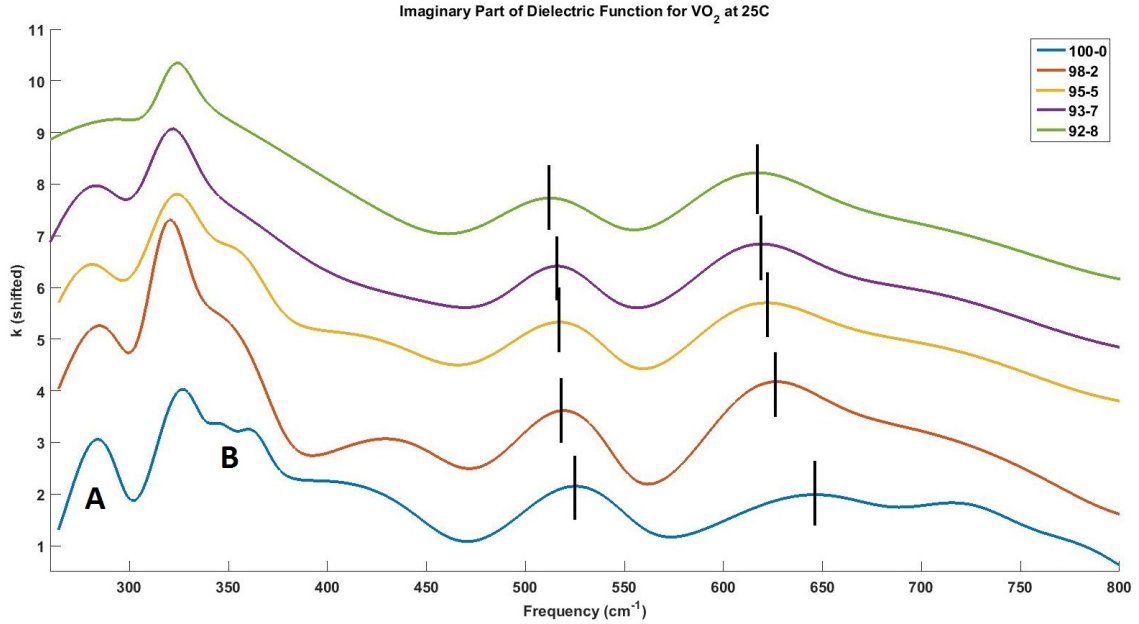


Figure 6.3: Imaginary part of the monoclinic phase dielectric function measured for undoped and doped VO_2 films deposited on silicon. The curves are shifted vertically for clarity. Features which evolve with increased tungsten doping are noted by A and B along with vertical lines.

more “metallic” and does not appear to influence the properties of the rutile phase.

Raman measurements provide additional confirmation of the phonon mode softening. In Figure 6.5, the three most prominent Raman peaks in monoclinic VO_2 are shown. The peaks in 6.5a show a much more pronounced shift while the shift in 6.5b is more subtle. It should also be noted that a substantially longer integration time (more than tenfold) is required to resolve peaks in the 93-7 and 92-8 samples compared to the pure (100-0) samples. This is consistent with the fact that tungsten doping increases the metallic character of the film, and Raman peaks are not clearly resolved in the metallic state. Of the 18 Raman peaks in monoclinic VO_2 , these are the only three which exhibit a frequency shift. The peaks at $\sim 194 \text{ cm}^{-1}$ and $\sim 225 \text{ cm}^{-1}$, 6.5(a), correspond to the 5.6 and 6.7 THz phonon modes which can be generated coherently by femtosecond laser excitation[38]. In unpublished work[161], softening of the coherent phonon modes generated by femtosecond laser excitation in tungsten-doped films has been observed, consistent with what is seen

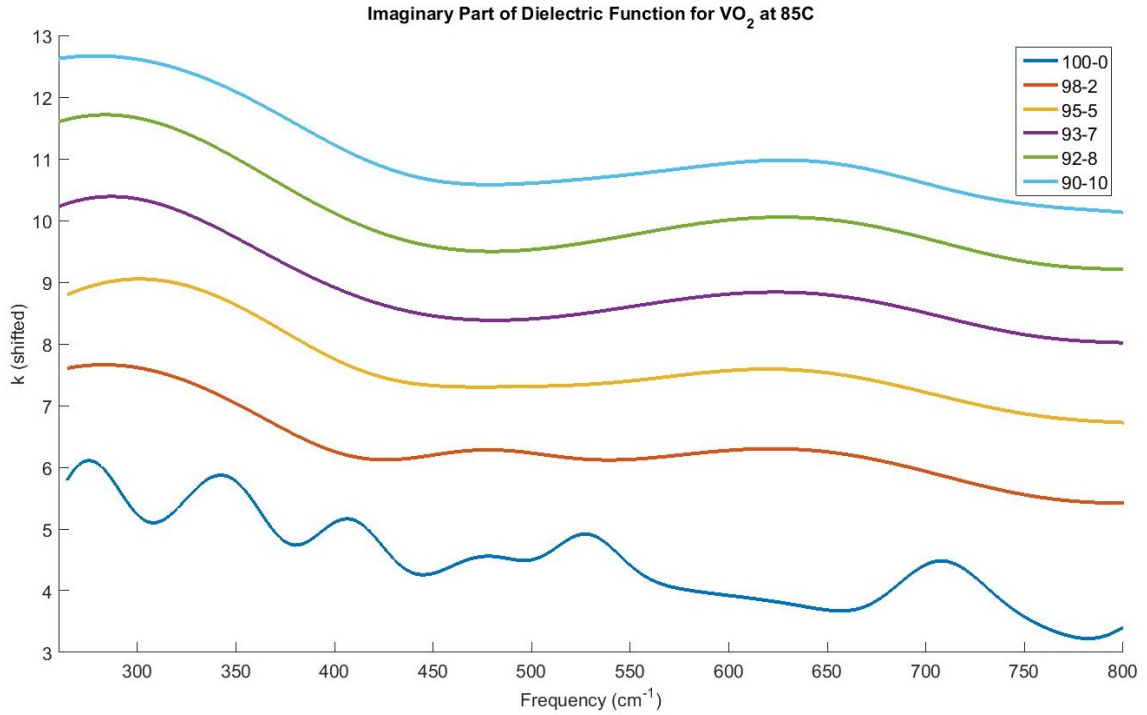


Figure 6.4: Imaginary part of the rutile phase dielectric function measured for undoped and doped VO_2 films deposited on silicon. The curves are shifted vertically for clarity.

here.

6.3.4 Results and Discussion: 1.6-12 μm

In the spectral range from 1.6-12 μm the monoclinic phase absorption is relatively flat and featureless with no trend in amplitude observed. The rutile phase has significantly more structure in this region, Figure 6.6. Similar to Figure 6.4, k for the doped films has a consistent shape while the undoped film is quite different. Again, infrared absorption measurements (Figure 6.7b) have the same shape for all the doped films while the pure film has a very different structure. The peaks between 10 and 12.5 μm are present, indicating that the ellipsometry model is consistent with absorption measurements. Looking at the behavior of the doped films, there is a broad peak from 1.5 to 9.5 μm that appears to broaden with increasing amounts of tungsten. Optical behavior in this spectral region

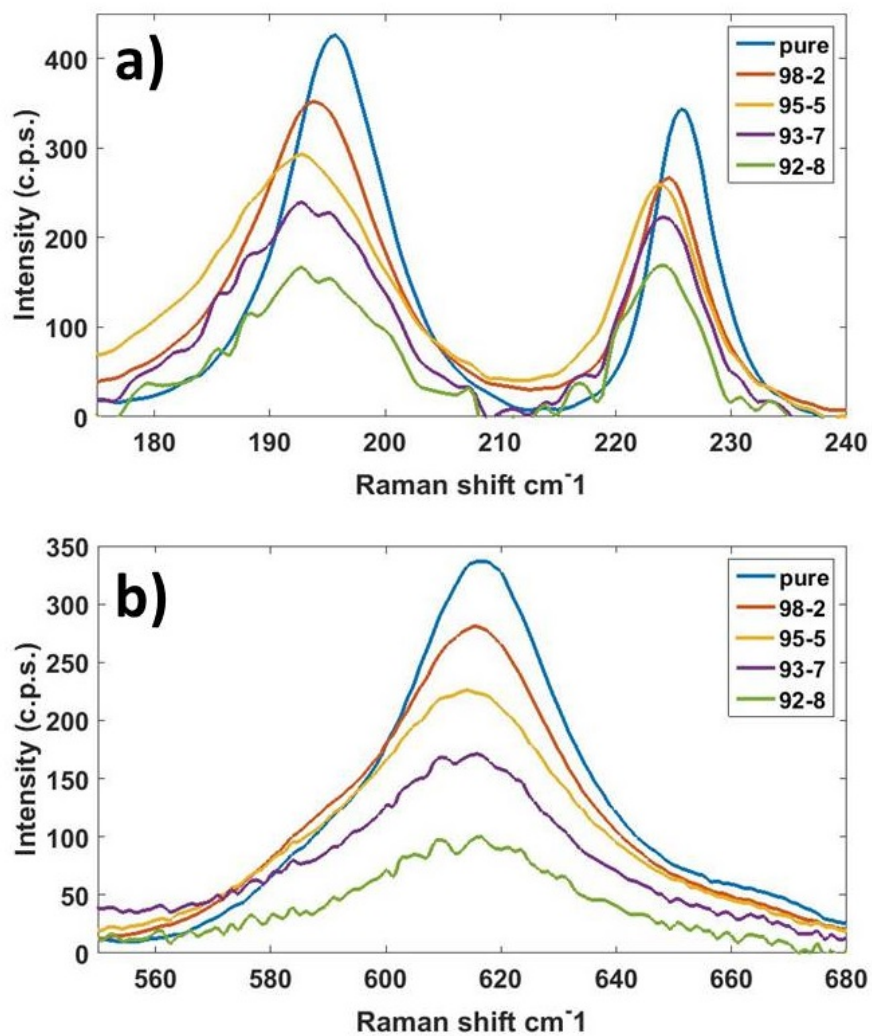


Figure 6.5: Peaks in Raman spectra that soften with increasing tungsten concentration at (a) $\sim 194 \text{ cm}^{-1}$ and $\sim 225 \text{ cm}^{-1}$ and (b) $\sim 615 \text{ cm}^{-1}$.

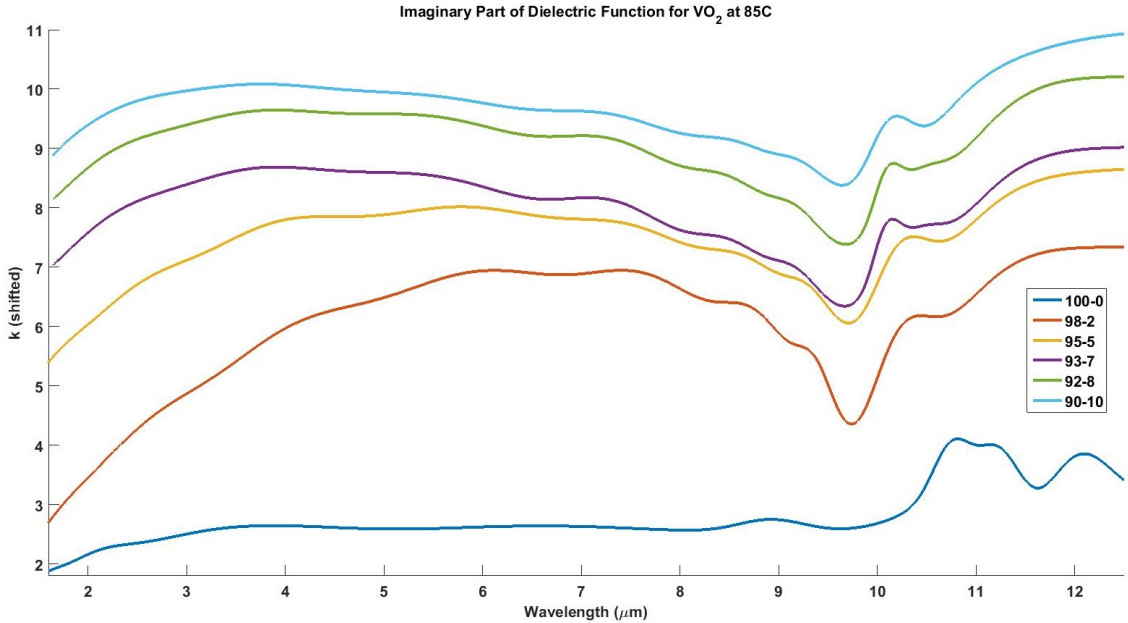


Figure 6.6: Imaginary part of the rutile phase dielectric function measured for undoped and doped VO₂ films deposited on silicon. The curves are shifted vertically for clarity.

is typically governed by defects or small polarons. In addition, tungsten ions contribute two free electrons to each metal-atom lattice site, which could possibly account for these differences. Theoretical work is still in progress and will be needed to determine if either of these mechanisms is responsible for the observed optical behavior.

Absorption measurements in this spectral range can provide some complementary information to the ellipsometry analysis, however absorption from O₂, CO₂ and H₂O make a direct comparison difficult. In Figure 6.7a and b, the features from 2-8 μm are the result of atmospheric absorption. The dip (6.7b) and spike (6.7a) at 15 μm can be attributed to CO₂. Atmospheric absorption bands are much less of an issue for ellipsometry because it is not an intensity-dependent measurement and only looks at the difference in polarization between the incident and reflected light. Specific absorption bands will reduce the signal strength in an ellipsometry measurement, requiring a longer measurement time, but do not impart specific features to the data.

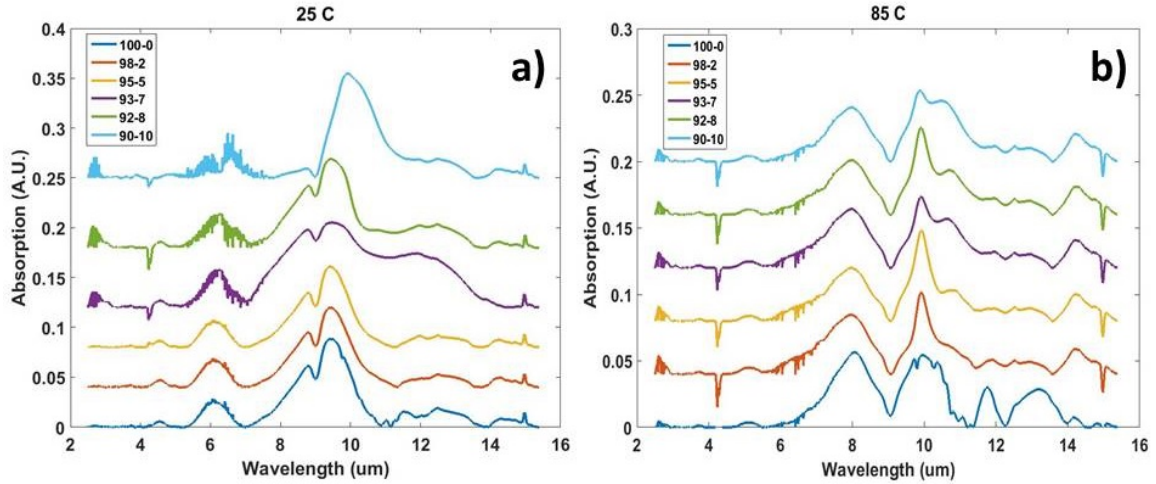


Figure 6.7: Absorption measurements for undoped and doped VO₂ films deposited on silicon at 25 C a) and 85 C b). The curves are shifted vertically for clarity.

6.3.5 Results and Discussion: 0.3-1.6 μm

Ellipsometry measurements and the resulting optical constants for pure VO₂ have been published by multiple groups[11, 160, 90], and are in reasonable qualitative agreement. The dielectric function, as modeled in these measurements, has the same general shape as the data reported by KanaKana[11], Barker[160] and Cueff[90], however the quantitative agreement is much better with the more recent data by Cueff than the work of KanaKana and Barker. This suggests that there are likely variations in the optical properties of VO₂ which depend on the film processing.

To aid in our interpretation of these results, absorption data from 0.4-7 eV were collected. In Figure 6.9, the absorption data are fit by a sum of five Voigt (Gaussian + Lorentzian) functions to extract the peak electronic transition energies. The transition energies compare well to what Qazilbash[162] reported: we see a peak at 4.4 eV that is expected to exist but was not observed in previous work[162]. Spectra are collected and fit for all samples in both hot and cold states and tabulated in Table 6.2. Considering the electronic structure, as presented by Qazilbash (Figure 6.8), the absorption peaks in the monoclinic phase, labeled A, B, C and D (left hand side of Table 6.2) correspond to transitions between

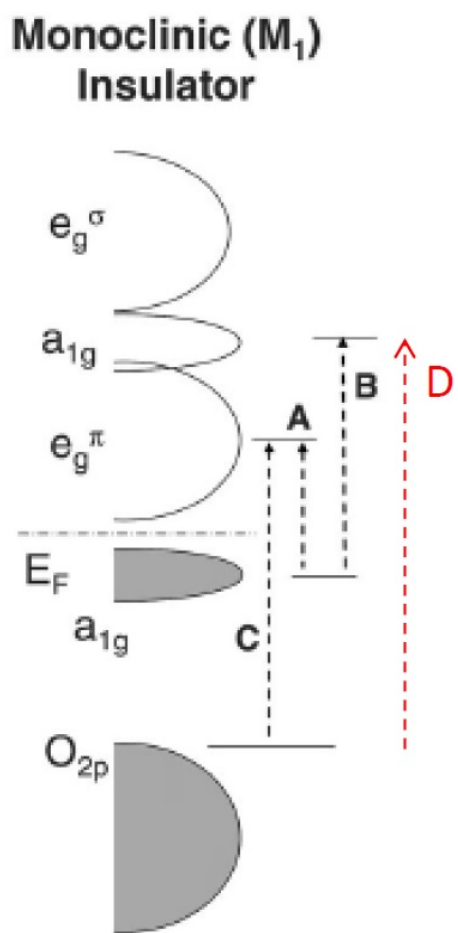


Figure 6.8: Electronic structure of monoclinic VO_2 , from Qazilbash[162]. Red arrow indicates transition observed in this work but not in the original paper.

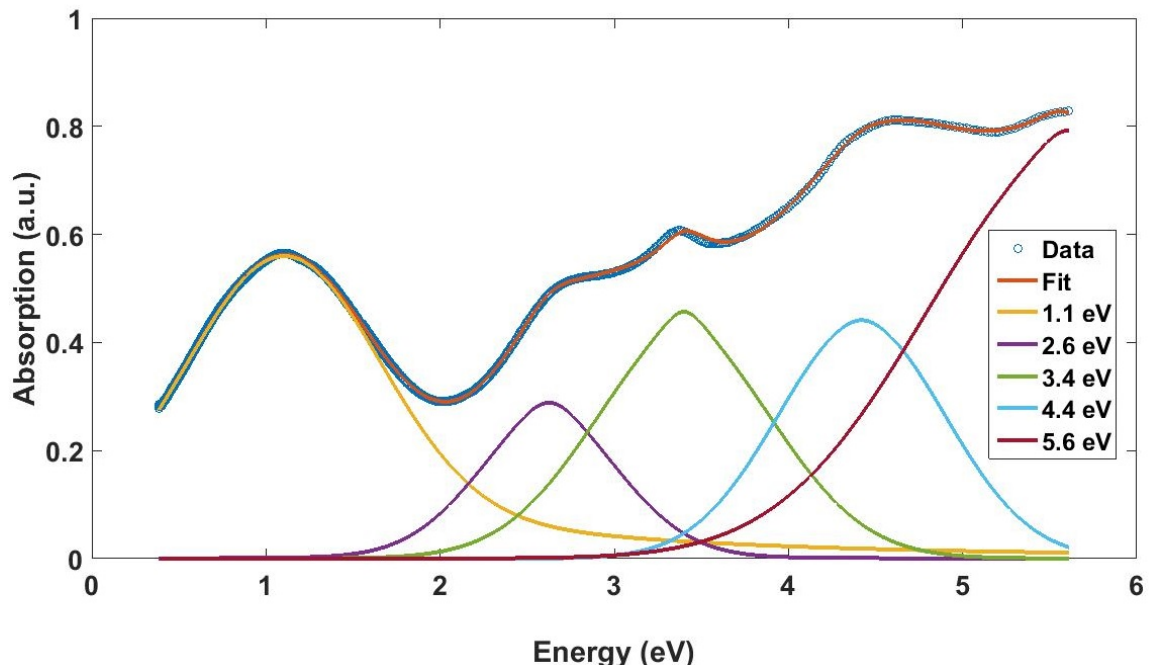


Figure 6.9: Absorption spectra for a monoclinic phase undoped VO₂ film deposited on silicon. The blue points are fit by summing up multiple Gaussian + Lorentzian functions to determine the energy of various electronic transitions.

the $a_{1g} \rightarrow e_g^\pi$, lower $a_{1g} \rightarrow$ upper a_{1g} , $O_{2p} \rightarrow e_g^\pi$ and $O_{2p} \rightarrow$ upper a_{1g} levels. The A and B transitions increase in energy with higher tungsten doping, indicating that the lower a_{1g} level likely shifts to lower energy. Because the C and D transitions do not shift, it is likely that the O_{2p} and upper a_{1g} level are not moving.

An examination of changes in the monoclinic state extinction (k) changes with tungsten doping, Figure 6.10, there is no significant change in structure in the range from 700-1700 nm, which remains flat, and as with previous data the amplitude does not have a consistent trend. For the 100-0, 98-2 and 95-5 samples, the peaks in the 400-600 nm range move in a ziz-zag manner, similar to the B transition energy. Other than the slight correlation just mentioned, the UV/VIS/NIR absorption data do not provide any additional insight into the ellipsometry data. However, the data may be helpful for theoretical calculations and confirms that the lower a_{1g} band is moving.

The imaginary part of the rutile state dielectric function does not change significantly

Film	A (eV)	B (eV)	C (eV)	D (eV)	AA (eV)	BB (eV)	CC (eV)	DD (eV)
	25 C	25 C	25 C	25 C	85 C	85 C	85 C	85 C
100-0	1.1	2.6	3.3	4.4	1.6	2.7	3.3	4.4
98-2	1.4	2.4	3.3	4.5	1.7	2.5	3.4	4.5
95-5	1.1	2.5	3.4	4.5	1.6	2.6	3.3	4.4
93-7	1.6	2.7	3.3	4.4	1.6	2.5	3.4	4.5
92-8	1.6	2.7	3.4	4.4	1.7	2.6	3.3	4.4
90-10	1.7	2.6	3.4	4.4	1.9	2.8	3.4	4.4

Table 6.2: Peak positions for electronic transitions in the monoclinic (A,B,C,D) and rutile states (AA,BB,CC,DD) as extracted by fitting the data.

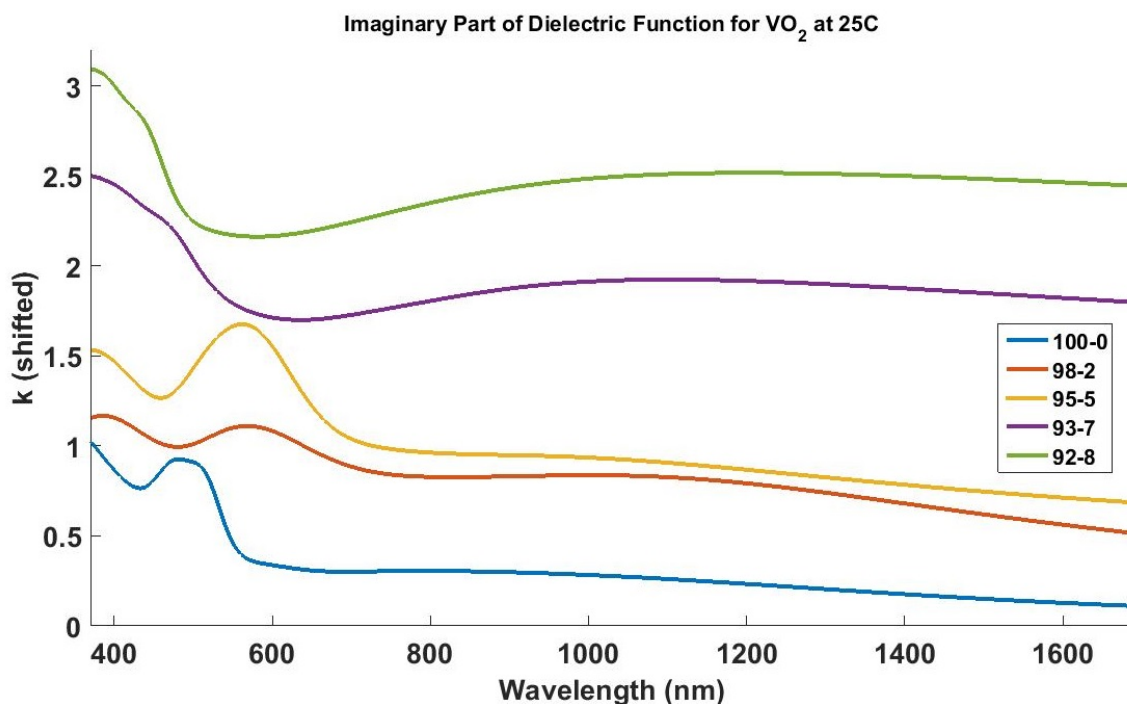


Figure 6.10: Imaginary part of the monoclinic phase dielectric function measured for undoped and doped VO_2 films deposited on silicon. The curves are shifted vertically for clarity.

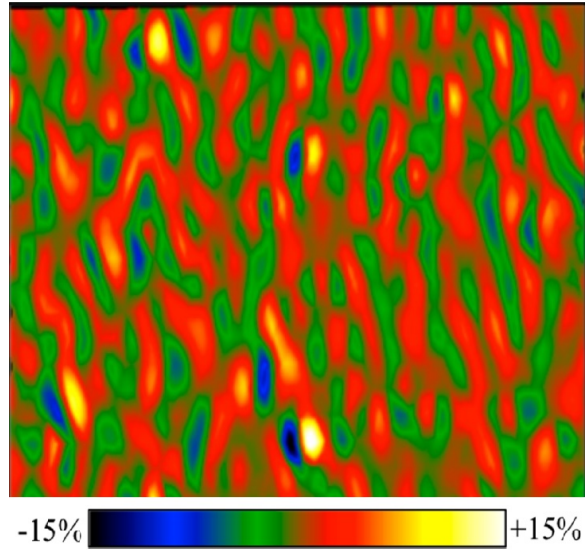


Figure 6.11: Atomically resolved strain maps for tungsten doped VO_2 . [158] Blue regions show tensile strain (+15%) and yellow indicate compressive strain (-15%).

when comparing the data for pure films (100-0) and heavily doped films (90-10). This is consistent with the UV/VIS/NIR data which do not show any shift in the peak position as the tungsten concentration increases.

6.4 Conclusions

In general, the metallic state electronic structure does not change as much with tungsten doping as the semiconducting state does. This is consistent with other results that show increasing metallicity of the monoclinic phase with doping. A recent report examining tungsten doping in single crystals using aberration-corrected STEM may help explain some of the observed behavior [158]. When crystals doped with 0.2 atomic % tungsten were examined, the resulting strain maps indicate highly localized strains, as shown in Figure 6.11. The tungsten atoms produce regions with high and low strain in close proximity; the blue and yellow regions indicate -15% and +15% strain, respectively. At higher tungsten concentrations (0.8 atomic %) the strain is nearly uniform and tungsten atoms can not be located from the strain maps.

Density functional theory (DFT) calculations show that phonon modes in W doped VO₂ (red curve) shift to higher frequency, relative to the undoped material (black curve), Figure 6.12. These calculations are for $\sim 1\%$ W doping, which is slightly more than the highest doping ($90-10 \approx 0.9$ at % W) examined in our ellipsometry measurements. The higher frequency shift is consistent with compressive strain in the lattice due to the larger size of the tungsten atoms. This may not be an accurate picture in light of the work presented above, because Figure 6.11 and the shift to higher frequency does not agree with our results.

In the calculations shown in Figure 6.12, no attempt has been made to replicate the local strain as shown in Figure 6.11. Calculations which include these local strains will need to be performed. The relatively low concentrations of tungsten present in these films makes simulations very time consuming. For $\sim 1\%$ tungsten doping, an atomic lattice with 107 vanadium atoms, 1 tungsten atom and 216 oxygen atoms must be constructed. Since integer numbers of atoms must be used, the simulation size quickly grows very large (and computationally demanding) for the low doping levels measured in our work.

Theoretical calculations will need to determine if local or uniform strain can account for differences observed in the optical behavior. Also, it is not known how similar the thin film and single crystal environments are. No comparable work exists to show where and how the tungsten atoms are incorporated in thin films. Does the larger concentration of defects in thin films accommodate strain differently? These issues will be key to understanding what is occurring in the electronic structure.

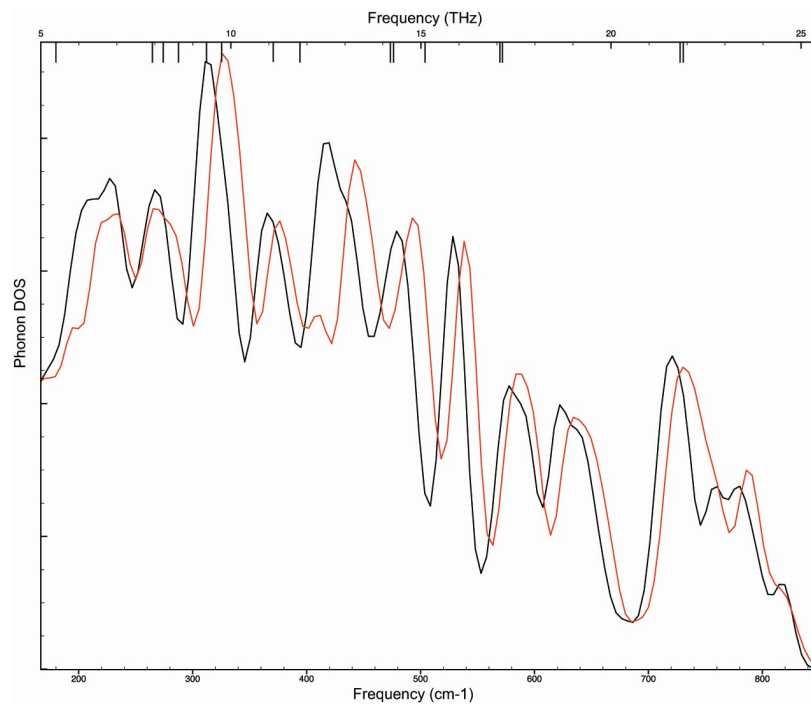


Figure 6.12: Density functional theory calculations showing the phonon density of states for pure VO₂ in black and W doped (~1 %) VO₂ in red[161].

Chapter 7

Outlook for VO₂ Based Optical Devices

In this dissertation, we have explored the fundamental physics of vanadium dioxide and produced compact devices for optical modulation. We have successfully produced optical modulators which are limited in reconfiguration speed only by the excitation laser pulse duration (25 ns). The next stage for this application will use picosecond and possibly femtosecond pulses to trigger optical modulation. In the nanosecond switching regime, we demonstrated that rings without VO₂ do not have a sizable shift in the resonant wavelength when pumped. Femtosecond laser pulses will contain much higher peak field intensities which may introduce additional optical effects. However, all of the existing work that explores the phase transition dynamics at femtosecond time scales has been performed on large area thin films. Sub-micron patches of VO₂ on top of a silicon waveguide may behave differently. Free beam coupling has been used for the excitation laser in all previous experiments, and true on-chip devices will need to couple femtosecond pulses into waveguides.

Although we successfully incorporated optically active erbium into VO₂, the effect of the phase transition on the erbium luminescence was quite small. This limited switching contrast could potentially be the result of poor coupling between the vanadium dioxide lattice and the erbium atoms, or perhaps because the phase transition does not significantly alter the Er³⁺ ion environment. Theoretical studies may be able to determine to what extent the local environment must be distorted to affect the Er³⁺ luminescence. Understanding how the vanadium dioxide lattice incorporates erbium atoms is also crucial. We have seen Er luminesce, indicating Er³⁺ ionization and we observe the VO₂ phase transition, but without TEM studies, the extent to which erbium is incorporated in the VO₂ lattice is not known. Perhaps an alternate strategy, such as that demonstrated by Cueff[90] would be

more effective.

As indicated by our work, physical vapor deposition processes may produce films with similar optical hysteresis properties, but the electrical and morphological properties are very different. The processes used in this dissertation deposit amorphous films at room temperature, which then must be annealed to produce switching VO_2 . This represents an improvement over high-temperature deposition processes as they are compatible with polymer based lithography resists and minimizes the time at elevated temperature. However, this process is still incompatible with many metals, as they are not stable at the $450\text{ }^\circ\text{C}$ annealing temperature. Perhaps the deposition parameters can be varied to reduce the thermal barriers for crystallization. Rapid thermal annealing or laser annealing may be able to reduce the thermal load. Another area which has proven difficult is etching. Small patches ($\sim 100\text{ nm}$) do not switch when fabricated by reactive ion etch processes. Fabrication processes need to be developed with an emphasis placed on material compatibility.

Very little work has explored the physics of the phase transition when pumping close to the band gap. In addition to the work presented in this dissertation, there is only one other paper which examines the switching fluence dependence for different pump wavelengths. In most femtosecond spectroscopy systems 800 nm is a convenient excitation wavelength, but it is not practical for optical modulators. Another important parameter to consider will be the pulse characteristics. Most experiments looking at the dynamics of the excited monoclinic state have been performed using sub-100 femtosecond pulses. Do pulses with longer duration excite the dynamics in the same way? In terms of coherent phonon generation, the temporal profile will certainly matter but can the structural and electronic portions of the phase transition still be separated? Practical questions like these still need to be answered.

Drastic changes in the phase transition temperature, optical properties and electrical properties occur when only a few atomic percent of tungsten is incorporated into the vanadium lattice. In single crystals, the location of the tungsten atoms and their influence on

the lattice has been directly determined[156, 158]. At low concentrations in single crystals, the tungsten atoms produce highly localized strain and are randomly distributed throughout the crystal. Somewhere between 0.2 atomic % and 0.8 atomic % the strain becomes delocalized. Knowing the exact positions of the tungsten atoms and how they strain thin films will be key to understanding the physics. For high-speed optical modulation, the separation between the structural and electronic transitions is critically important. The fundamental question remaining is to what extent can doping and processing separate these components?

APPENDICES

Appendix A

Supplementary Information for Chapter 4

Supplementary Information

Influence of deposition process and substrate on the phase transition of vanadium dioxide thin films

R.E. Marvel¹, R.R. Harl², V. Craciun³, B.R. Rogers², and R.F. Haglund Jr.^{1,4}

¹Interdisciplinary Graduate Program in Materials Science, Vanderbilt University, Nashville,

²Chemical and Biomelecular Engineering, Vanderbilt University, Nashville

³National Institute for Laser, Plasma and Radiation Physics, 077125 Magurele, Bucharest, Romania,

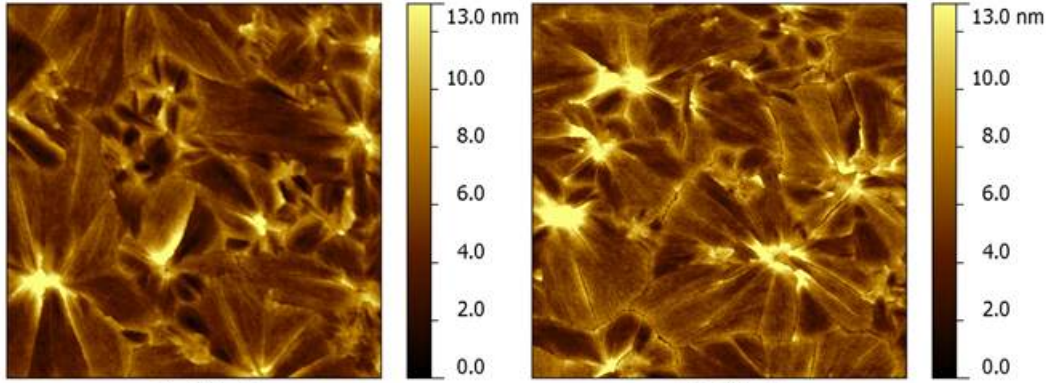
⁴Physics Department, Vanderbilt University, Nashville

Due to space limitations in chapter 3, we present data for all samples produced in this supplementary information. AFM images for all samples and the calculated roughness values are included. XPS data and the specific parameters for deconvoluting the bonding states are presented. Examples of the fit quality for optical hysteresis measurements are included. Finally, Raman spectra for all samples are displayed.

S1-9: AFM images

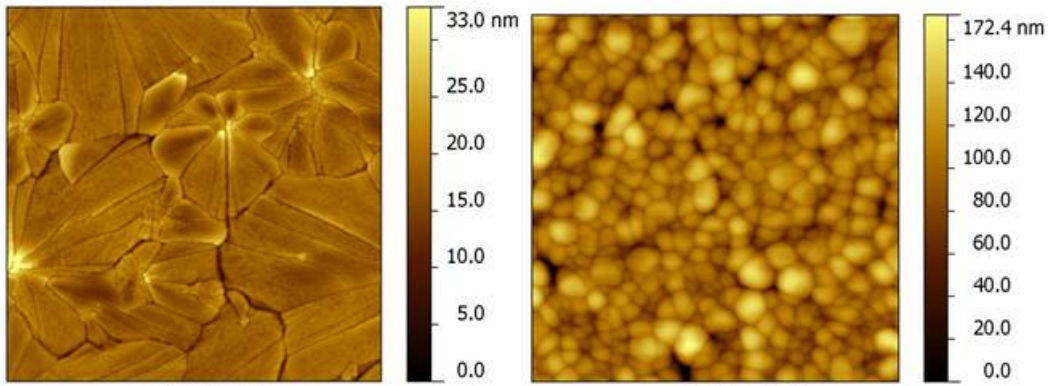
AFM images for all samples produced in this work are presented in S1-9. The images displayed are all 5 μm x 5 μm square and are taken from larger 10 μm x 10 μm scans. The data are leveled by mean plane subtraction and the contrast is adjusted to provide maximum detail for the features present. Multiple scans were done on each sample to ensure that the observed structures are present across the sample. For selected samples, cross sections of the AFM data are provide to highlight specific features. AFM image leveling and analysis was performed using Gwyddion software.

S1



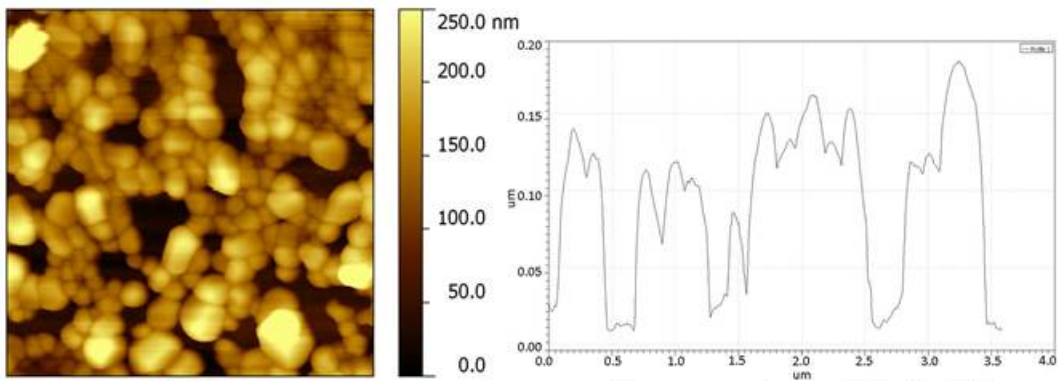
P_Si_2

P_Si_5



P_Si_10

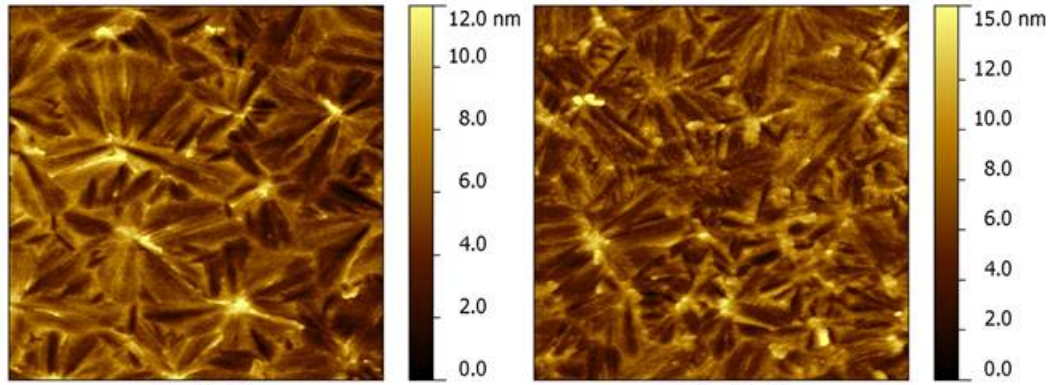
P_Si_30



P_Si_90

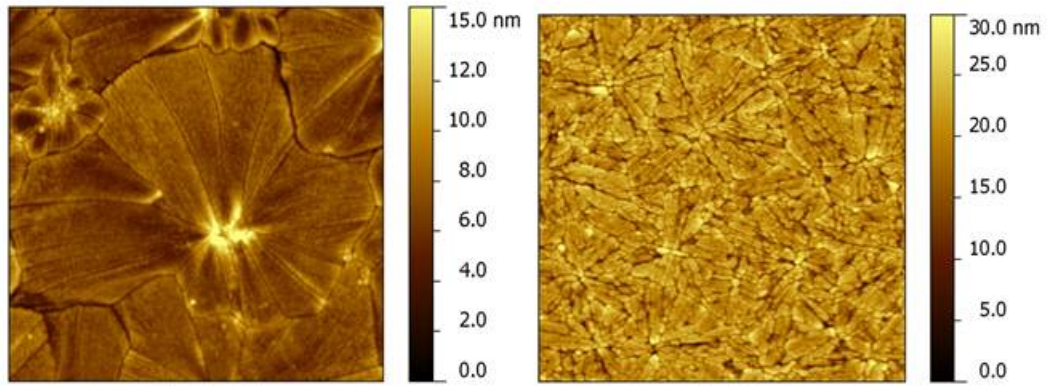
Cross section of P_Si_90 3

S2



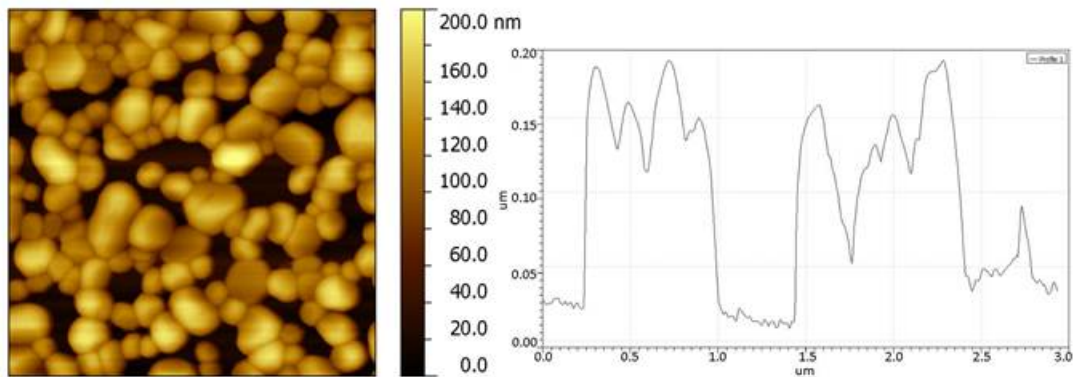
P_G_2

P_G_5



P_G_10

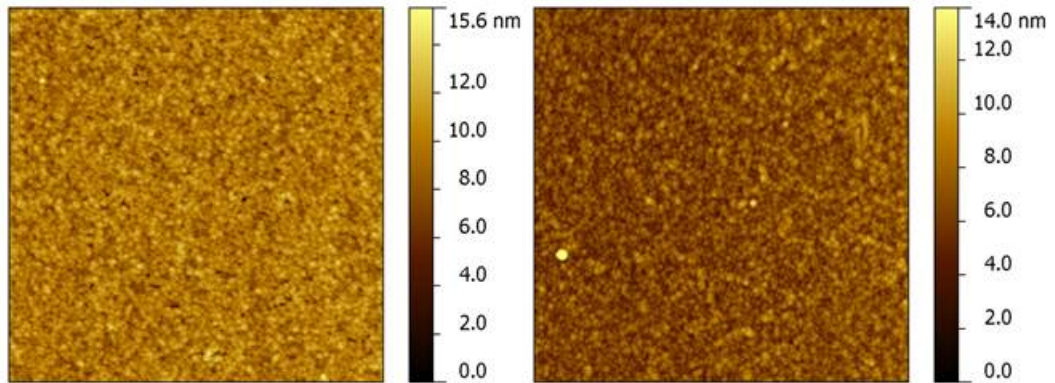
P_G_30



P_G_90

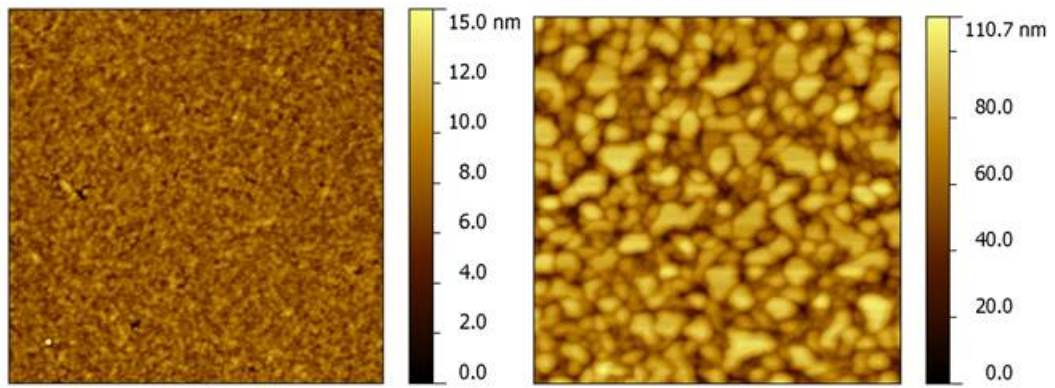
Cross section of P_G_90 4

S3



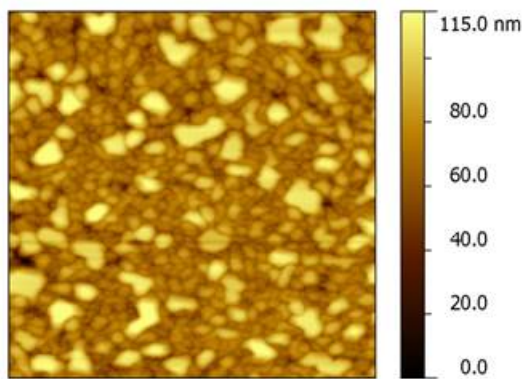
P_Sa_2

P_Sa_5



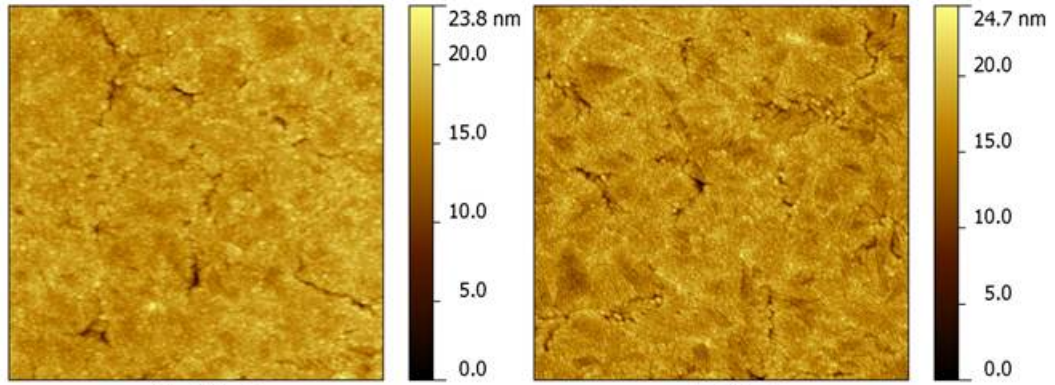
P_Sa_10

P_Sa_30



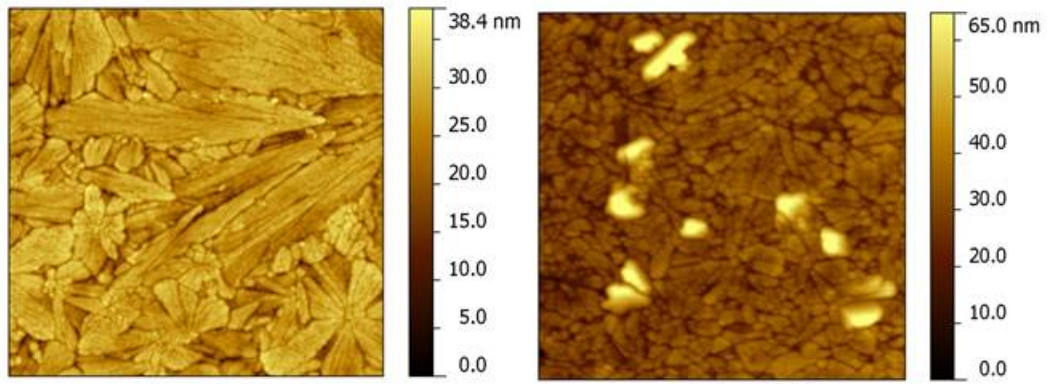
P_Sa_90

S4



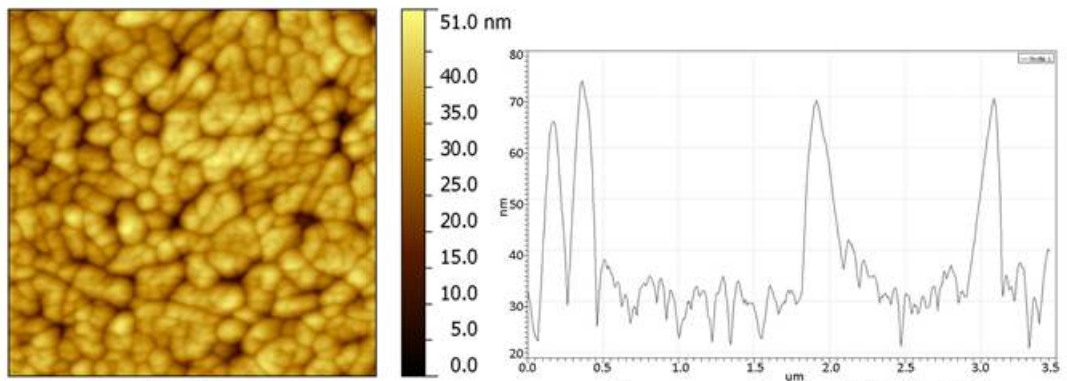
E_Si_2

E_Si_5



E_Si_10

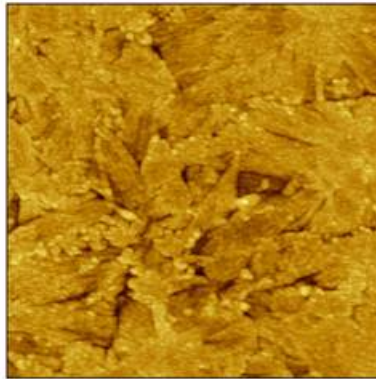
E_Si_30



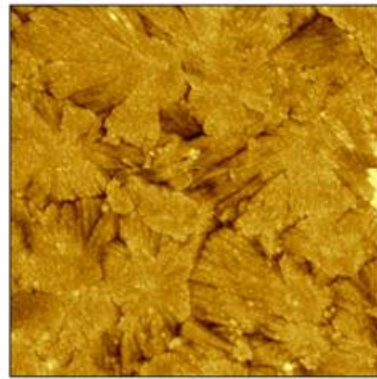
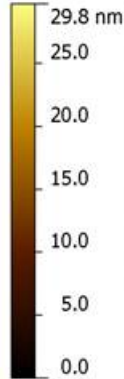
E_Si_90

Cross section of E_Si_30 6

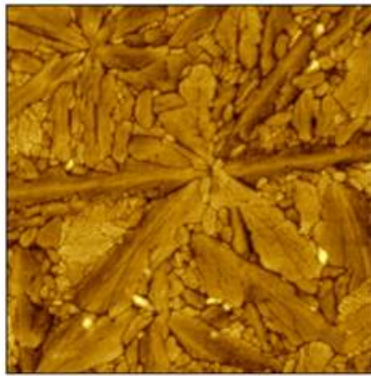
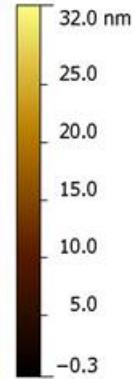
S5



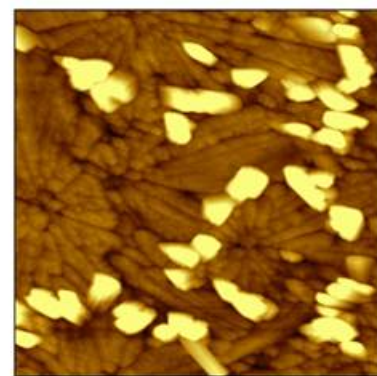
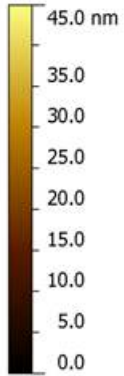
E_G_2



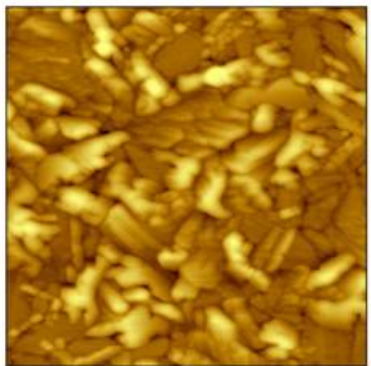
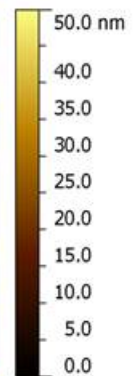
E_G_5



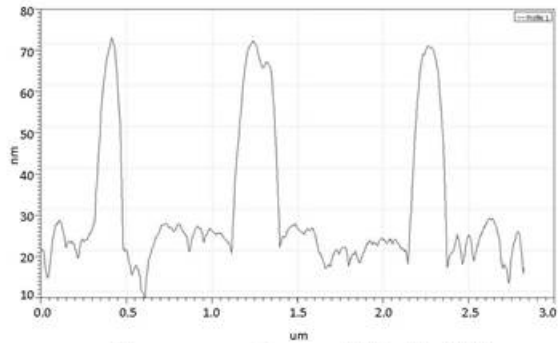
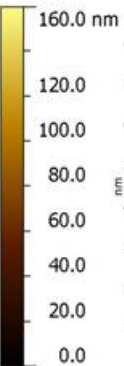
E_G_10



E_G_30

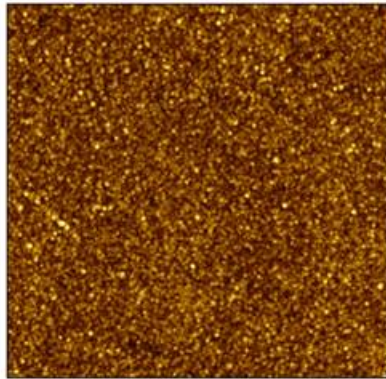


E_G_90

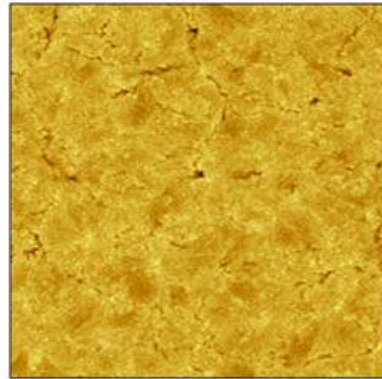
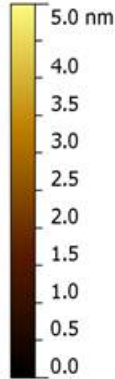


Cross section of E_G_30 7

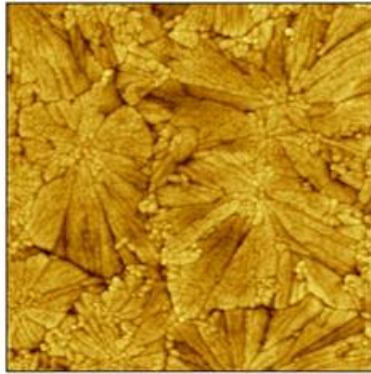
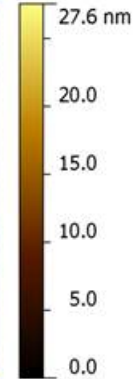
S6



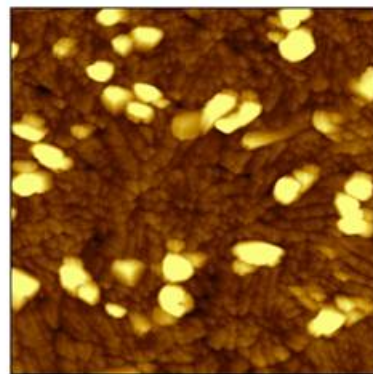
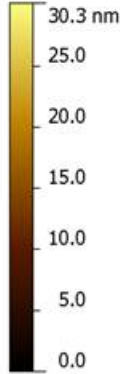
E_Sa_2



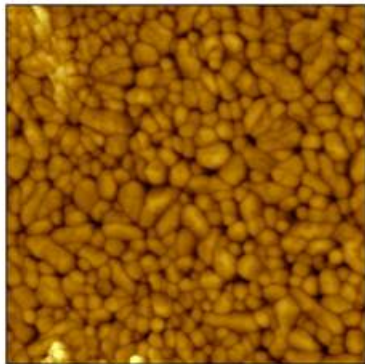
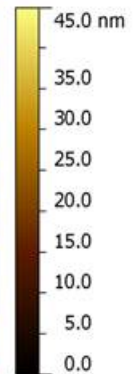
E_Sa_5



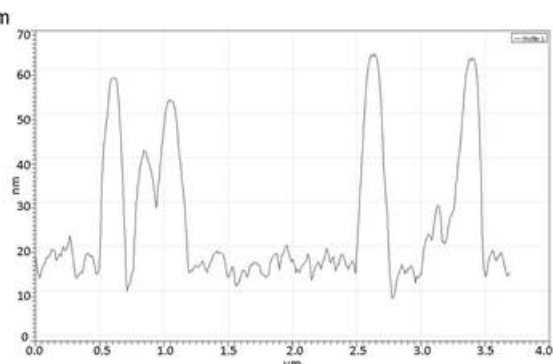
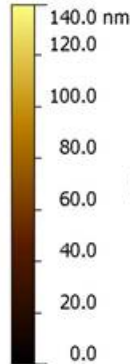
E_Sa_10



E_Sa_30

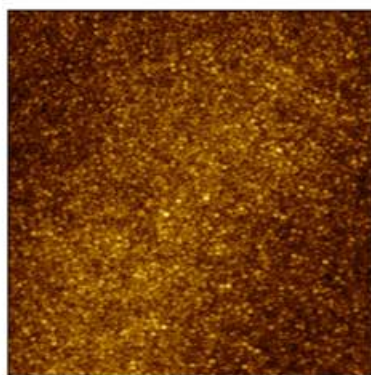


E_Sa_90

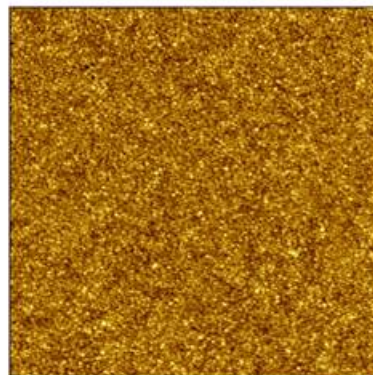
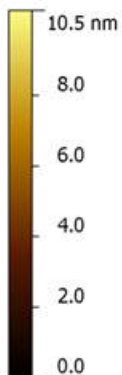


Cross section of E_Sa_30 ₈

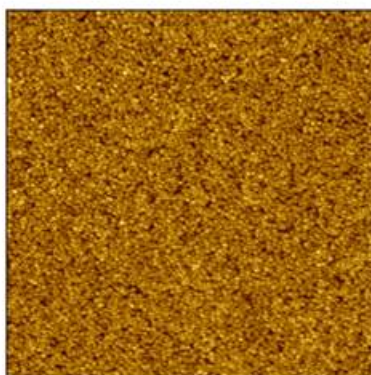
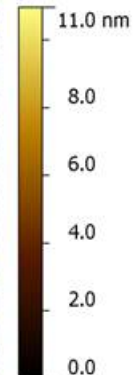
S7



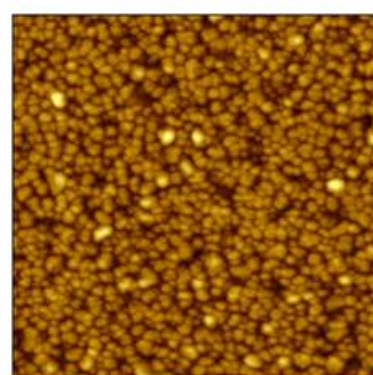
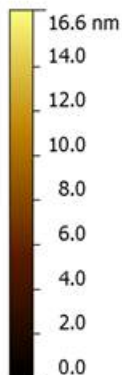
S_Si_2



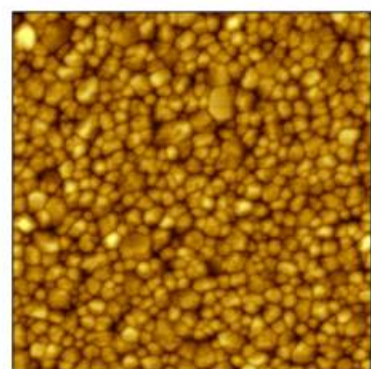
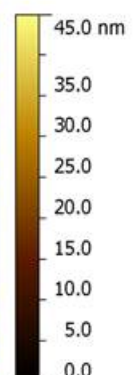
S_Si_5



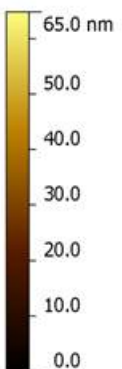
S_Si_10



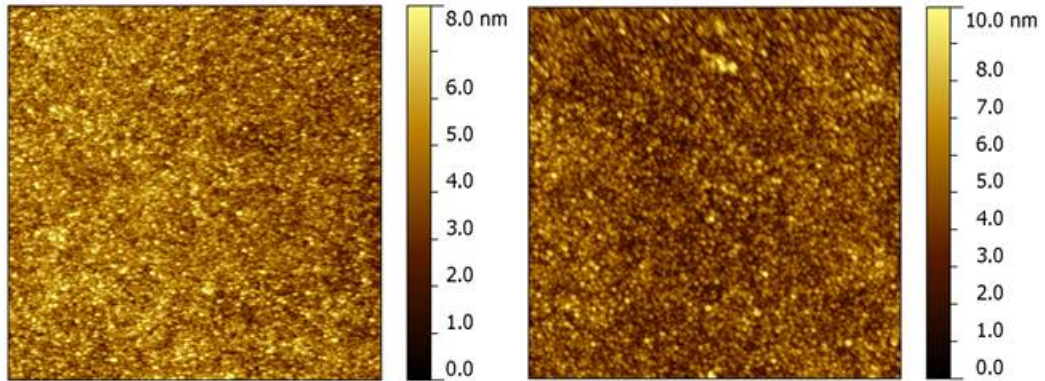
S_Si_30



S_Si_90

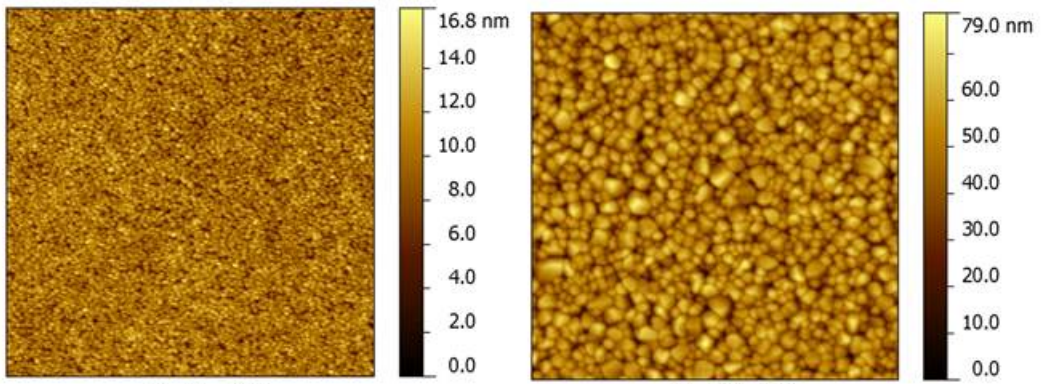


S8



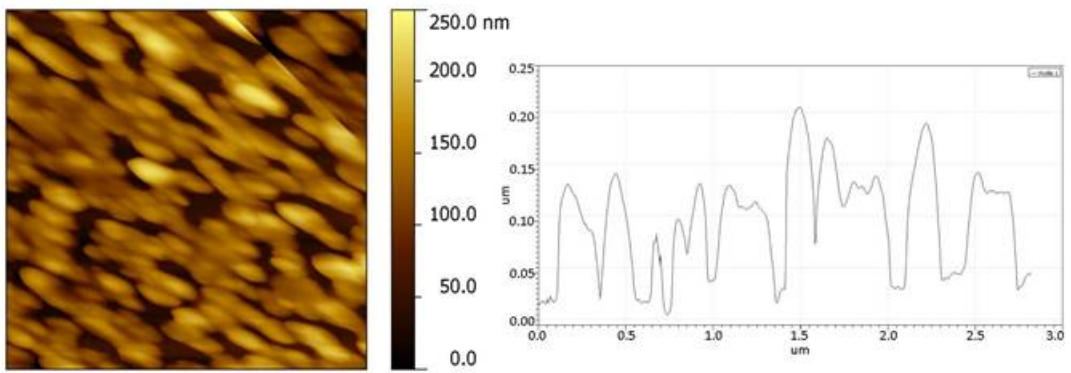
S_G_2

S_G_5



S_G_10

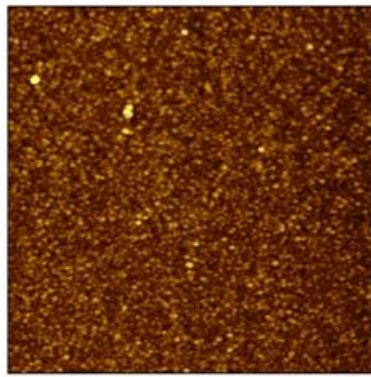
S_G_30



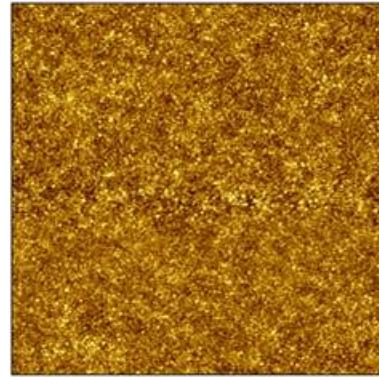
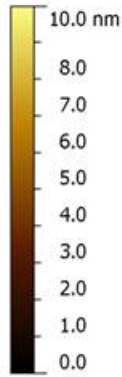
S_G_90

Cross section of S_G_90 10

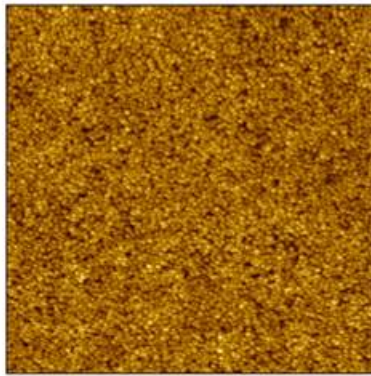
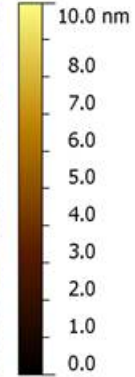
S9



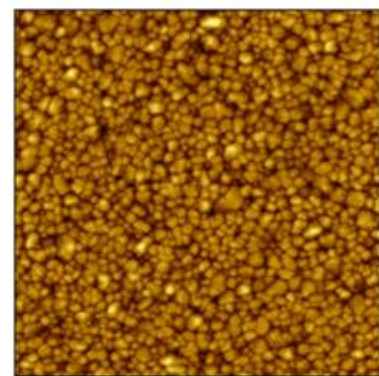
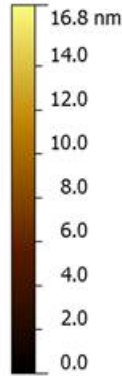
S_Sa_2



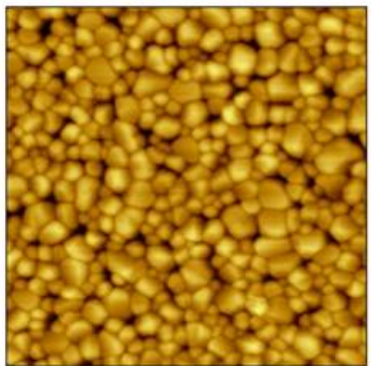
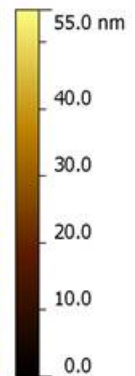
S_Sa_5



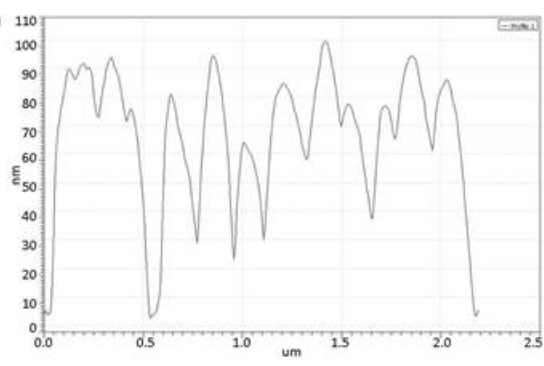
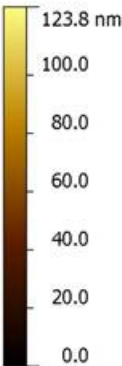
S_Sa_10



S_Sa_30



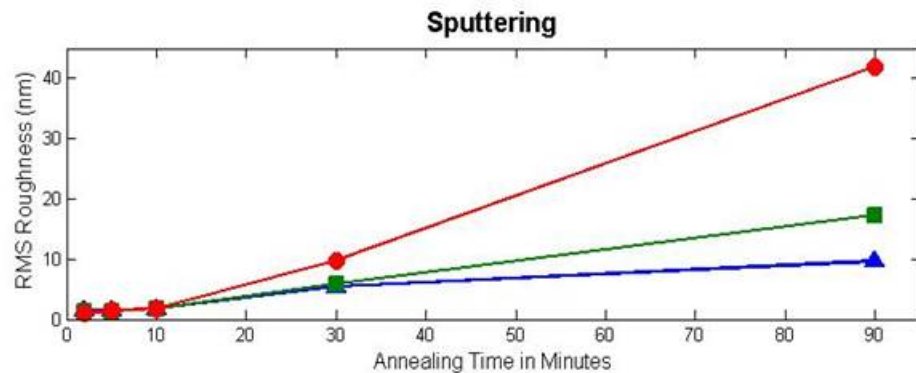
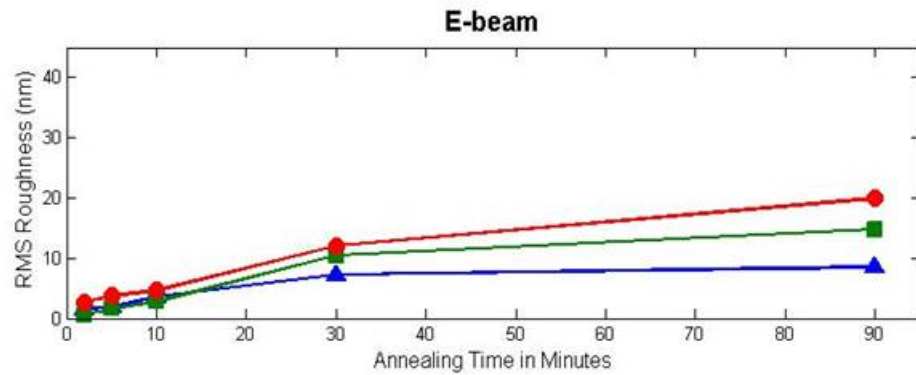
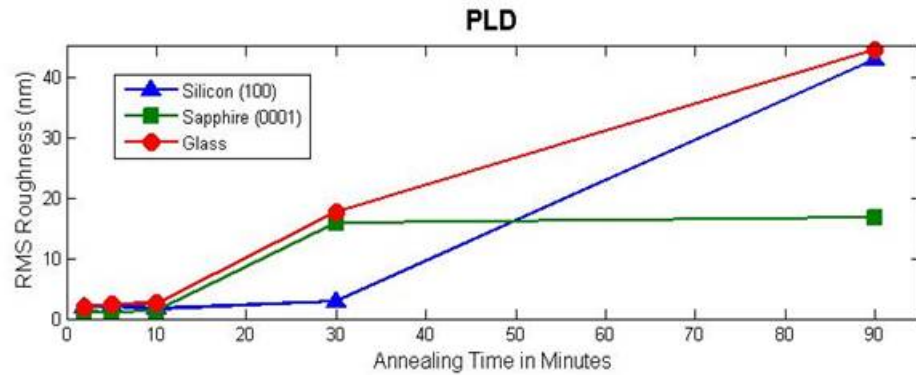
S_Sa_90



Cross section of S_Sa_90₁₁

S10: RMS Roughness

The RMS roughness values presented below are extracted from 10 um x 10 um AFM scans using Gwyddion software. Lines are added to guide the eye.



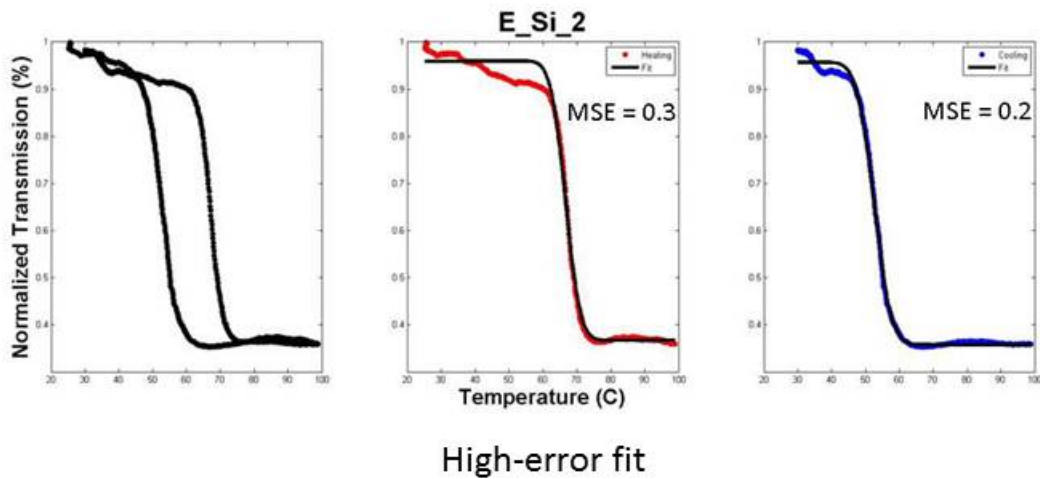
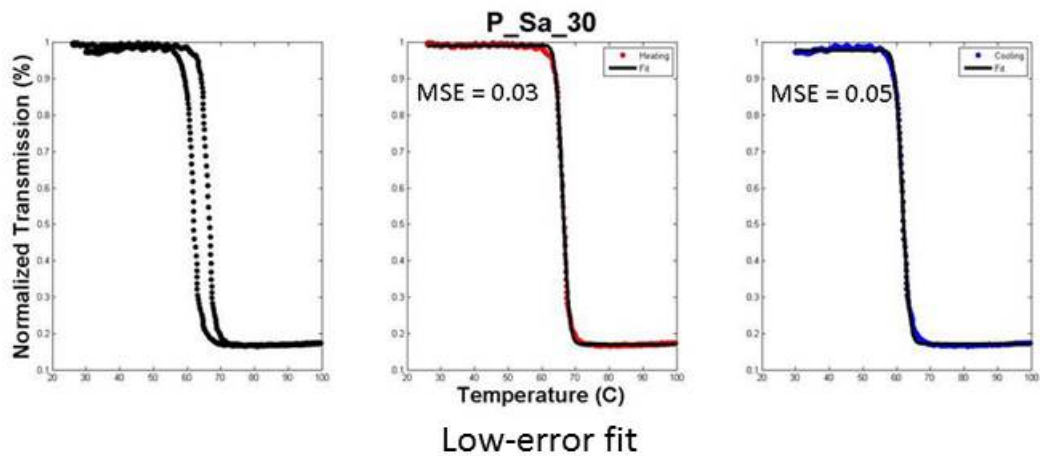
S11: XPS Composition Analysis

Atomic Composition (%)				
Sample	V2p	O1s	C1s	N1s
E-beam	25.4	60.0	12.8	1.9
PLD	24.4	58.0	19.1	3.9
Sputter	24.8	60.0	13.4	1.8
V2p _{3/2} Bonding Information (BE/FWHM/%Peak)				
Sample	V ₂ O ₅	V ₆ O ₁₃	VO ₂	V ₂ O ₃
E-beam	517.3/1.65/41.1	516.8/1.1/7.0	516.1/1.49/42.6	515.0/1.7/9.3
PLD	517.3/1.54/62.2	-	516.1/1.42/35.4	514.8/1.45/2.4
Sputter	517.3/1.65/35.5	516.7/1.5/20.0	516.1/1.45/29.5	515.0/1.65/14.9

Table of XPS results for as-deposited (no phase transition) samples on silicon showing the atomic composition of each sample. The deconvolution of the V2p_{2/3} peak bonding states is also shown.

S12: Hysteresis Fit Quality

The images below show the range in fit quality observed for optical hysteresis curves fit using a sigmoidal function.



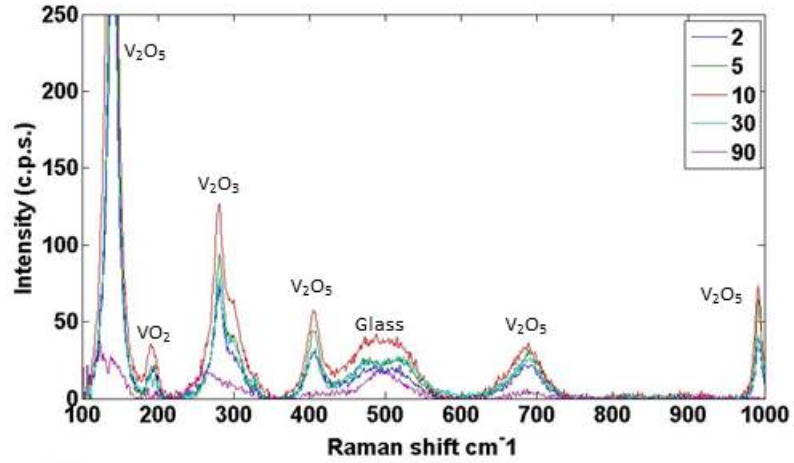
Two thirds of all the fits performed have a MSE below 0.2. The higher values for MSE are the result of poor agreement between the data and fit in the upper parts of the hysteresis, as shown above. In these cases the data are on both sides of the fit.

S13-15: Raman

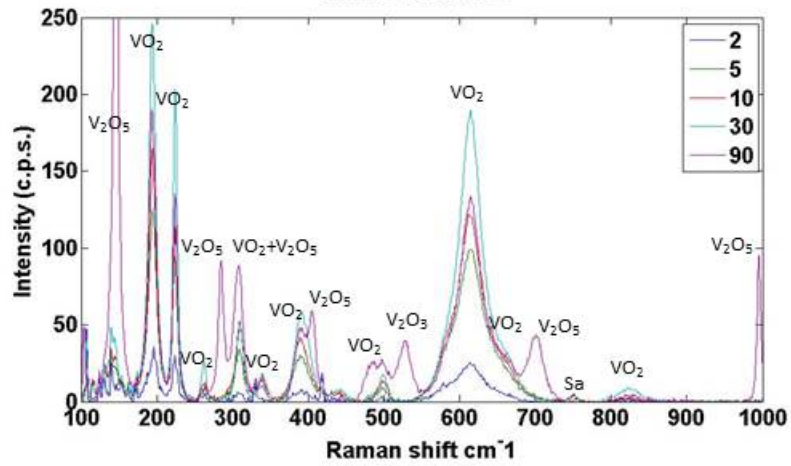
The following graphs show how the Raman spectra for each deposition process and substrate evolve during annealing. Peaks which can be attributed to the substrate or known oxides of vanadium are labeled, unknown peaks have the position listed. We note that a Raman signal for VO_2 is not observed for films on glass however they clearly have a phase transition. We believe that this is an optical phenomenon and have seen it before but do not know the specific origin.

S13

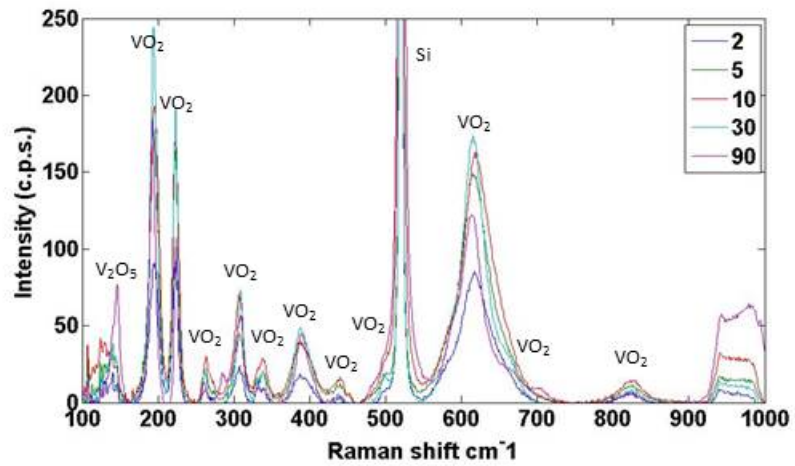
P_G



P_Sa



P_Si



16

Appendix B

Contributions to VO_2 Knowledge

Table B.1: Published work contributed towards vanadium dioxide understanding during time as a graduate student. Work covered in this dissertation is highlighted.

Publication Summary	Significance	Author List and Citation
Demonstration of photothermally induced optical switching in a Si-VO ₂ ring resonator.	10 dB of modulation and 1.26 nm change in resonant wavelength is observed.	J.D. Ryckman, V. Diez-Blanco, J. Nag, R.E. Marvel , B.K. Choi, R.F. Haglund, and S.M. Weiss.[13] (2012)
A Si-VO ₂ photonic device is switched with nanosecond laser pulses.	Device produces a 3 nm shift in resonance wavelength and 7 dB modulation at GHz speeds.	J.D. Ryckman, K.A. Hallman, R.E. Marvel , R.F. Haglund, and S.M. Weiss.[73] (2013)
Electro-optical modulation in a Si-VO ₂ device is demonstrated.	A maximum of 5 dB of modulation is observed; optical pulse durations as short as 2 ns result from the applied electric field.	P. Markov, R.E. Marvel , H.J. Conley, K.J. Miller, K. Bolotin, R.F. Haglund, Jr., and S.M. Weiss, ACS Photonics (2015)
The VO ₂ phase-transition is triggered by photo-injection of hot electrons.	This technique may be able to drive ultrafast phase transitions in transparent materials .	M. Hada, D. Zhang, A. Casandrac, R.J.D. Miller, Y. Hontani, J. Matsuo, R.E. Marvel , and R.F. Haglund, Jr.[163] (2012)
Femtosecond time-resolved photoelectron spectroscopy reveals that monoclinic VO ₂ transforms quasi-instantaneously into a metal.	The 80 fs "structural bottleneck" is not observed.	D. Wegkamp, M. Herzog, L. Xian, M. Gatti, P. Cudazzo, C.L. McGahan, R.E. Marvel , R.F. Haglund, A. Rubio, M. Wolf, and J. Stahler.[28] (2014)
The ultrafast insulator-to-metal transition in VO ₂ is driven by terahertz radiation.	The results are consistent with THz field-induced tunneling.	B. Mayer, C. Schmidt, A. Grupp, J. Bhler, J. Oelmann, R.E. Marvel , R.F. Haglund Jr., T. Oka, D. Brida, A. Leitenstorfer, and A. Pashkin, (PRB) (2015)
Ion implantation is used to dope VO ₂ thin films with Er ³⁺ ions.	Annealing at 800 C activates the Er while preserving the VO ₂ phase transition.	H. Lim, N. Stavrias, B.C. Johnson, R.E. Marvel , R.F. Haglund and J.C. McCallum.[91] (2014)
implantation is used to dope VO ₂ single crystals with Er ³⁺ ions.	Annealing at 825 C activates the Er while preserving the VO ₂ single crystal phase transition.	H. Lim, B.C. Johnson, R.E. Marvel , R.F. Haglund and J.C. McCallum, COMMAD (IEEE) Paper (2015)
A VO ₂ film is used to modulate the resonant wavelength of nanoantenna arrays.	Wavelength modulation of up to 110 nm is observed.	S.K. Earl, T.D. James, T.J. Davis, J.C. McCallum, R.E. Marvel , R.F. Haglund, Jr., and A. Roberts.[164] (2013)
A novel sub-diffraction limit imaging technique is demonstrated.	Resolution of 105 nm (using 392 nm) is achieved, offering a new method for nanoscale imaging.	O. Tzang, A. Pevzner, R.E. Marvel , R.F. Haglund , O. Cheshnovsky, Nano Letters (2015)
A new process for fabricating VO ₂ thin films using e-beam evaporation is presented.	A powder precursor is used, allowing for easy doping via powder mixing.	R.E. Marvel K. Appavoo B.K. Choi J. Nag and R.F. Haglund Jr.[165] (2012)
The role that substrate and deposition process play in the phase transition properties of VO ₂ thin films is explored.	Morphology varies significantly between deposition processes.	R.E. Marvel , R.R. Harl, V. Craciun, B.R. Rogers, R.F. Haglund Jr., Acta Materialia [98] (2015)
The plasmonic behavior of gold rods on a VO ₂ film is characterized with NSOM.	The rods switch from dipole to monopole nanoantennas during the phase transition.	Y. Abate, R.E. Marvel , J.I. Ziegler, S. Gamage, M.H. Javani, M.I. Stockman, R.F. Haglund Jr., Scientific Reports (2015)

Table B.2: Work contributed towards vanadium dioxide understanding during time as a graduate student. Work covered in this dissertation is highlighted.

Future Publication Summary	Significance	For Publication In
VO ₂ is pumped at different wavelengths and probed by a white-light continuum.	Differences in the coherent phonon behavior are observed.	JAP (2016)
Ellipsometry is used to measure the dielectric constants, n and k , from 350 nm to 40 μm , in W-doped and pure VO ₂ .	This data will be presented for the first time and in the context of other infrared spectroscopy work.	JAP or PRB (2016)

BIBLIOGRAPHY

- [1] F. J. Morin. Oxides which show a metal-to-insulator transition at the Néel temperature. *Physical Review Letters*, 3:34–36, Jul 1959.
- [2] Tao Yao, Xiaodong Zhang, Zhihu Sun, Shoujie Liu, Yuanyuan Huang, Yi Xie, Changzheng Wu, Xun Yuan, Wenqing Zhang, Ziyu Wu, Guoqiang Pan, Fengchun Hu, Lihui Wu, Qinghua Liu, and Shiqiang Wei. Understanding the nature of the kinetic process in a VO₂ metal-insulator transition. *Physical Review Letters*, 105:226405, Nov 2010.
- [3] Sven Westman. Note on a phase transition in VO₂. *Acta Chemica Scandinavica*, 15:217, December 1961.
- [4] Georg Anderson. Studies on vanadium oxides. *Acta Chemica Scandinavica*, 10:623–628, 1956.
- [5] J. H. Park, J.M. Coy, T.S. Kasirga, C. Huang, Z. Fei, S. Hunter, and D.H. Cobden. Measurement of a solid-state triple point at the metal-insulator transition in VO₂. *Nature*, 500(7463):431–434, 2013.
- [6] JP Pouget and H Launois. Metal-insulator phase transition in VO₂. *Le Journal de Physique Colloques*, 37(C4):C4–49, 1976.
- [7] Kevin Wang, Chun Cheng, Edy Cardona, Jingyang Guan, Kai Liu, and Junqiao Wu. Performance limits of microactuation with vanadium dioxide as a solid engine. *ACS Nano*, 7(3):2266–2272, 2013.
- [8] Kai Liu, Chun Cheng, Zhenting Cheng, Kevin Wang, Ramamoorthy Ramesh, and Junqiao Wu. Giant-amplitude, high-work density microactuators with phase transi-

tion activated nanolayer bimorphs. *Nano Letters*, 12(12):6302–6308, 2012. PMID: 23157372.

- [9] Rafmag Cabrera, Emmanuelle Merced, and Nelson Sepúlveda. A micro-electromechanical memory based on the structural phase transition of VO₂. *Physica Status Solidi (a)*, 210(9):1704–1711, 2013.
- [10] Aurelian Crunteanu, Julien Givernaud, Jonathan Leroy, David Mardivirin, Corinne Champeaux, Jean-Christophe Orlianges, Alain Catherinot, and Pierre Blondy. Voltage and current activated metal-insulator transition in VO₂ based electrical switches: a lifetime operation analysis. *Science and Technology of Advanced Materials*, 11(6):065002, 2010.
- [11] J.B. Kana Kana, J.M. Ndjaka, G. Vignaud, A. Gibaud, and M. Maaza. Thermally tunable optical constants of vanadium dioxide thin films measured by spectroscopic ellipsometry. *Optics Communications*, 284(3):807 – 812, 2011.
- [12] Ryan M. Briggs, Imogen M. Pryce, and Harry A. Atwater. Compact silicon photonic waveguide modulator based on the vanadium dioxide metal-insulator phase transition. *Optics Express*, 18(11):11192–11201, May 2010.
- [13] Judson D. Ryckman, V. Diez-Blanco, Joyeeta Nag, Robert E. Marvel, B. K. Choi, Richard F. Haglund, and Sharon M. Weiss. Photothermal optical modulation of ultra-compact hybrid Si-VO₂ ring resonators. *Optics Express*, 20(12):13215–13225, Jun 2012.
- [14] Petr Markov, Robert E. Marvel, Hiram J. Conley, Kevin J. Miller, Jr. Richard F. Haglund, and Sharon M. Weiss. Optically monitored electrical switching in vo₂. *ACS Photonics*, 2(8):1175–1182, 2015.
- [15] C.G. Granqvist, Bayrak Pehlivan, Y.-X. Ji, S.-Y. Li, and G.A. Niklasson. Elec-

trochromics and thermochromics for energy efficient fenestration: Functionalities based on nanoparticles of $\text{In}_2\text{O}_3:\text{Sn}$ and VO_2 . *Thin Solid Films*, pages 1–7, 2013.

- [16] Troy D. Manning, Ivan P. Parkin, Martyn E. Pemble, David Sheel, and Dimitra Vernardou. Intelligent window coatings: atmospheric pressure chemical vapor deposition of tungsten-doped vanadium dioxide. *Chemistry of Materials*, 16(4):744–749, 2004.
- [17] T. Driscoll, Hyun-Tak Kim, Byung-Gyu Chae, Bong-Jun Kim, Yong-Wook Lee, N. Marie Jokerst, S. Palit, D. R. Smith, M. Di Ventra, and D. N. Basov. Memory metamaterials. *Science*, 325(5947):1518–1521, 2009.
- [18] Mikhail A. Kats, Romain Blanchard, Patrice Genevet, Zheng Yang, M. Mumtaz Qazilbash, D. N. Basov, Shriram Ramanathan, and Federico Capasso. Thermal tuning of mid-infrared plasmonic antenna arrays using a phase change material. *Optics Letters*, 38(3):368–370, Feb 2013.
- [19] Y.S. Kivshar N.I. Zheludev. From metamaterials to metadevices. *Nature Materials*, 11(11):917–924, 2012.
- [20] Haidan Wen, Lu Guo, Eftihia Barnes, June Hyuk Lee, Donald A. Walko, Richard D. Schaller, Jarrett A. Moyer, Rajiv Misra, Yuelin Li, Eric M. Dufresne, Darrell G. Schlom, Venkatraman Gopalan, and John W. Freeland. Structural and electronic recovery pathways of a photoexcited ultrathin VO_2 film. *Physical Review B*, 88:165424, Oct 2013.
- [21] Dong-Wook Oh, Changhyun Ko, Shriram Ramanathan, and David G Cahill. Thermal conductivity and dynamic heat capacity across the metal-insulator transition in thin film VO_2 . *Applied Physics Letters*, 96(15):151906, 2010.
- [22] C. N. Berglund and H. J. Guggenheim. Electronic properties of VO_2 near the semiconductor-metal transition. *Physical Review*, 185:1022–1033, Sep 1969.

- [23] D. Kucharczyk and T. Niklewski. Accurate x-ray determination of the lattice parameters and the thermal expansion coefficients of VO₂ near the transition temperature. *Journal of Applied Crystallography*, 12(4):370–373, 1979.
- [24] C. N. Berglund and H. J. Guggenheim. Electronic properties of VO₂ near the semiconductor-metal transition. *Physical Review*, 185:1022–1033, Sep 1969.
- [25] Hua Guo, Kai Chen, Y. Oh, Kevin Wang, Catherine Dejoie, S. A. Syed Asif, O. L. Warren, Z. W. Shan, J. Wu, and A. M. Minor. Mechanics and dynamics of the strain-induced M1M2 structural phase transition in individual VO₂ nanowires. *Nano Letters*, 11(8):3207–3213, 2011. PMID: 21736336.
- [26] Changhyun Ko, Zheng Yang, and Shriram Ramanathan. Work function of vanadium dioxide thin films across the metal-insulator transition and the role of surface non-stoichiometry. *ACS Applied Materials & Interfaces*, 3(9):3396–3401, 2011. PMID: 21827179.
- [27] J. Cao, Y. Gu, W. Fan, L. Q. Chen, D. F. Ogletree, K. Chen, N. Tamura, M. Kunz, C. Barrett, J. Seidel, and J. Wu. Extended mapping and exploration of the vanadium dioxide stress-temperature phase diagram. *Nano Letters*, 10(7):2667–2673, 2010. PMID: 20586406.
- [28] Daniel Wegkamp, Marc Herzog, Lede Xian, Matteo Gatti, Pierluigi Cudazzo, Christina L. McGahan, Robert E. Marvel, Richard F. Haglund, Angel Rubio, Martin Wolf, and Julia Stähler. Instantaneous band gap collapse in photoexcited monoclinic VO₂ due to photocarrier doping. *Physical Review Letters*, 113:216401, Nov 2014.
- [29] Vance R. Morrison, Robert. P. Chatelain, Kunal L. Tiwari, Ali Hendaoui, Andrew Bruhcs, Mohamed Chaker, and Bradley J. Siwick. A photoinduced metal-like phase of monoclinic VO₂ revealed by ultrafast electron diffraction. *Science*, 346(6208):445–448, 2014.

- [30] J. Laverock, S. Kittiwatanakul, A. A. Zakharov, Y. R. Niu, B. Chen, S. A. Wolf, J. W. Lu, and K. E. Smith. Direct observation of decoupled structural and electronic transitions and an ambient pressure monoclinic-like metallic phase of VO₂. *Physical Review Letters*, 113:216402, Nov 2014.
- [31] Volker Eyert. The metal-insulator transitions of VO₂: A band theoretical approach. *Annals Phys (Leipzig)*, 11:1, July 2002.
- [32] John B. Goodenough. The two components of the crystallographic transition in VO₂. *Journal of Solid State Chemistry*, 3(4):490 – 500, 1971.
- [33] Nagaphani B. Aetukuri, Alexander X. Gray, Marc Drouard, Matteo Cossale, Li Gao, Alexander H. Reid, Roopali Kukreja, Hendrik Ohldag, Catherine A. Jenkins, Elke Arenholz, Kevin P. Roche, Hermann A. Durr, Mahesh G. Samant, and Stuart S. P. Parkin. Control of the metal-insulator transition in vanadium dioxide by modifying orbital occupancy. *Nature Physics*, 9(10):661–666, 2013.
- [34] Hyun-Tak Kim, Byung-Gyu Chae, Doo-Hyeb Youn, Gyungock Kim, Kwang-Yong Kang, Seung-Joon Lee, Kwan Kim, and Yong-Sik Lim. Raman study of electric-field-induced first-order metal-insulator transition in VO₂ based devices. *Applied Physics Letters*, 86(24), 2005.
- [35] Dmitry Ruzmetov, Kevin T. Zawilski, Venkatesh Narayanamurti, and Shriram Ramanathan. Structure-functional property relationships in rf-sputtered vanadium dioxide thin films. *Journal of Applied Physics*, 102(11), 2007.
- [36] Brett A. Kruger, Arash Joushaghani, and Joyce K. S. Poon. Design of electrically driven hybrid vanadium dioxide (VO₂) plasmonic switches. *Optics Express*, 20(21):23598–23609, Oct 2012.
- [37] Michel van Veenendaal. Ultrafast photoinduced insulator-to-metal transitions in vanadium dioxide. *Physical Review B*, 87:235118, Jun 2013.

- [38] S. Wall, D. Wegkamp, L. Foglia, K. Appavoo, J. Nag, R.F. Haglund Jr, J. Stahler, and M. Wolf. Ultrafast changes in lattice symmetry probed by coherent phonons. *Nature Communications*, (3):1–6, 2012.
- [39] A. Pashkin, C. Kübler, H. Ehrke, R. Lopez, A. Halabica, R. F. Haglund, R. Huber, and A. Leitenstorfer. Ultrafast insulator-metal phase transition in VO₂ studied by multiterahertz spectroscopy. *Physical Review B*, 83:195120, May 2011.
- [40] T. L. Cocker, L. V. Titova, S. Fourmaux, G. Holloway, H.-C. Bandulet, D. Brassard, J.-C. Kieffer, M. A. El Khakani, and F. A. Hegmann. Phase diagram of the ultrafast photoinduced insulator-metal transition in vanadium dioxide. *Physical Review B*, 85:155120, Apr 2012.
- [41] Kannatassen Appavoo, Dang Yuan Lei, Yannick Sonnefraud, Bin Wang, Sokrates T. Pantelides, Stefan A. Maier, and Richard F. Haglund. Role of defects in the phase transition of VO₂ nanoparticles probed by plasmon resonance spectroscopy. *Nano Letters*, 12(2):780–786, 2012.
- [42] J. Y. Suh, R. Lopez, L. C. Feldman, and R. F. Haglund. Semiconductor to metal phase transition in the nucleation and growth of VO₂ nanoparticles and thin films. *Journal of Applied Physics*, 96(2):1209–1213, 2004.
- [43] Tsung-Han Yang, Chunming Jin, Honghui Zhou, Roger J. Narayan, and J. Narayan. Role of twin boundaries in semiconductor to metal transition characteristics of VO₂ films. *Applied Physics Letters*, 97(7), 2010.
- [44] J. B. MacChesney, J. F. Potter, and H. J. Guggenheim. Preparation and properties of vanadium dioxide films. *Journal of The Electrochemical Society*, 115(1):52–55, 1968.
- [45] J. W. Tashman, J. H. Lee, H. Paik, J. A. Moyer, R. Misra, J. A. Mundy, T. Spila, T. A.

- Merz, J. Schubert, D. A. Muller, P. Schiffer, and D. G. Schlom. Epitaxial growth of VO₂ by periodic annealing. *Applied Physics Letters*, 104(6), 2014.
- [46] W.R. Roach and I. Balberg. Optical induction and detection of fast phase transition in VO₂. *Solid State Communications*, 9(9):551 – 555, 1971.
- [47] C. Kübler, H. Ehrke, R. Huber, R. Lopez, A. Halabica, R. F. Haglund, and A. Leitenstorfer. Coherent structural dynamics and electronic correlations during an ultrafast insulator-to-metal phase transition in VO₂. *Physical Review Letters*, 99:116401, Sep 2007.
- [48] A. Cavalleri, Cs. Tóth, C. W. Siders, J. A. Squier, F. Ráksi, P. Forget, and J. C. Kieffer. Femtosecond structural dynamics in VO₂ during an ultrafast solid-solid phase transition. *Physical Review Letters*, 87:237401, Nov 2001.
- [49] Peter Baum, Ding-Shyue Yang, and Ahmed H. Zewail. 4d visualization of transitional structures in phase transformations by electron diffraction. *Science*, 318(5851):788–792, 2007.
- [50] Joyeeta Nag, Richard F. Haglund, E. Andrew Payzant, and Karren L. More. Non-congruence of thermally driven structural and electronic transitions in VO₂. *Journal of Applied Physics*, 112(10), 2012.
- [51] Zhensheng Tao, Tzong-Ru T. Han, Subhendra D. Mahanti, Phillip M. Duxbury, Fei Yuan, Chong-Yu Ruan, Kevin Wang, and Junqiao Wu. Decoupling of structural and electronic phase transitions in vo₂. *Physical Review Letters*, 109:166406, Oct 2012.
- [52] Mikhail Hauryla, Guoqing Chen, Hui Chen, Jidong Zhang, Nicholas Nelson, David H Albonesi, Eby G Friedman, Philippe M Fauchet, et al. On-chip optical interconnect roadmap: challenges and critical directions. *IEEE Journal of Selected Topics in Quantum Electronics*, 12(6):1699–1705, 2006.

- [53] David AB Miller. Device requirements for optical interconnects to silicon chips. *Proceedings of the IEEE*, 97(7):1166–1185, 2009.
- [54] ITRS Committee et al. International technology roadmap for semiconductors executive summary. *New York: ITRS*, pages 13–17, 2007.
- [55] Andrew Alduino and Mario Paniccia. Interconnects: Wiring electronics with light. *Nature Photonics*, 1(3):153–155, 2007.
- [56] Jonas Weiss. Integrated photonics for datacenter and server interconnects. In *Transparent Optical Networks (ICTON), 2015 17th International Conference on*, pages 1–1. IEEE, 2015.
- [57] Jared F Bauters, Michael L Davenport, Martijn JR Heck, JK Doylend, Arnold Chen, Alexander W Fang, and John E Bowers. Silicon on ultra-low-loss waveguide photonic integration platform. *Optics Express*, 21(1):544–555, 2013.
- [58] Graham T Reed, G Mashanovich, FY Gardes, and DJ Thomson. Silicon optical modulators. *Nature Photonics*, 4(8):518–526, 2010.
- [59] Po Dong, Wei Qian, Hong Liang, Roshanak Shafiiha, Dazeng Feng, Guoliang Li, John E. Cunningham, Ashok V. Krishnamoorthy, and Mehdi Asghari. Thermally tunable silicon racetrack resonators with ultralow tuning power. *Optics Express*, 18(19):20298–20304, Sep 2010.
- [60] Richard A Soref and Brian R Bennett. Electrooptical effects in silicon. *IEEE Journal of Quantum Electronics*, 23(1):123–129, 1987.
- [61] Graham T Reed and Andrew P Knights. *Silicon photonics: an introduction*. John Wiley & Sons, 2004.
- [62] Lutz Waldecker, Timothy A Miller, Miquel Rudé, Roman Bertoni, Johann Osmond, Valerio Pruneri, Robert E Simpson, Ralph Ernstorfer, and Simon Wall. Time-domain

separation of optical properties from structural transitions in resonantly bonded materials. *Nature Materials*, 14(10):991–995, 2015.

- [63] Archana Singh, Vipul Srivastava, Mahendra Aynyas, and Sankar P. Sanyal. High pressure structural phase transition and elastic properties of yttrium pnictides. *Physica B: Condensed Matter*, 404(1213):1852 – 1857, 2009.
- [64] Seokbae Lee, Ki-Young Choi, Eilho Jung, Seulki Rho, Soohyeon Shin, Tuson Park, and Jungseek Hwang. Hidden non-fermi liquid behavior caused by magnetic phase transition in Ni-doped Ba-122 pnictides. *Scientific Reports*, 5, 2015.
- [65] F. Macià, G. Abril, A. Hernández-Mínguez, J. M. Hernandez, J. Tejada, and F. Parisi. Magnetic fingerprints of the very fast jumps of colossal magnetoresistance in the phase-separated manganite $\text{La}_{0.225}\text{Pr}_{0.40}\text{Ca}_{0.375}\text{MnO}_3$. *Physical Review B*, 77:012403, Jan 2008.
- [66] Hubert Jerominek, Francis Picard, Nicholas R. Swart, Martin Renaud, Marc Levesque, Mario Lehoux, Jean-Sebastien Castonguay, Martin Pelletier, Ghislain Bilodeau, Danick Audet, Timothy D. Pope, and Philippe Lambert. Micromachined uncooled VO_2 -based IR bolometer arrays. *Proceedings SPIE*, 2746(1996):60–71, 2013.
- [67] Hongchen Wang, Xinjian Yi, Guang Huang, Jing Xiao, Xiongwei Li, and Sihai Chen. IR microbolometer with self-supporting structure operating at room temperature. *Infrared Physics and Technology*, 45(1):53 – 57, 2004.
- [68] Changhong Chen, Xinjian Yi, Jing Zhang, and Bifeng Xiong. Micromachined uncooled IR bolometer linear array using VO_2 thin films. *International Journal of Infrared and Millimeter Waves*, 22(1):53–58, 2001.
- [69] Richard Haglund, E. U. Donev, L. C. Feldman, R. Lopez, and J. Y. Suh. Nanoscale

nonlinear optics coupling plasmonics to the metal-insulator transition in vanadium dioxide, 2007.

- [70] Zheng Yang, Changyun Ko, and Shriram Ramanathan. Oxide electronics utilizing ultrafast metal-insulator transitions. *Annual Review of Materials Research*, 41(1):337–367, 2011.
- [71] M Nakano, K Shibuya, D Okuyama, T Hatano, S Ono, M Kawasaki, Y Iwasa, and Y Tokura. Collective bulk carrier delocalization driven by electrostatic surface charge accumulation. *Nature*, 487:459–462, jul 2012.
- [72] Jaewoo Jeong, Nagaphani Aetukuri, Tanja Graf, Thomas D. Schladt, Mahesh G. Samant, and Stuart S. P. Parkin. Suppression of metal-insulator transition in VO₂ by electric field-induced oxygen vacancy formation. *Science*, 339(6126):1402–1405, 2013.
- [73] Judson D. Ryckman, Kent A. Hallman, Robert E. Marvel, Richard F. Haglund, and Sharon M. Weiss. Ultra-compact silicon photonic devices reconfigured by an optically induced semiconductor-to-metal transition. *Optics Express*, 21(9):10753–10763, May 2013.
- [74] G Stefanovich, A Pergament, and D Stefanovich. Electrical switching and Mott transition in VO₂. *Journal of Physics: Condensed Matter*, 12(41):8837, 2000.
- [75] Dmitry Ruzmetov, Gokul Gopalakrishnan, Changyun Ko, Venkatesh Narayana-murti, and Shriram Ramanathan. Three-terminal field-effect devices utilizing thin film vanadium oxide as the channel layer. *Journal of Applied Physics*, 107(11), 2010.
- [76] Yu-Hsuan Kuo, Yangs Ge, Shen Ren, Jonathan E. Roth, Theodore I. Kamins, David A. Miller, and James S. Harris. Strong quantum-confined Stark effect in

germanium quantum-well structures on silicon. *Nature*, 437:1334–1336, October 2005.

- [77] Michael Hochberg, Tom Baehr-Jones, Guangxi Wang, Michael Shearn, Katherine Harvard, Jingdong Luo, Baoquan Chen, Zhengwei Shi, Rhys Lawson, Phil Sullivan, Alex K. Y. Jen, Larry Dalton, and Axel Scherer. Terahertz all-optical modulation in a silicon-polymer hybrid system. *Nature Materials*, 1(5):703–709, August 2006.
- [78] Magdalena S. Nawrocka, Tao Liu, Xuan Wang, and Roberto R. Panepucci. Tunable silicon microring resonator with wide free spectral range. *Applied Physics Letters*, 89(7), 2006.
- [79] T. Ben-Messaoud, G. Landry, J.P. Garipy, B. Ramamoorthy, P.V. Ashrit, and A. Hach. High contrast optical switching in vanadium dioxide thin films. *Optics Communications*, 281(24):6024 – 6027, 2008.
- [80] Jacob T. Robinson, Long Chen, and Michal Lipson. On-chip gas detection in silicon optical microcavities. *Optics Express*, 16(6):4296–4301, Mar 2008.
- [81] Qianfan Xu, David Fattal, and Raymond G. Beausoleil. Silicon microring resonators with 1.5- μm radius. *Optics Express*, 16(6):4309–4315, Mar 2008.
- [82] Ming Liu, Xiaobo Yin, Erick Ulin-Avila, Baisong Geng, Thomas Zentgraf, Long Ju, Feng Wang, and Xiang Zhang. A graphene-based broadband optical modulator. *Nature*, 1(474):64–67, March 2011.
- [83] T. Liang, L. Nunes, T. Sakamoto, K. Sasagawa, T. Kawanishi, M. Tsuchiya, G. Priem, D. Van Thourhout, P. Dumon, R. Baets, and H. Tsang. Ultrafast all-optical switching by cross-absorption modulation in silicon wire waveguides. *Optics Express*, 13(19):7298–7303, Sep 2005.

- [84] M. M. Qazilbash, M. Brehm, G. O. Andreev, A. Frenzel, P.-C. Ho, Byung-Gyu Chae, Bong-Jun Kim, Sun Jin Yun, Hyun-Tak Kim, A. V. Balatsky, O. G. Shpyrko, M. B. Maple, F. Keilmann, and D. N. Basov. Infrared spectroscopy and nano-imaging of the insulator-to-metal transition in vanadium dioxide. *Physical Review B*, 79:075107, Feb 2009.
- [85] Ling Liao, Dean Samara-Rubio, Michael Morse, Ansheng Liu, Dexter Hodge, Doron Rubin, Ulrich D. Keil, and Thorkild Franck. High speed silicon Mach-Zehnder modulator. *Optics Express*, 13(8):3129–3135, Apr 2005.
- [86] William M. J. Green, Michael J. Rooks, Lidija Sekaric, and Yurii A. Vlasov. Ultra-compact, low rf power, 10 gb/s silicon mach-zehnder modulator. *Optics Express*, 15(25):17106–17113, Dec 2007.
- [87] M.R. Watts, D.C. Trotter, R.W. Young, and A.L. Lentine. Ultralow power silicon microdisk modulators and switches. In *Group IV Photonics, 2008 5th IEEE International Conference on*, pages 4–6, Sept 2008.
- [88] Long Chen, Kyle Preston, Sasikanth Manipatruni, and Michal Lipson. Integrated GHz silicon photonic interconnect with micrometer-scale modulators and detectors. *Optics Express*, 17(17):15248–15256, Aug 2009.
- [89] E. Desurvire, J. R. Simpson, and P. C. Becker. High-gain erbium-doped traveling-wave fiber amplifier. *Optics Letters*, 12(11):888–890, Nov 1987.
- [90] Sébastien Cueff, Dongfang Li, You Zhou, Franklin J Wong, Jonathan A Kurvits, Shriram Ramanathan, and Rashid Zia. Dynamic control of light emission faster than the lifetime limit using VO₂ phase-change. *Nature Communications*, 6, 2015.
- [91] Herianto Lim, Nikolas Stavrias, Brett C. Johnson, Robert E. Marvel, Richard F. Haglund, and Jeffrey C. McCallum. Optical switching and photoluminescence in

- erbium-implanted vanadium dioxide thin films. *Journal of Applied Physics*, 115(9), 2014.
- [92] Herianto Lim, Brett C Johnson, Robert E Marvel, Richard F Haglund, and Jeffrey C McCallum. Optical spectroscopy of erbium doped monocrystalline vanadium dioxide. In *Optoelectronic and Microelectronic Materials & Devices (COMMAD), 2014 Conference on*, pages 230–232. IEEE, 2014.
- [93] A.J Kenyon. Recent developments in rare-earth doped materials for optoelectronics. *Progress in Quantum Electronics*, 26(45):225 – 284, 2002.
- [94] James F. Ziegler, M.D. Ziegler, and J.P. Biersack. SRIM: The stopping and range of ions in matter (2010). *Nuclear Instruments and Methods in Physics Research Section B: Beam Interactions with Materials and Atoms*, 268(1112):1818 – 1823, 2010. 19th International Conference on Ion Beam Analysis.
- [95] Peter Schilbe. Raman scattering in VO₂. *Physica B: Condensed Matter*, 316317(0):600 – 602, 2002. Proceedings of the 10th International Conference on Phonon Scattering in Condensed Matter.
- [96] James F Gibbons. Ion implantation in semiconductors-part II: Damage production and annealing. *Proceedings of the IEEE*, 60(9):1062–1096, 1972.
- [97] J.-G. Ramírez, Rainer Schmidt, A. Sharoni, M. E. Gómez, Ivan K. Schuller, and Edgar J. Patio. Ultra-thin filaments revealed by the dielectric response across the metal-insulator transition in VO₂. *Applied Physics Letters*, 102(6), 2013.
- [98] Robert E Marvel, Robert R Harl, Valentin Craciun, Bridget R Rogers, and Richard F Haglund. Influence of deposition process and substrate on the phase transition of vanadium dioxide thin films. *Acta Materialia*, 91:217–226, 2015.

- [99] M. K. Liu, M. Wagner, E. Abreu, S. Kittiwatanakul, A. McLeod, Z. Fei, M. Goldflam, S. Dai, M. M. Fogler, J. Lu, S. A. Wolf, R. D. Averitt, and D. N. Basov. Anisotropic electronic state via spontaneous phase separation in strained vanadium dioxide films. *Physical Review Letters*, 111:096602, Aug 2013.
- [100] Sergey Lysenko, Felix Fernandez, Armando Rua, and Huimin Liu. Ultrafast light scattering imaging of multi-scale transition dynamics in vanadium dioxide. *Journal of Applied Physics*, 114(15), 2013.
- [101] Yong Zhao, Joon Hwan Lee, Yanhan Zhu, M. Nazari, Changhong Chen, Haiyan Wang, Ayrton Bernussi, Mark Holtz, and Zhaoyang Fan. Structural, electrical, and terahertz transmission properties of VO₂ thin films grown on c-, r-, and m-plane sapphire substrates. *Journal of Applied Physics*, 111(5):–, 2012.
- [102] Gisia Beydaghyan, Vincent Basque, and P.V. Ashrit. High contrast thermochromic switching in vanadium dioxide (VO₂) thin films deposited on indium tin oxide substrates. *Thin Solid Films*, 522:204 – 207, 2012.
- [103] R. J. Jaccodine. Surface energy of germanium and silicon. *Journal of The Electrochemical Society*, 110(6):524–527, 1963.
- [104] S. K. Rhee. Critical surface energies of Al₂O₃ and graphite. *Journal of the American Ceramic Society*, 55(6):300–303, 1972.
- [105] Douglas A. Olsen and A. Jean Osteraas. The critical surface tension of glass. *The Journal of Physical Chemistry*, 68(9):2730–2732, 1964.
- [106] Sebastian Fahler and Hans-Ulrich Krebs. Calculations and experiments of material removal and kinetic energy during pulsed laser ablation of metals. *Applied Surface Science*, 9698(0):61 – 65, 1996. Proceedings of Symposium F: Third International Symposium on Laser Ablation of the 1995 E-MRS Spring Conference.

- [107] $k_B T$ at powder melting temperature.
- [108] John A. Thornton. *Deposition Technologies for Films and Coatings*. Noyes Publications, 1982.
- [109] John F. Moulder, Jill Chastain, and Roger C. King. *Handbook of X-ray Photoelectron Spectroscopy: a reference book of standard spectra for identification and interpretation of XPS data*. Physical Electronics, February 1995.
- [110] David Neas and Petr Klapetek. Gwyddion: an open-source software for SPM data analysis. *Central European Journal of Physics*, 10:181–188, 2012.
- [111] Geert Silversmit, Diederik Depla, Hilde Poelman, Guy Marin, and Roger De Gryse. Determination of the V_{2p} XPS binding energies for different vanadium oxidation states (V^{5+} to V^{0+}). *Journal of Electron Spectroscopy and Related Phenomena*, 135(2-3):167–175, 2004.
- [112] M. Demeter, M. Neumann, and W. Reichelt. Mixed-valence vanadium oxides studied by XPS. *Surface Science*, 454456(0):41 – 44, 2000.
- [113] Kai Zhang, Madhavi Tangirala, David Nminibapiel, Wei Cao, Venkateswara Pallem, Christian Dussarrat, and Helmut Baumgart. Synthesis of VO_2 thin films by atomic layer deposition with TEMAV as precursor. *ECS Transactions*, 50(13):175–182, 2013.
- [114] Amos Sharoni, Juan Gabriel Ramirez, and Ivan K. Schuller. Multiple avalanches across the metal-insulator transition of vanadium oxide nanoscaled junctions. *Physical Review Letters*, 101:026404, Jul 2008.
- [115] John Rozen, Ren Lopez, Richard F. Haglund, and Leonard C. Feldman. Two-dimensional current percolation in nanocrystalline vanadium dioxide films. *Applied Physics Letters*, 88(8), 2006.

- [116] H. E. Bennett and J. O. Porteus. Relation between surface roughness and specular reflectance at normal incidence. *Journal Optical Society America*, 51(2):123–129, Feb 1961.
- [117] R. Lopez, T. E. Haynes, L. A. Boatner, L. C. Feldman, and R. F. Haglund. Size effects in the structural phase transition of VO₂ nanoparticles. *Physical Review B*, 65:224113, Jun 2002.
- [118] Carl V. Thompson. Solid-state dewetting of thin films. *Annual Review Materials Research*, 42:399–434, May 2012.
- [119] Richard R. Thomas, Frank B. Kaufman, Juergen T. Kirleis, and Richard A. Bel-sky. Wettability of polished silicon oxide surfaces. *Journal of The Electrochemical Society*, 143(2):643–648, 1996.
- [120] Seon-Hwa Kim, Yong-Lak Choi, Yo-Seung Song, Deuk Yong Lee, and Se-Jong Lee. Influence of sputtering parameters on microstructure and morphology of TiO₂ thin films. *Materials Letters*, 57(2):343 – 348, 2002.
- [121] H Windischmann. Intrinsic Stress in Sputter-Deposited Thin-Films. *Critical Reviews in Solid State and Materials Sciences*, 17(6):547–596, 1992.
- [122] Carl V. Thompson. Structure evolution during processing of polycrystalline films. *Annual Review Materials Research*, 30:159–190, August 2000.
- [123] M. Guntersdorfer. Die leitfhigkeitsanomale in vanadiumdioxid. *Solid-State Elec-tronics*, 13(3):355 – 367, 1970.
- [124] H. Zhou, M. F. Chisholm, Tsung-Han Yang, S. J. Pennycook, and J. Narayan. Role of interfacial transition layers in VO₂/Al₂O₃ heterostructures. *Journal of Applied Physics*, 110(7), 2011.

- [125] Mengkun Liu, Harold Y Hwang, Hu Tao, Andrew C Strikwerda, Kebin Fan, George R Keiser, Aaron J Sternbach, Kevin G West, Salinporn Kittiwatanakul, Jiwei Lu, et al. Terahertz-field-induced insulator-to-metal transition in vanadium dioxide metamaterial. *Nature*, 487(7407):345–348, 2012.
- [126] Beth S. Guiton, Qian Gu, Amy L. Prieto, Mark S. Gudiksen, and Hongkun Park. Single-crystalline vanadium dioxide nanowires with rectangular cross sections. *Journal of the American Chemical Society*, 127(2):498–499, 2005.
- [127] In Soo Kim and Lincoln J. Lauhon. Increased yield and uniformity of vanadium dioxide nanobeam growth via two-step physical vapor transport process. *Crystal Growth & Design*, 12(3):1383–1387, 2012.
- [128] Brian T OCallahan, Andrew C Jones, Jae Hyung Park, David H Cobden, Joanna M Atkin, and Markus B Raschke. Inhomogeneity of the ultrafast insulator-to-metal transition dynamics of VO₂. *Nature Communications*, 6, 2015.
- [129] Chun Cheng, Kai Liu, Bin Xiang, Joonki Suh, and Junqiao Wu. Ultra-long, free-standing, single-crystalline vanadium dioxide micro/nanowires grown by simple thermal evaporation. *Applied Physics Letters*, 100(10), 2012.
- [130] Harish N. S. Krishnamoorthy, You Zhou, Shriram Ramanathan, Evgenii Narimanov, and Vinod M. Menon. Tunable hyperbolic metamaterials utilizing phase change heterostructures. *Applied Physics Letters*, 104(12), 2014.
- [131] Hao Wang, Yue Yang, and Liping Wang. Switchable wavelength-selective and diffuse metamaterial absorber/emitter with a phase transition spacer layer. *Applied Physics Letters*, 105(7), 2014.
- [132] Dacheng Wang, Lingchao Zhang, Yinghong Gu, MQ Mehmood, Yandong Gong, Amar Srivastava, Linke Jian, T Venkatesan, Cheng-Wei Qiu, and Minghui Hong.

- Switchable ultrathin quarter-wave plate in terahertz using active phase-change meta-surface. *Scientific Reports*, 5, 2015.
- [133] Kyle Zufelt. Highly efficient infrared photodetectors based on plasmonic metamaterials and vanadium dioxide. *Vanderbilt Masters Thesis*, 1, 2014.
- [134] A. A. Bugaev, V.V. Gudyalis, B. P. Zakharchenya, and F.A. Chudnovskii. Selectivity of the photoexcited metal-semiconductor phase transition in vanadium dioxide initiated by picosecond pulses. *JETP Letters*, 34(8):430–452, Aug 1981.
- [135] Michael F. Becker, A. Bruce Buckman, Rodger M. Walser, Thierry Lpine, Patrick Georges, and Alain Brun. Femtosecond laser excitation of the semiconductor-metal phase transition in VO_2 . *Applied Physics Letters*, 65(12), 1994.
- [136] Michael F. Becker, A. Bruce Buckman, Rodger M. Walser, Thierry Lpine, Patrick Georges, and Alain Brun. Femtosecond laser excitation dynamics of the semiconductor-metal phase transition in VO_2 . *Journal of Applied Physics*, 79(5), 1996.
- [137] Ferenc Krausz and Misha Ivanov. Attosecond physics. *Review Modern Physics*, 81:163–234, Feb 2009.
- [138] Ahmed H Zewail. Femtochemistry: Atomic-scale dynamics of the chemical bond. *The Journal of Physical Chemistry A*, 104(24):5660–5694, 2000.
- [139] Keith A Nelson and Ahmed H Zewail. *Ultrafast Spectroscopy of Chemical and Biological Processes*. Optical Society of America, 1990.
- [140] H. J. Zeiger, J. Vidal, T. K. Cheng, E. P. Ippen, G. Dresselhaus, and M. S. Dresselhaus. Theory for displacive excitation of coherent phonons. *Physical Review B*, 45:768–778, Jan 1992.

- [141] David G Cahill, Wayne K Ford, Kenneth E Goodson, Gerald D Mahan, Arun Majumdar, Humphrey J Maris, Roberto Merlin, and Simon R Phillpot. Nanoscale thermal transport. *Journal of Applied Physics*, 93(2):793–818, 2003.
- [142] Guray Tas and Humphrey J. Maris. Electron diffusion in metals studied by picosecond ultrasonics. *Physical Review B*, 49:15046–15054, Jun 1994.
- [143] A. Cavalleri, Th. Dekorsy, H. H. W. Chong, J. C. Kieffer, and R. W. Schoenlein. Evidence for a structurally-driven insulator-to-metal transition in VO₂: A view from the ultrafast timescale. *Physical Review B*, 70:161102, Oct 2004.
- [144] M. Rini, Z. Hao, R. W. Schoenlein, C. Giannetti, F. Parmigiani, S. Fourmaux, J. C. Kieffer, A. Fujimori, M. Onoda, S. Wall, and A. Cavalleri. Optical switching in VO₂ films by below-gap excitation. *Applied Physics Letters*, 92(18), 2008.
- [145] Marieke Jager, Christian Ott, Christopher Kaplan, Robert Marvel, Richard Haglund, Daniel Neumark, and Steve Leone. Attosecond transient absorption spectroscopy of an insulator-to-metal phase transition material: Vanadium dioxide. *ATTO2015*, 64:14:00–14:15, May 2015.
- [146] S. Wall, L. Foglia, D. Wegkamp, K. Appavoo, J. Nag, R. Haglund, J. Stähler, and M. Wolf. Tracking the evolution of electronic and structural properties of VO₂ during the ultrafast photoinduced insulator-metal transition. *Physical Review B*, 87:115126, Mar 2013.
- [147] Rikiya Yoshida, Takashi Yamamoto, Yukiaki Ishida, Hiroki Nagao, Tsubasa Otsuka, Kuninari Saeki, Yuji Muraoka, Ritsuko Eguchi, Kyoko Ishizaka, Takayuki Kiss, Shuntaro Watanabe, Teruto Kanai, Jiro Itatani, and Shik Shin. Ultrafast photoinduced transition of an insulating VO₂ thin film into a nonrutile metallic state. *Physical Review B*, 89:205114, May 2014.

- [148] Wen-Pin Hsieh, Mariano Trigo, David A. Reis, Gianluca Andrea Artioli, Lorenzo Malavasi, and Wendy L. Mao. Evidence for photo-induced monoclinic metallic VO₂ under high pressure. *Applied Physics Letters*, 104(2), 2014.
- [149] A. Oschlies, R. W. Godby, and R. J. Needs. First-principles self-energy calculations of carrier-induced band-gap narrowing in silicon. *Physical Review B*, 45:13741–13744, Jun 1992.
- [150] R.A. Abram, G.J. Rees, and B.L.H. Wilson. Heavily doped semiconductors and devices. *Advances in Physics*, 27(6):799–892, 1978.
- [151] Joachim Wagner. Band-gap narrowing in heavily doped silicon at 20 and 300 k studied by photoluminescence. *Physical Review B*, 32:1323–1325, Jul 1985.
- [152] Y. Dou, T. Fishlock, R. G. Egdell, D. S. L. Law, and G. Beamson. Band-gap shrinkage in n-type-doped CdO probed by photoemission spectroscopy. *Physical Review B*, 55:R13381–R13384, May 1997.
- [153] Catalin D. Spataru, Lorin X. Benedict, and Steven G. Louie. *Ab initio* calculation of band-gap renormalization in highly excited GaAs. *Physical Review B*, 69:205204, May 2004.
- [154] Elbio Dagotto. Complexity in strongly correlated electronic systems. *Science*, 309(5732):257–262, 2005.
- [155] François Gervais and Winfried Kress. Lattice dynamics of oxides with rutile structure and instabilities at the metal-semiconductor phase transitions of NbO₂ and VO₂. *Physical Review B*, 31:4809–4814, Apr 1985.
- [156] Xiaogang Tan, Tao Yao, Ran Long, Zhihu Sun, Yajuan Feng, Hao Cheng, Xun Yuan, Wenqing Zhang, Qinghua Liu, Changzheng Wu, Yi Xie, and Shiqiang Wei. Unrav-

- eling metal-insulator transition mechanism of VO₂ triggered by tungsten doping. *Scientific Reports*, 2(2):466 – 470, 2012.
- [157] Tai-Lung Wu, Luisa Whittaker, Sarbajit Banerjee, and G. Sambandamurthy. Temperature and voltage driven tunable metal-insulator transition in individual W_xV_{1-x}O₂ nanowires. *Physical Review B*, 83:073101, Feb 2011.
- [158] Hasti Asayesh-Ardakani, Anmin Nie, Peter M. Marley, Yihan Zhu, Patrick J. Phillips, Sujay Singh, Farzad Mashayek, Ganapathy Sambandamurthy, Ke bin Low, Robert F. Klie, Sarbajit Banerjee, Gregory M. Odegard, and Reza Shahbazian-Yassar. Atomic origins of monoclinic-tetragonal (rutile) phase transition in doped VO₂ nanowires. *Nano Letters*, 15(11):7179–7188, 2015. PMID: 26457771.
- [159] T. J. Huffman, Peng Xu, M. M. Qazilbash, E. J. Walter, H. Krakauer, Jiang Wei, D. H. Cobden, H. A. Bechtel, M. C. Martin, G. L. Carr, and D. N. Basov. Anisotropic infrared response of vanadium dioxide microcrystals. *Physical Review B*, 87:115121, Mar 2013.
- [160] A. S. Barker, H. W. Verleur, and H. J. Guggenheim. Infrared optical properties of vanadium dioxide above and below the transition temperature. *Physical Review Letters*, 17:1286–1289, Dec 1966.
- [161] Private communication.
- [162] M. M. Qazilbash, A. A. Schafgans, K. S. Burch, S. J. Yun, B. G. Chae, B. J. Kim, H. T. Kim, and D. N. Basov. Electrodynamics of the vanadium oxides VO₂ and V₂O₃. *Physical Review B*, 77:115121, Mar 2008.
- [163] Masaki Hada, Dongfang Zhang, Albert Casandruc, R. J. Dwayne Miller, Yusaku Hontani, Jiro Matsuo, Robert E. Marvel, and Richard F. Haglund. Hot electron injection driven phase transitions. *Physical Review B*, 86:134101, Oct 2012.

- [164] Stuart K. Earl, Timothy D. James, Timothy J. Davis, Jeffrey C. McCallum, Robert E. Marvel, Richard F. Haglund, and Ann Roberts. Tunable optical antennas enabled by the phase transition in vanadium dioxide. *Optics Express*, 21(22):27503–27508, Nov 2013.
- [165] R.E. Marvel, K. Appavoo, B.K. Choi, J. Nag, and Jr. Haglund, R.F. Electron-beam deposition of vanadium dioxide thin films. *Applied Physics A*, 111(3):975–981, 2013.